High Momentum Transfer Nucleon Elastic Electromagnetic Form Factor Measurements Using Super BigBite Spectrometer at Jefferson Lab

Danning Di

Qinhuangdao, Hebei, China

B.S., Nankai University (2012)

A Dissertation Presented to the Graduate Faculty

of the University of Virginia in Candidacy for the Degree of

Doctor of Philosophy

Department of Physics

University of Virginia

October, 2019

Abstract

The nucleons - protons and neutrons - are the basic building blocks of atomic nuclei. We now know that the nucleon consists of fundamental particles called quarks and gluons. The quarks interact with each other by exchanging gluons via the strong interaction. Understanding the quark-gluon structure of the nucleon, especially the confinement of quarks within the nucleon in its ground state, remains one of the main unsolved puzzles of particle physics. The nucleon electromagnetic form factors are directly related to the internal structure of the nucleon. A new generation of high precision experiments, GEp-V, GEn-II, GEn-RP, and GMn, measuring the ground state nucleon space-like electro-magnetic form factor at high momentum transfer is underway at Jefferson Lab experimental Hall-A as part of the Super Bigbite Spectrometer (SBS) program. This series of experiments will provide a new level of understanding of the nucleon structure. These experiments are highly demanding due to the extremely fast drop off of the elastic cross section with the increasing four-momentum transfer squared(Q^2). This thesis provides an overview of the SBS physics program and reports on the extensive R&D program carried out to achieve the high rate running conditions essential for carrying out the SBS experiments. SBS will provide an intermediate solid angle of approximately 35 msr, which is significantly larger than the solid angle of other dipole based spectrometers at Jefferson lab. Of course, there are much larger acceptance spectrometers at Jefferson Lab, CLAS12 for example. What is special about SBS is that it provides a sizable acceptance while operating at the highest possible luminosity at Jefferson Lab. With this combination of medium acceptance and the highest available luminosity, SBS provides an unparalleled opportunity to explore the nucleon in its ground state with unprecedented resolution.

The relatively large acceptance of SBS is achieved by using a large gap dipole magnet and placing it close to the target. An unavoidable consequence of this is that the SBS GEM trackers and other detectors have a clear line-of-sight view of the target and a portion of the beam-line. As a result, the background hit rate in the SBS front GEM trackers is expected to be up to 500 kHz/cm^2, over the entire active area of 6000 cm^2. To the best of our knowledge, this extremely high rate over such a large area is unprecedented in any particle

tracking system used anywhere in the world before. Correctly reconstructing the particle tracks of interest in this very high background environment is achieved by using especially adapted high rate techniques at every step of the tracking process: optimizing the GEM module and tracker design at the hardware level, using high bandwidth electronics and real time Field Programmable Gate Array (FPGA) based background suppression techniques at the Data Acquisition (DAQ) level, and developing highly specialized tracking algorithms to pick out the signal hits from among the vast amount of background hits. In order to ensure a smooth start and running of the SBS experiments, it is extremely crucial that these techniques are developed, implemented, and tested under realistic conditions well before the actual start of the SBS experimental program. A detailed Geant4 simulation of the experiment was combined with a digitization package to generate the detector level pseudo-data similar to what is expected in the actual experiments. The digitization procedures were calibrated against actual GEM data from cosmic-ray runs, X-ray tests, beam test runs in experimental Hall-A, and the PRad experiment in Hall B. Then, optimized tracking algorithms were developed and implemented in an analysis program used to analyze these pseudo-data and to extract expected high-level parameters. These extracted quantities were then compared with the input parameters from the simulation to verify and determine the performance characteristics for the SBS tracker. From this work, a final tracking efficiency of 69% at 25% occupancy was achieved, with the required reconstruction accuracy, for the GMn experiment, the first experiment in the SBS program, with background level at 100 kHz/cm^2. These demonstrated parameters are adequate for the successful running of not only the GMn experiment but as well as for GEn-RP and GEn-II experiments, the second and third experiments in the program. This work builds the solid ground to further improve the tracking performance for these experiments and achieve similar conditions for the running of the GEp-V experiment, the most demanding experiment in the SBS program, with an expected background level at 500 kHz/cm^2.

Acknowledgments

This thesis would not have been possible without the support and encouragement from many, many people. I would like to take this opportunity to thank everyone for helping me in this long and exciting journey.

First and foremost, I must thank my thesis advisor, Nilanga Liyanage, for his continuous guidance and support. I would never think of reaching this point if it were not for his patience, motivation and immense knowledge. In the beginning of my research, I was daunted by the challenge I was facing to achieve the high rate running condition for the SBS experiments. For many times I told myself this is impossible. It was him who gave me the confidence and countless precious advice in our weekly discussion. Moreover, he taught me his deep understanding of physics behind its mathematical expressions and how to become a physicist.

I would like to thank all my colleagues in the GEM Detector Lab at University of Virginia for the help and inspiration I received from them: Vladimir Nelyubin, Kondo Gnanvo, Huong Thi Nguyen, Chao Gu, Xinzhan Bai, John Matter, Siyu Jian, John Boyd, Sean Jeffas, Rong Wang, and Yan Huang. I thank Kondo for patiently teaching me about the GEM detector and the data acquisition system when I started out in my research. I wish to thank Xinzhan for all the productive discussions we had about data analysis. I sincerely thank Huong, Kondo, Xinzhan, Vladimir, Rong, and Yan for their unparalleled expertise in GEM construction. The exceptional GEM detectors from them set the solid foundation for me to achieve my research goal.

I would like to thank all my colleagues at Jefferson Lab: Bogdan Wojtsekhowski, Mark Jones, Alexandre Camsonne, Ole Hansen, Chuck Long, Andrew Puckett, Seamus Riordan, Eric Fuchey, Bryan Moffit, Benjamin Raydo, Evaristo Cisbani, Paolo Musico, and Jixie Zhang. I thank Bogdan for sharing his insights in physics. I would never forget those simple yet thought-provoking questions he asked in the first summer I spent at Jefferson Lab. I wish to thank Mark, Chuck, and Alex for their help I received during the 2016 GEM test in Hall A. I would like to thank Eric for his help in performing the Geant4 simulation of the experiment. I thank Bryan, Ben and

Paolo for their help in building the data acquisition system for the GEM detectors.

I would also like to thank all my friends, both at UVa and Jefferson Lab, for their friendship and the wonderful time we shared. They are: Xinzhan Bai, Huangxing Li, Wenjiang Fan, Haina Li, Haoyu Chen, Kai Jin, Wenyang Qian, Nguyen Ton, Jie Liu, Evan Graber, Peng Peng, Yuxiang Zhao, Yi Qiang, Chao Gu, Ye Li, Tong Su, Dien Nguyen, Shujie Li, Ye Tian, Jixie Zhang, and Ke Li. I am especially thankful to Ke, Wenjiang, Haina, and Xinzhan for caring and hosting me during my recovery from the ski accident I had in 2015. I would have no chance achieving this without them. I shall forever remember the love you gave in the weakest phase of my life.

Finally I would like to thank my parents for their unconditional love, understanding, and encouragement in this long adventure. I thank my mother for her diligence and determination. She set me a great example of what to do whenever I am in doubt. I thank my father for initiating my interest in physics. I still remember our discussion when I was eight about why a mosquito can catch up the speed of a car when it is inside the car. They have always been open and supportive to my decisions. For these, I am eternally thankful. I dedicate this thesis to you.

Contents

List of Figures

List of Tables

Chapter 1

Introduction

What is matter made of and how do the most fundamental parts interact with each other? The first answer to this question was perhaps given 26 centuries ago by Ancient Greek philosopher Anaximenes of Miletus (born 585 BC) who believed that all matter originates from air. Then, less than 100 years later, Democritus (460 BC - 370 BC), drawing on the teachings of two Greek philosophers who came before him, Leucippus and Anaxagoras, developed the first atomic theory of matter. Democritus' model stated that matter consists of invisible particles called atoms and a void (empty space) between them. He believed that atoms are indestructible and unchangeable. Also that they are homogeneous, meaning they have no internal structure. According to this model all atoms differ in size, shape, mass, position and arrangement.

Although not exactly correct, this way of thinking that various objects in our universe are made of common fundamental element(s) is beneficial to this day. In 1869, Russian chemist Dmitri Mendeleev answered the question with the first recognizable periodic table listing elements that are the fundamental building blocks of matter. In the late 19th century, the electron was discovered by Thomson. In the early 20th century, Rutherford formulated the modern model of the atom from his famous gold foil experiment. With the discovery of the neutron by Chadwick in 1932, a relatively modern picture of the atom came up; all matter is made of atoms that are composed of a charged core known as the nucleus which consists of two types of building blocks(protons and neutrons - collectively know as nucleons) and one or more

electrons orbiting, as rather accurately described by relativistic quantum mechanics, around the nucleus. For a very short time, the electron, proton and neutron were believed to be the most fundamental particles that make up all matter. However, in 1933, Stern, with his measurement of anomalously large magnetic moment of the proton, showed that the nucleons also have structure.

For a point-like spin 1/2 particle, the magnetic moment is:

$$\mu = \frac{ge'}{2e}\mu_N \tag{1.1}$$

where e' is the particles charge, e is the charge of an electron, $\mu_N = \frac{e\hbar}{2m}$ is the nuclear magneton and g is the g-factor which is close to 2 for spin 1/2 point-like particles like electrons. The measurement of the magnetic moment of the protons and neutrons showed that $\mu_p = 2.79\mu_N$ and $\mu_n = -1.91\mu_N$, instead of $\mu_p = \mu_N$ and $\mu_n = 0$ if they were point-like particles. This clear suggested that the nucleon was not point-like but must have a sub-structure. In 1956, Hofstadter further confirmed that the nucleons have structure with his elastic scattering experiment. The experiment showed that the elastic scattering cross section of an electron from a proton differs from theoretical prediction of the cross section for a point particle. Ever since then, the structure of the nucleon has been actively studied by particle physicists. There has been much advancement in our understanding of the nucleon structure. However, to this day, no complete and accurate answer is yet available. Many modern experiments strives to gain more information on the nucleons to test and give insight to new theories. This thesis discusses the work to enable one of these projects at Jefferson Lab studying the nucleon structure it its ground state with unprecedented precision.

1.1 Nucleon structure

Today perhaps the most well accepted answer to the question *What is matter made of ?* comes from the standard model of particle physics. In the standard model there are three types of particles that make up the world around us: leptons, quarks

and mediators. The nucleons fall into the category of baryons that are bound states of three quarks. There are 6 flavors of quarks: up(u), down(d), charm(c), strange(s), top(t), and bottom(b). The collection of quarks and their electric charges is listed in Table 1.1.

	$Q = 2/3e$	$Q = -1/3e$
First generation	u	d
Second generation	c	s
Third generation	t	b

Table 1.1: Collection of six flavors of quarks and their electric charges. Quarks in higher generation have higher mass.

In the basic quark model, the proton consists of two up quarks and one down quark, and the neutron consists of two down quarks and one up quark. The model gives a simple yet remarkable explanation of the anomalous magnetic moment of the nucleons. For example, the spin/flavor wave function of a proton with spin up can be written as[24]:

$$\begin{aligned} |p\uparrow\rangle = \sqrt{\frac{1}{18}}\,[&2|u\uparrow d\downarrow u\uparrow\rangle + 2|u\uparrow u\uparrow d\downarrow\rangle + 2|d\downarrow u\uparrow u\uparrow\rangle \\ &-|u\uparrow u\downarrow d\uparrow\rangle - |u\downarrow u\uparrow d\uparrow\rangle - |u\uparrow d\uparrow u\downarrow\rangle \\ &-|u\downarrow d\uparrow u\uparrow\rangle - |d\uparrow u\uparrow u\downarrow\rangle - |d\uparrow u\downarrow u\uparrow\rangle] \\ = \quad &\frac{2}{3\sqrt{2}}\,[2|u\uparrow u\uparrow d\downarrow\rangle - |u\uparrow u\downarrow d\uparrow\rangle - |d\uparrow u\uparrow u\downarrow\rangle] + permutations \end{aligned} \tag{1.2}$$

The magnetic moment of the proton is:

$$\begin{aligned} \mu_p &= \langle p\uparrow|(\mu_1+\mu_2+\mu_3)_z|p\uparrow\rangle \\ &= \frac{2}{\hbar}\sum_{i=1}^{3}\langle p\uparrow|\mu_i S_{i_z}|p\uparrow\rangle \\ &= \frac{1}{3}(4\mu_u - \mu_d) \end{aligned} \tag{1.3}$$

where $\mu_u = (\frac{2}{3}e)\hbar/2m_u c$ and $\mu_d = (-\frac{1}{3}e)\hbar/2m_d c$ are the magnetic moment of the

quarks. Similar calculation for neutron yields:

$$\mu_n = \frac{1}{3}(-\mu_u + 4\mu_d) \tag{1.4}$$

Using constituent quark masses $m_u = m_d = 336$ MeV/c^2, we have:

$$\begin{aligned} \mu_p &= 2.79 \cdot \mu_N \\ \mu_n &= -1.86 \cdot \mu_N \end{aligned} \tag{1.5}$$

which is very close to the experimental value of the magnetic moments of the nucleon. In fact, with some assumption on the masses of the constituent quarks, this basic quark model brought up by Gell-mann[25] and Zweig[26] in 1964 has roughly the correct prediction on both the magnetic moments and masses of all mesons and baryons. It also received further support from the deep inelastic scattering experiments at SLAC around 1970[27]. However, later experiments showed that neither the mass nor the spin of the nucleon comes only from the three constituent quarks. In the most accepted understanding as of today, the constituent(or valence) quarks contributes around only 1% to the nucleon mass and around 30% to the nucleon spin. In modern perspective, the nucleon is a rather complex particle composed of valence quarks, gluons, and sea quarks. The interactions between them, which is governed by Quantum Chromodynamics(QCD), contributes to most of the nucleon mass. The spin of the nucleon is a combination of the quark spin, angular momentum of the quarks, the gluon spin, and the angular momentum of the gluons. Despite the success of QCD at short distances (i.e. very high momentum transfers) where quarks are *asymptotically free* and perturbative technique can be applied, a complete description of the nucleon is still missing.

Experimentally, physicists use highly energetic particles such as electrons hitting on the nucleon to probe the inner structure of the nucleon. The method is known as scattering experiment. Over the last few decades, results from scattering experiments have provides a highly effective testing ground for theories and have brought many insights to our understanding of the nucleon structure.

1.2 Electron elastic scattering from nucleon

The elastic scattering of an electron off of a nucleon is a scattering process that occurs when an electron beam scatters from a nucleon target without breaking the nucleon or exciting it into a higher energy state. In other words, the nucleon stays intact and in its ground state. The process is well understood and calculable by Quantum Electrodynamics (QED). The cross section of this process is closely related to the nucleon electromagnetic structure characterized by the nucleon form factors. As a matter of fact, electron scattering experiments are limited to studying only the electromagnetic features of the nucleon (at least in a direct way), as there is no strong interaction between the electron and nucleon's components involved. The gluons, which interact only through strong interaction, can not be directly studied in such experiments. Despite this drawback, electron scattering experiments are still one of the most effective tools to study the nucleon structure. In this section we will discuss the cross section of the electron elastic scattering from a nucleon within the QED framework.

1.2.1 Kinematics

Before diving into discussion of the cross section of the electron elastic scattering from a nucleon, it is useful to review the kinematics of the scattering process. We will be using many of the conclusions from here in the next sections to derive the cross section. First, we define the direction of the momentum of the incoming electron as the z axis. Then we define the scattering plane as the x-z plane and the y axis to be perpendicular to the x-z plane to form a system of 3D Cartesian coordinates which follows the right hand rule. The kinematics of the scattering process is shown in Figure 1-1. Here we assume the target nucleon to be free and initially at rest. The

four momenta of the electron and the target particle are:

$$\begin{cases} p_e = (E_e, \vec{p_e}) = (E_e,\ 0,\ 0,\ |\vec{p_e}|) \\ p'_e = (E'_e, \vec{p_e}') = (E'_e,\ |\vec{p_e}'|sin\theta,\ 0,\ |\vec{p_e}'|cos\theta) \\ p_N = (m, 0) \\ p'_N = (E'_N, \vec{p_N}') = (E'_N,\ |\vec{p_N}'|sin\phi,\ 0,\ |\vec{p_N}'|cos\phi) \end{cases} \tag{1.6}$$

From momentum and energy conservation we have the following relations:

$$\begin{aligned} E'_e &= \frac{E_e}{1 + \frac{2E_e}{m} sin^2\frac{\theta}{2}} & \nu &= E_e - E'_e & Q^2 &= 2E_eE'_e(1 - cos\theta) \\ p_e \cdot p'_e &= \frac{Q^2}{2} & p_e \cdot p_N &= E_em & p_e \cdot p'_N &= E_em - \frac{Q^2}{2} \\ p'_e \cdot p_N &= E_em - \frac{Q^2}{2} & p'_e \cdot p'_N &= -E_em & p_N \cdot p'_N &= m^2 + \frac{Q^2}{2} \end{aligned} \tag{1.7}$$

where $Q^2 = -q^2$ with $q = (\nu, \vec{q})$ being the four momentum transfer squared of the virtual photon in the leading order of the scattering process where only a single photon is exchanged. In the above relations we have neglected electron mass since it is much smaller than the mass of the target nucleon.

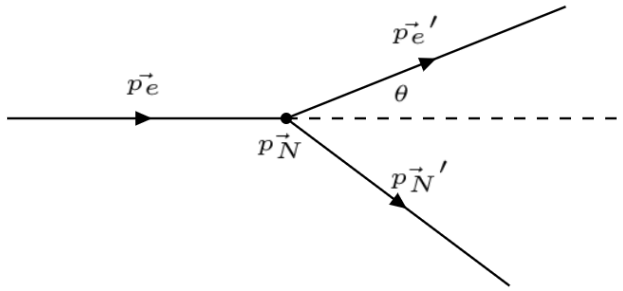

Figure 1-1: Kinematic of the elastic scattering process of an electron from nucleon

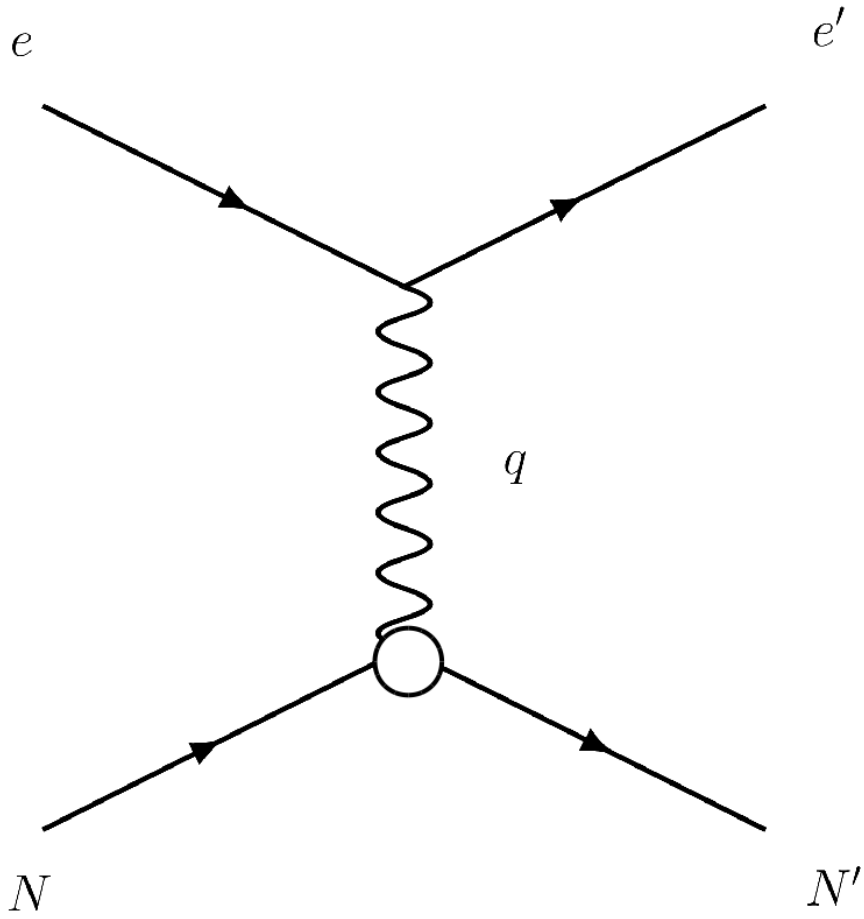

Figure 1-2: First order Feynman diagram of electron nucleon elastic scattering

1.2.2 Cross Section

In the one photon exchange approximation, the amplitude of the elastic scattering of a electron from a nucleon can be read from the first order Feynman diagram as shown in Figure 1-2:

$$\mathcal{M} = (2\pi)^4 \int [\bar{u}(p'_e, s'_e)(ig_e\gamma^\mu)u(p_e, s_e)]\frac{-ig_{\mu\nu}}{q^2}[\bar{u}(p_N{}', s_N{}')(-ig_e\Gamma^\nu)u(p_N, s_N)] \\ \delta^4(p_e - p'_e - q)\delta^4(p_p - p'_p + q)d^4q \tag{1.8}$$

The u and $\bar{u}$ are respectively the Dirac spinors and their adjoints ($\bar{u} = u^\dagger\gamma^0$). The p_e and p'_e are respectively the initial and final four momenta of the electron. The p_N and $p_N{}'$ are respectively the initial and final four momenta of the nucleon. The s_e, s'_e,

s_N and $s_N{}'$ are the initial and final spin four-vectors of the electron and nucleon. The $g_e = \sqrt{4\pi\alpha}$ where α is the fine-structure constant of electromagnetism with $\alpha = \frac{e^2}{\hbar c}$. γ^μ is one of the Dirac matrices. $q^2 = p'_e - p_e = p_N - p_N{}'$ is the four-momentum transfer squared and the term $-ig_e\Gamma^\nu$ denotes the nucleon vertex factor. After the integration over q and the contraction of the Minkowski metric tensor $g_{\mu\nu}$ (and replacement of ν with μ), the amplitude becomes:

$$\mathcal{M} = \frac{e^2}{Q^2}\left[\bar{u}(p'_e, s'_e)\gamma_\mu u(p_e, s_e)\right]\left[\bar{u}(p_N{}', s_N{}')\Gamma^\mu u(p_N, s_N)\right] \tag{1.9}$$

In the equation above, the Γ^μ represents structure of the nucleon. In the lowest order Γ^μ should be equal to γ^μ, where the nucleon is considered as a point particle. In the general form, Γ^μ should be a function of q, p_N and $p_N{}'$. With using a method analogous to [28], it can be shown that the Γ^μ takes the form of:

$$\Gamma^\mu = \gamma^\mu F_1(q^2) + \frac{i\sigma^{\mu\nu}q_\nu}{2m}F_2(q^2) \tag{1.10}$$

where $\sigma^{\mu\nu} = \frac{i}{2}\left[\gamma^\mu, \gamma^\nu\right]$. The $F_1(q^2)$ and $F_2(q^2)$ are functions of q^2 know as form factors. In the lowest order, $F_1(q^2) = 1$ and $F_2(q^2) = 0$, then Γ^μ returns to γ^μ. For convenience of later calculation of the amplitude squared, it is useful to re-express Γ using the Gordon identity:

$$\bar{u}(p_N{}', s_N{}')\gamma^\mu u(p_N, s_N) = \bar{u}(p_N{}', s_N{}')\left[\frac{i\sigma^{\mu\nu}q_\nu}{2m} + \frac{p_N{}'^\mu + p_N{}^\mu}{2m}\right]u(p_N, s_N) \tag{1.11}$$

With this, Γ^μ becomes:

$$\Gamma^\mu = \gamma^\mu[F_1(q^2) + F_2(q^2)] - \frac{p_N{}'^\mu + p_N{}^\mu}{2m}F_2(q^2) \tag{1.12}$$

Plug 1.12 back into 1.9, we have:

$$\begin{aligned}\mathcal{M} =& \frac{e^2}{q^2}\left[\bar{u}(p'_e, s'_e)\gamma_\mu u(p_e, s_e)\right] \\ &\cdot\left[\bar{u}(p_N{}', s_N{}')\left[\gamma^\mu[F_1(q^2) + F_2(q^2)] - \frac{p_N{}'^\mu + p_N{}^\mu}{2m}F_2(q^2)\right]u(p_N, s_N)\right]\end{aligned} \tag{1.13}$$

Now we can calculate the $\overline{|\mathcal{M}|^2}$. To do that We need to average $|\mathcal{M}|^2$ the over all initial spins and sum it over all final spins, which gives:

$$\begin{aligned}\overline{|\mathcal{M}|^2} =& \frac{1}{2}\cdot\frac{1}{2}\cdot\sum_{s_e}\sum_{s_e{}'}\sum_{s_N}\sum_{s_N{}'}\frac{e^4}{q^4} \\ &\cdot[\bar{u}(p_e',s_e')\gamma_\mu u(p_e,s_e)] \\ &\cdot\left[\bar{u}(p_N{}',s_N{}')\left[\gamma^\mu[F_1(q^2)+F_2(q^2)]-\frac{p_N{}'^\mu+p_N{}^\mu}{2m}F_2(q^2)\right]u(p_N,s_N)\right] \\ &\cdot[\bar{u}(p_e',s_e')\gamma_\nu u(p_e,s_e)]^* \\ &\cdot\left[\bar{u}(p_N{}',s_N{}')\left[\gamma^\nu[F_1(q^2)+F_2(q^2)]-\frac{p_N{}'^\nu+p_N{}^\nu}{2m}F_2(q^2)\right]u(p_N,s_N)\right]^*\end{aligned} \tag{1.14}$$

Using Casimir's trick[24]:

$$\sum_{allspins}[\bar{u}(a)\Gamma_1 u(b)][\bar{u}(a)\Gamma_1 u(b)]^* = Tr[\Gamma_1(\not{p}_b+m_bc)\bar{\Gamma_2}(\not{p}_a+m_ac)] \tag{1.15}$$

where $\bar{\Gamma_2}=\gamma^0\Gamma_2^\dagger\gamma^0$.
The averaged amplitude becomes:

$$\overline{|\mathcal{M}|^2}=\frac{e^4}{4Q^4}\cdot Tr[\gamma_\mu(\not{p}_e'+m_e)\gamma_\nu(\not{p}_e+m_e)]\cdot Tr[\Gamma_\mu(\not{p}_N'+m)\Gamma_\nu(\not{p}_N+m)] \tag{1.16}$$

The first trace term relates only to the electron initial and final states can be easily evaluated:

$$\begin{aligned}&Tr[\gamma_\mu(\not{p}_e+m_e)\gamma_\nu(\not{p}_e'+m_e)] \\ =&\, Tr(\gamma^\mu\not{p}_e\gamma^\nu\not{p}_e')+m_eTr(\gamma^\mu\not{p}_e\gamma^\nu+\gamma^\mu\gamma^\nu\not{p}_e')+m^2c^2Tr(\gamma^\mu\gamma^\nu) \\ =&\, 4[p_e^\mu p_e'^\nu+p_e'^\mu p_e^\nu+g^{\mu\nu}(m^2c^2-p_e\cdot p_e')]\end{aligned} \tag{1.17}$$

The second trace term relates to the nucleon initial and final states and its form factor:

$$
\begin{aligned}
& Tr[\Gamma_\mu(\not{p}'_N + m)\Gamma_\nu(\not{p}_N + m)] \\
&= Tr\left\{\left[\gamma^\mu(F_1+F_2) - \frac{{p_N}'^\mu + p_N{}^\mu}{2m}F_2\right](\not{p}'_N + m)\right. \\
&\quad \left.\left[\gamma^\nu(F_1+F_2) - \frac{{p_N}'^\nu + p_N{}^\nu}{2m}F_2\right](\not{p}_N + m)\right\} \\
&= (F_1+F_2)^2 \cdot Tr[(\gamma^\mu \not{p}'_N + m)\gamma^\nu(\not{p}_N + m)] \\
&\quad + \frac{(F_1+F_2)F_2}{2m}\left\{({p_N}'^\nu + p_N{}^\nu)Tr[\gamma^\mu(\not{p}_N + m)(\not{p}'_N + m)]\right. \\
&\qquad\qquad \left. +({p_N}'^\mu + p_N{}^\mu)Tr[(\not{p}_N + m)\gamma^\nu(\not{p}'_N + m)]\right\} \\
&\quad + \frac{F_2^2}{m^2}({p_N}'^\mu + p_N{}^\mu)({p_N}'^\nu + p_N{}^\nu)Tr[(\not{p}_N + m)(\not{p}'_N + m)] \\
&= 4(F_1+F_2)^2[p_N{}^\mu {p_N}'^\nu + {p_N}'^\mu p_N{}^\nu + g^{\mu\nu}(m^2c^2 - p_N \cdot {p_N}')] \\
&\quad + 4\left[\frac{{p_N}' \cdot p_N + m^2}{4m^2}F_2^2 - (F_1+F_2)F_2\right]({p_N}'^\mu + p_N{}^\mu)({p_N}'^\nu + p_N{}^\nu)
\end{aligned}
\tag{1.18}
$$

note that here we omitted the q^2 within the form factors F_1 and F_2 just for cleanliness in the derivation, the form factors are still functions of q^2.

Plug 1.17 and 1.18 back into 1.16 and do the contraction, now we have:

$$
\begin{aligned}
\overline{|\mathcal{M}|^2} = \frac{8e^4}{Q^4}\Bigg\{ & (F_1+F_2)^2[({p_e}' \cdot {p_N}')(p_e \cdot p_N) + ({p_e}' \cdot p_N)(p_e \cdot {p_N}') \\
& \qquad -m^2({p_e}' \cdot p_e) - m_e^2({p_N}' \cdot p_N) + 2m^2m_e^2] \\
& + \left[\frac{{p_N}' \cdot p_N + m^2}{4m^2}F_2^2 - (F_1+F_2)F_2\right] \\
& \left[p_e \cdot (p_N + {p_N}')\ {p_e}' \cdot (p_N + {p_N}') - \frac{1}{2}(m^2c^2 - p_e \cdot p'_e)(p_N + {p_N}')^2\right]\Bigg\}
\end{aligned}
\tag{1.19}
$$

Using the result of the dot product of the four momentum in 1.7, we have:

$$
\overline{|\mathcal{M}|^2} = \frac{4e^4m^2}{Q^2}\left[\left(F_1^2 + \tau F_2^2\right)cot^2\frac{\theta}{2} + 2\tau(F_1+F_2)^2\right] \tag{1.20}
$$

Now that we have the averaged amplitude we can compute the cross section of the scattering based on the golden rule (again ignoring electron mass):

$$\begin{aligned}
d\sigma &= \frac{1}{4mE_e}\overline{|\mathcal{M}|^2}(2\pi)^4\delta^4(p_e + p_N - p'_e - p'_N)\frac{1}{2E'_e(2\pi)^3}\frac{1}{2E'_N(2\pi)^3}d^3p'_e d^3p'_N \\
&= \frac{1}{4mE_e}\overline{|\mathcal{M}|^2}\delta(E_e + m - E'_e - E'_p)\frac{1}{16\pi^2 E'_e E'_p}d^3p'_e \\
&= \frac{1}{64\pi^2 mE_e}\overline{|\mathcal{M}|^2}\frac{E'_e}{m + 2Esin^2\frac{\theta}{2}}d\Omega \\
&= \frac{1}{64\pi^2 m^2}\left(\frac{E'_e}{E_e}\right)^2\overline{|\mathcal{M}|^2}d\Omega \\
&= \frac{e^4}{16\pi^2 Q^2}\left(\frac{E'_e}{E_e}\right)^2\left[\left(F_1^2 + \tau F_2^2\right)cot^2\frac{\theta}{2} + 2\tau(F_1 + F_2)^2\right]d\Omega
\end{aligned} \tag{1.21}$$

Thus, we have the Rosenbluth Formula for the differential cross section:

$$\frac{d\sigma}{d\Omega} = \frac{\alpha^2}{4E_e^2 sin^2\frac{\theta}{2}}\frac{E'_e}{E_e}\left[\left(F_1^2 + \tau F_2^2\right)cot^2\frac{\theta}{2} + 2\tau(F_1 + F_2)^2\right] \tag{1.22}$$

where $\alpha = \frac{e^2}{4\pi}$, $\tau = \frac{Q^2}{4m^2}$, and $Q^2 = 4E_eE'_esin^2\frac{\theta}{2}$ being the four momentum squared of the virtual photon. It is also common to express the cross section in another choice of form factors called Sachs electric and magnetic form factors and they are:

$$\begin{aligned}
G_E(Q^2) &= F_1(Q^2) - \tau F_2(Q^2) \\
G_M(Q^2) &= F_1(Q^2) + F_2(Q^2)
\end{aligned} \tag{1.23}$$

With the Sachs form factors, the cross section becomes:

$$\frac{d\sigma}{d\Omega} = \frac{\alpha^2}{4E_e^2 sin^2\frac{\theta}{2}}\frac{E'_e}{E_e}\left[\frac{G_E^2 + \tau G_M^2}{1+\tau}cot^2\frac{\theta}{2} + 2\tau G_M^2\right]. \tag{1.24}$$

G_E and G_M characterize the electric and magnetic structure of the nucleon. At very low Q^2, where the wave length of the virtual photon is too large to be sensitive to the inner structure of the nucleon, the nucleon would just behave like a point like particle while G_E and G_M become the nucleon charge and the anomalous magnetic moment respectively. More detailed physical meaning of the Sachs form factors will

be discussed in the next chapter.

Chapter 2

Electromagnetic Form Factors

In the last chapter we arrived at the Rosenbluth Formula 1.24 for the elastic scattering of an electron from a nucleon. The inner structure of the nucleon has been factorized into the electromagnetic form factors G_E and G_M which are function of the four momentum transfer squared. In this chapter we will discuss the relation between these form factors and the electromagnetic structure of nucleon, experimental techniques to measure these form factors, existing data on them and the importance of the form factors in testing and verifying theoretical models of the nucleons.

2.1 Physical Meaning

The nucleons have a rich and complex inner structure. The elastic scattering of an electron off a nucleon can be regarded as an act of probing the nucleon's substructure using the electron. A certain structure of the nucleon would result in a certain form of G_E and G_M in the Rosenbluth Formula 2.1. The form factors G_E and G_M describe a certain structure.

$$\frac{d\sigma}{d\Omega} = \frac{\alpha^2}{4E_e^2 sin^2\frac{\theta}{2}} \frac{E'_e}{E_e} \left[\frac{G_E^2 + \tau G_M^2}{1+\tau} cot^2\frac{\theta}{2} + 2\tau G_M^2 \right] \tag{2.1}$$

For a structureless charge $+e$ spin $\frac{1}{2}$ particle, it is clear that both G_E and G_M reduce to 1. For a target particle like a nucleon with inner structure, G_E and G_M are

closely related to the charge and magnetic moment distributions of the nucleon.

2.1.1 Form Factors in Low momentum transfer

First let's look at the meaning of the form factors in the limit of $Q^2 \ll 0$. In this limit, the energy transfer $\nu = \frac{Q^2}{2m} \ll 0$, which means the recoil of the proton is negligible. In such a case, the nucleon can be considered a static charge cloud and the form factors G_E and G_M can be shown to be respectively the Fourier transform of the nucleon's charge and magnetic moment distribution[28]. For instance G_E can be written as:

$$\begin{aligned} G_E(\mathbf{q}) &= \int \rho(\mathbf{x}) e^{i\mathbf{q}\cdot\mathbf{x}} d^3x \\ &= \int \left(1 + i\mathbf{q}\cdot\mathbf{x} - \frac{(\mathbf{q}\cdot\mathbf{x})^2}{2} + \dots\right) \\ &= 1 - \frac{1}{6}|\mathbf{q}|^2\langle r^2\rangle + \dots \end{aligned} \tag{2.2}$$

where $\langle r^2\rangle$ is the mean of the charge radius, and $|\mathbf{q}|^2 = Q^2$ since $\nu \to 0$. Here we see how G_E directly relates to the size of the charge distribution of the nucleon in the limit of small Q^2. To the lowest order of Q^2, we have a simple relation:

$$\langle r^2\rangle = -6 \left.\frac{dG_E}{dQ^2}\right|_{Q^2=0} \tag{2.3}$$

Given the factor of the G_M^2 terms $\tau = \frac{Q^2}{4m^2} \to 0$ and the cross section in 2.1 will be dominated by G_E:

$$\frac{d\sigma}{d\Omega} = \frac{\alpha^2}{4E_e^2 sin^2\frac{\theta}{2}} \frac{E_e'}{E_e} \frac{G_E^2}{1+\tau} cot^2\frac{\theta}{2} \tag{2.4}$$

Equations 2.3 and 2.4 provide a way of measuring the nucleon charge radius by measuring the cross section at very low Q^2. The PRad experiment at Jefferson Laboratory adopted this as the basic method for the high precision measurement of the charge radius of the proton[29]. Here the form factors describe only the mean size of the charge distribution instead of a more detailed description. This is as expected because in the limit of $Q^2 \to 0$ the virtual photon has a relative large wavelength and it is

hard to detect the nucleon's inner structure.

2.1.2 Form Factors in Breit Frame

A more general way of describing the physical meaning of the Sachs form factors without limiting the range of Q^2 can be done in the Breit frame. By definition, there is no energy transfer to the nucleon in the Breit frame which means $\nu = 0$ and $\mathbf{p_N} = -\mathbf{p'_N}$. The nucleon transition current $\mathcal{J}^\mu_N \equiv (\rho, \mathbf{J}) = \bar{u}(p'_N)\Gamma^\mu u(p_N)$ can be expressed with identity 1.12 as follows:

$$\begin{aligned}\mathcal{J}^\mu_N &= \bar{u}(p'_N)\left[\gamma^\mu[F_1(q^2)+F_2(q^2)] - \frac{{p_N}'^\mu + {p_N}^\mu}{2m}F_2(q^2)\right]u(p_N) \\ &= \bar{u}(p'_N)\left[\gamma^\mu G_M + \frac{{p_N}'^\mu + {p_N}^\mu}{2m}\frac{G_E - G_M}{1+\tau}\right]u(p_N)\end{aligned} \tag{2.5}$$

Take the $\mathcal{J}^0_N$ for example:

$$\begin{aligned}\mathcal{J}^0_N \equiv \rho &= \bar{u}(p'_N)\left[\gamma^0 G_M + \frac{{p_N}'^0 + {p_N}^0}{2m}\frac{G_E - G_M}{1+\tau}\right]u(p_N) \\ &= G_M\bar{u}(p'_N)\gamma^0 u(p_N) + \frac{2E}{2m}\frac{G_E - G_M}{1+\tau}\bar{u}(p'_N)u(p_N) \\ &= 2mG_E{\chi'}^\dagger\chi\end{aligned} \tag{2.6}$$

Here we see how the electric form factor relates to the nucleon charge density in the Breit frame. A similar analysis can be done for the other components of the transition current and results in:

$$\vec{\mathcal{J}}_N = 2iG_M{\chi'}^\dagger(\vec{\mathbf{p_N}} \times \vec{\sigma})\chi \tag{2.7}$$

where $\vec{\sigma}$ is the Pauli vector.

However, there is great difficulty in translating these relations back to the lab frame since the Breit frame is different for different four momentum transfer squared Q^2. Nonetheless, the electromagnetic form factors are tightly bound to the structure of the nucleon and are great test ground for theories that predict a certain nucleon structure.

2.2 Form Factors Measurement

The nucleon electromagnetic form factors have been studied for decades in elastic scattering experiments. In the early days the form factors were extracted from the cross section of the scattering process by the Rosenbluth method. This method requires accurate measurement of the cross section and suffers from large system uncertainty in high four momentum transfer squared Q^2 range. With the advancement in polarized electron beam and polarized target technology, another method of measuring polarization transferred to recoil nucleon or asymmetry in cross section with polarized target made possible precise measurement of the electromagnetic form factors at high Q^2 value. The result of the form factors using the polarization method lead to a significant breakthrough in the understanding of nucleons. In this section we will introduce the two methods and discuss the discrepancy in the value of form factors between these two methods.

2.2.1 Rosenbluth Separation

Based on the Rosenbluth Formula 2.1, the "reduced" cross section σ_{red} can be written as:

$$\sigma_{red} \equiv \frac{\epsilon(1+\tau)}{\tau}\left(\frac{d\sigma}{d\Omega}\right)_N / \left(\frac{d\sigma}{d\Omega}\right)_{Mott} = \frac{\epsilon}{\tau}G_E^2 + G_M^2 \tag{2.8}$$

where $\left(\frac{d\sigma}{d\Omega}\right)_{Mott}$ is the Mott cross section for elastic scattering of an electron from a spinless point-like charged particle and ϵ is the polarization of the virtual photon with:

$$\begin{aligned}\left(\frac{d\sigma}{d\Omega}\right)_{Mott} &= \frac{\alpha^2 cos^2\frac{\theta}{2}}{4E_e^2 sin^4\frac{\theta}{2}} \\ \epsilon &= \left[1 + 2(1+\tau)tan^2\frac{\theta}{2}\right]^{-1}\end{aligned} \tag{2.9}$$

It is clear that when τ is fixed, the reduced cross section σ_{red} has a linear dependence on ϵ. By plotting σ_{red} vs. ϵ we can get the G_E^2 from the slope and G_M^2 from the intercept. This is called the Rosenbluth separation technique. Many ex-

periments have adopted this method to measure the nucleon form factors since the 1960s[1][2][3][4][5][6]. The results of the proton electric form factor G_{Ep} from these experiments are shown in Figure 2-1. As can be seen from Figure 2-1, the uncertainty

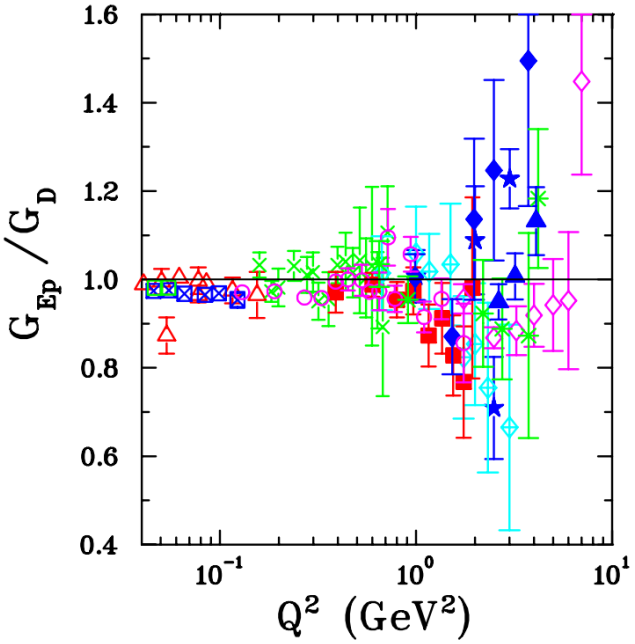

Figure 2-1: The proton electric form factor G_{Ep} normalized to the dipole form factor measured by experiments using Rosenbluth separation technique. The data points and their origin are: [1]-open red triangle, [2]-green star, [3]-red square, [4]-green open square, [5]-green asterisk and [6]-blue triangle. Plot reproduced from [7]

of the form factor increases significantly with Q^2. This is because with increasing Q^2, $\tau = \frac{Q^2}{4m}$ increases and thus the contribution of the G_M term which has the factor τ in the Rosenbluth Formula 2.1 is much larger compared to the G_E term. Because of the dominance of the G_M term, the extraction of the electric form factor G_E becomes very difficult and suffers from huge uncertainties. In addition, the Rosenbluth separation is based on the linear ϵ dependence of the σ_{red} which comes from the one-photon exchange approximation in the elastic scattering. However, radiative corrections have to be made. The two-photon exchange channel could also contribute to the linearity and can not be corrected from experimental data and careful theoretical calculations have to be made[30].

2.2.2 Polarization Method

The method of utilizing polarization variables to measure the nucleon form factors was brought up around the 1960s[31]. However it wasn't until decades later when a good quality polarized beam and polarized target was available that experiments using the polarization method were able to measure the form factors with good accuracy. In this section we will briefly discuss the two types of experiments that use polarization variables in the scattering process.

Recoil Polarization

The recoil polarization method examines the polarization transfer in the elastic scattering of a longitudinally polarized electron from a unpolarized target. In the process the polarization of the electron is transferred to the nucleon as[32][33]:

$$I_0 P_l = h\sqrt{\tau(1+\tau)} tan^2\frac{\theta_e}{2}\frac{E_e + E'_e}{M} G_M^2 \tag{2.10}$$

$$I_0 P_t = -2h\sqrt{\tau(1+\tau)} tan\frac{\theta_e}{2} G_E G_M \tag{2.11}$$

$$I_0 P_n = 0 \tag{2.12}$$

$$I_0 = G_E^2 + \frac{\tau}{\epsilon} G_M^2 \tag{2.13}$$

where P_t and P_l are the polarization component of the recoil proton perpendicular and parallel to the proton momentum in the scattering plane, P_n is the polarization component of the recoil proton perpendicular to the scattering plane, $h = \pm 1$ is the helicity of the electron, $\tau = \frac{Q^2}{4m_p^2}$, m_p is the proton mass, E_e and E'_e are the energy of the initial and final electron and θ_e is the scattering angle. Thus the ratio of the two polarization components can be related to the ratio of the form factors:

$$\frac{G_E}{G_M} = -\frac{P_t}{P_l}\frac{E_e + E'_e}{2m_p} tan\frac{\theta_e}{2} \tag{2.14}$$

This method has the following advantage over the Rosenbluth separation method. First, it requires only one single measurement of the azimuthal angular distribution

of the recoil nucleon in a polarimeter to measure the longitudinal and transverse polarization P_l and P_t as apposed to several measurement points at different ϵ to extract the slope and intercept of linear relation between σ_{red} and ϵ. Second, the precision of electric form factor measurements at high four momentum transferred value squared Q^2 is far greater than that using the Rosenbluth separation method because the form factor ratio relates only to the ratio of the polarization components. Third, many of the systematic uncertainties which enter the Rosenbluth method such as the beam current, target thickness, spectrometer acceptance, detector efficiencies etc. cancel in the ratios in the polarization transfer method. This makes the recoil polarization method enjoy very low systematic uncertainties. Historical data of the proton electric form factors ratio using the polarization method is shown in Figure 2-2

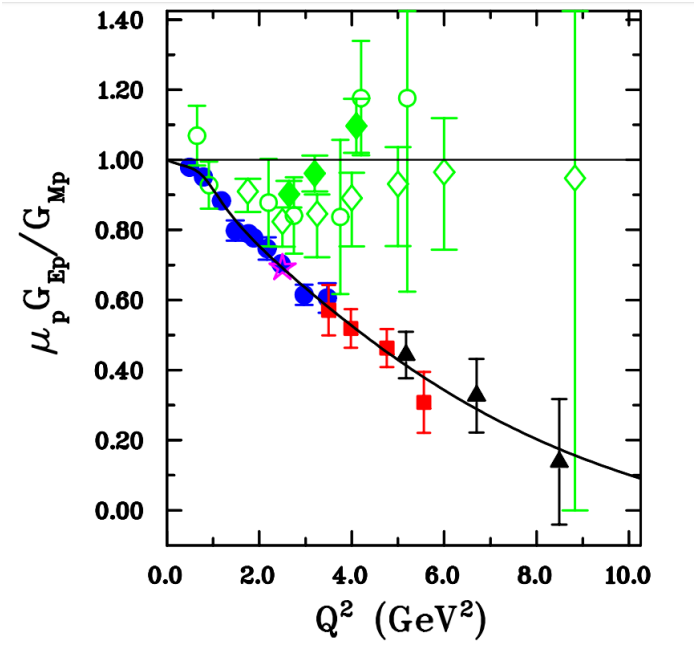

Figure 2-2: The proton electric form factor ratio $\mu_p G_{Ep}/G_{Mp}$ extracted using the recoil polarization method and using the Rosenbluth separation method. The blue circle, red square and black triangle are respectively data from the *GEp*-I, *GEp*-II and *GEp*-III experiment at Jefferson Laboratory. The rest of the data points are from experiments using the Rosenbluth separation method. The black curve is a parameter fit on the JLab data. The data points from recoil polarization experiments offer much higher precision at high Q^2. Plot reproduced from [7].

Double Polarization

Another polarization method uses a polarized electron beam and polarized target such as ${}^3\vec{H}e$. In this section we will briefly describe the principle behind the experiment. A more detailed discussion can be found in [34] [35]. In the Born approximation, the elastic electron nucleon scattering cross section can be written in terms of the beam helicity as:

$$\sigma_h = \Sigma + h\Delta \tag{2.15}$$

where Σ is the unpolarized elastic differential cross section and Δ is the polarized part. The unpolarized cross section can be written as:

$$\Sigma = \frac{d\sigma}{d\Omega}\Big|_{Mott} \frac{E_f}{E_i}\left(\frac{G_E^2 + \tau G_M^2}{1+\tau} + 2\tau G_M^2 tan^2\frac{\theta}{2}\right) \tag{2.16}$$

where E_f is the final energy of the electron, E_i is the initial energy of the electron, $\tau = \frac{Q^2}{4M^2}$, Q^2 is the square of the four-momentum transfer, M is the mass of the target, G_E and G_M are the Sachs Electric and Magnetic form factors, and $\frac{d\sigma}{d\Omega}\Big|_{Mott}$ is the Mott cross section describing the scattering of an electron from a point-like target:

$$\frac{d\sigma}{d\Omega}\Big|_{Mott} = \frac{\alpha^2 cos^2\frac{\theta}{2}}{4E_i^2 sin^4\frac{\theta}{2}} \tag{2.17}$$

The polarized part of the cross section can be written as:

$$\Delta = -2\frac{d\sigma}{d\Omega}\Big|_{Mott} \frac{E_f}{E_i}\sqrt{\frac{\tau}{1+\tau}}tan\frac{\theta}{2} \left[\sqrt{\tau(1+(1+\tau)tan^2(\frac{\theta}{2}))}cos\theta^* G_M^2 + sin\theta^* cos\phi^* G_M G_E\right] \tag{2.18}$$

where θ is the scattering angle of the electron noted as θ_e in Figure 2-3, the θ^* and ϕ^* are respectively the polar angle and azimuthal angle of the polarization of the target relative to the direction of the momentum transfer.

The asymmetry of the cross section between helicity +1 and -1 is:

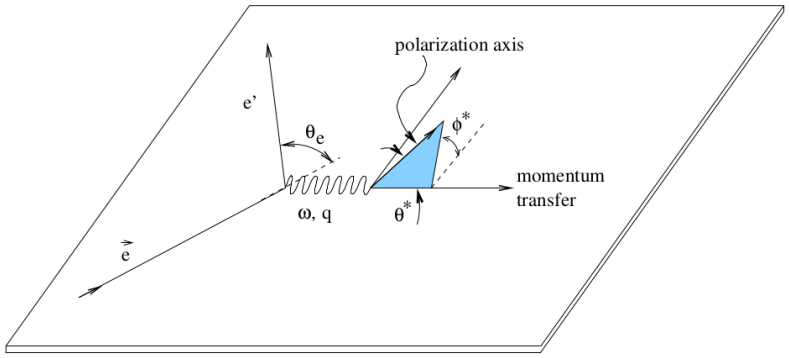

Figure 2-3: The kinematics of electron scattering from a polarized nucleon.

$$A_{phys} = \frac{\sigma_+ - \sigma_-}{\sigma_+ + \sigma_-} = \frac{\Delta}{\Sigma} \tag{2.19}$$

Combine 2.19 with 2.16 and 2.18, and the asymmetry can be written as:

$$\begin{aligned} A_{phys} = &- \frac{2\sqrt{\tau(\tau+1)}tan\frac{\theta}{2}G_E^n G_M^n sin\theta^* cos\phi^*}{(G_E^n)^2 + (G_M^n)^2(\tau + 2\tau(1+\tau)tan^2\frac{\theta}{2})} \\ &- \frac{2\tau\sqrt{1+\tau+(1+\tau)^2 tan^2\frac{\theta}{2}}tan\frac{\theta}{2}(G_M^n)^2 cos\theta^*}{(G_E^n)^2 + (G_M^n)^2(\tau + 2\tau(1+\tau)tan^2\frac{\theta}{2})} \end{aligned} \tag{2.20}$$

The asymmetry is usually written in terms of the perpendicular asymmetry $A_\perp$(when the target spin is perpendicular to the momentum transfer) and longitudinal asymmetry $A_\parallel$ as:

$$A_{phys} = A_\perp sin\theta^* cos\phi^* + A_\parallel cos\theta^* \tag{2.21}$$

where

$$A_\perp = -\frac{2\sqrt{\tau(\tau+1)}tan\frac{\theta}{2}\frac{G_E^n}{G_M^n}}{\frac{G_E^n}{G_M^n}^2 + (\tau + 2\tau(1+\tau)tan^2\frac{\theta}{2})} \tag{2.22}$$

and

$$A_\parallel = -\frac{2\tau\sqrt{1+\tau+(1+\tau)^2 tan^2\frac{\theta}{2}}tan\frac{\theta}{2}}{\frac{G_E^n}{G_M^n}^2 + (\tau + 2\tau(1+\tau)tan^2\frac{\theta}{2})} \tag{2.23}$$

The ratio of neutron form factors G_E^n/G_M^n is the quantity we aim to measure. Since it appears in the numerator of the perpendicular asymmetry $A_\perp$, we can maximize

the contribution of $A_\perp$ in 2.21 to minimize the uncertainty of G_E^n/G_M^n. Thus the optimum value for θ and ϕ are respectively 90° and 0°/180°, which means the target polarization is aligned perpendicular to the momentum transfer $\vec{\mathbf{q}}$ and within the scattering plane. In such an ideal condition, the relation between A_{phys} and form factor ratio G_E^n/G_M^n is:

$$A_{phys} = -\frac{2\sqrt{\tau(\tau+1)}tan\frac{\theta}{2}\frac{G_E^n}{G_M^n}}{\frac{G_E^n}{G_M^n}^2 + (\tau + 2\tau(1+\tau)tan^2\frac{\theta}{2})} \tag{2.24}$$

Once the asymmetry $A_{phys}$is measured, the neutron form factor ratio G_E^n/G_M^n can be easily extracted.

2.3 History data on Form Factors

2.3.1 Proton Form Factors Data

In earlier experiments before high quality polarized beam was available, both proton electric and magnetic form factors were studied using the Rosenbluth separation technique. The proton magnetic form factor G_M^p is the easiest to measure and known up to Q^2 value as high as 30 GeV^2. A collection of G_M^p data is shown in Figure 2-4. It is worth noting that the data points on the high Q^2 side(hollowed square and hollow star) were extracted from the cross section instead of from the Rosenbluth separation. At such high Q^2 value, the cross section becomes too small to perform the Rosenbluth separation. Experiments at this range of high Q^2 assumed the relation $\mu_p G_E^p = G_M^p$ in extracting the magnetic form factor G_M^p. This relation has been proved to be not strictly accurate, which will be discussed later in this section. However, due to the G_M^p dominance in the cross section as discussed in 2.2.2, the error in assuming $\mu_p G_E^p = G_M^p$ is very small(less than 1 percent). The proton electric form factor G_E^p was measured with good accuracy in range of $Q^2 < 0.2$ GeV^2 with Rosenbluth separation. Again due to the G_M^p dominance in the cross section, it becomes difficult to extract the G_E^p with small uncertainty at high Q^2. In contrast, experiments at

JLab used the recoil polarization method to extract the form factor ratio G_E^p/G_M^p and achieved much better uncertainty than previous measurements. As can be seen in Figure 2-2, there exists apparent inconsistencies between the results of the two methods. While the result from the Rosenbluth separation method suggests that the form factor ratio $\mu_p G_E^p/G_M^p$ stays constant and have a consensus of 1, there is an obvious linear drop in the ratio obtained from the polarization method. This fast drop of the ratio $\mu_p G_E^p/G_M^p$ has brought many heated discussions in the structure of the nucleon as it contradicts the general belief of the constant behavior of the ratio from earlier experiments. It was the first experimental evidence that indicates the distribution of charge and magnetization are different, especially at short distances. The first two proton electric form factor experiments at JLab, GEp-I[36] and GEp-II[37], showed a drastic linear drop of the ratio $\mu_p G_E^p/G_M^p$. The ratio decreased as low as to $\sim$0.35 at $Q^2 = 5.6$ GeV^2 which indicated a zero crossing of the ratio $\mu_p G_E^p/G_M^p$ at $Q^2 \sim 10$ GeV^2. The third polarization transfer experiment GEp-III[38][39][40] showed a continued but slowed drop of the ratio, with its highest Q^2 data point measured to be 0.2 at $Q^2 = 8.5$ GeV^2.

2.3.2 Neutron Form Factors Data

Neutron form factors are less well known compared to proton form factors since there is no free neutron target. To measure the form factors of the neutron, complex light nuclei like deuteron or helium have to be used. For the neutron magnetic form factor G_M^n, one experimental technique is to do a coincidence measurement of the cross section of the $d(e, e'n)p$ reaction[41]. Since the neutron electric form factor G_E^n is close to zero at low Q^2, the G_M^n dominates in the cross section. This method removes the contribution of the proton but relies on good knowledge of neutron detection efficiency. Another common and effective technique is to extract G_M^n from the ratio of the $d(e, e'n)p$ and $d(e, e'p)n$ cross section. This method is used in many experiments[10][9][42][43][8] and is less sensitive to many nuclear effects and other experimental variables like target thickness, detection efficiency in the electron arm and exact knowledge of the beam intensity since many of these variables cancel in the

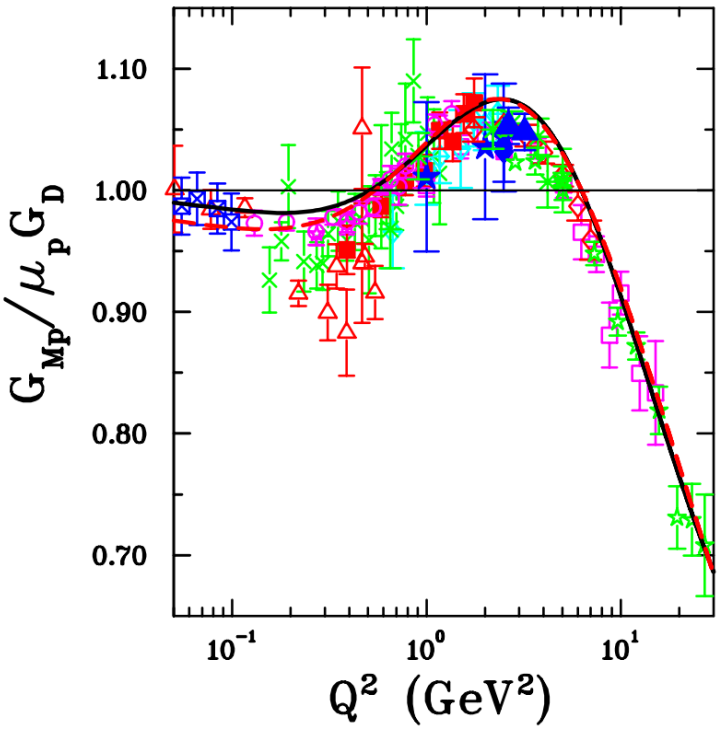

Figure 2-4: Proton magnetic form factor data obtained from cross section data using the Rosenbluth separation technique. Plot reproduced from [7]

ratio. However this method does need results from other experiments of the proton cross section to extract the neutron form factor G_M^n from the cross section ratio. Historical data on G_M^n is shown in Figure 2-5. As can be seen in the figure, the data with highest Q^2 is from an experiment at SLAC in the 1980s and shows a rapid drop of the neutron magnetic form factor. However, another experiment from Hall B at Jefferson Lab in 2009 measured the G_M^n with fine Q^2 bins and showed a flat behavior of the form factor. The neutron electric form factor G_E^n is the most difficult form factor to measure of the four nucleon form factors. In addition to the fact that there is no free neutron target, the neutron electric form factor G_E^n is zero at $Q^2 \sim 0$ because the neutrality of the neutron. One early technique is to do Rosenbluth separation in elastic electron deuteron scattering[44][45][46][47]. This method relies on theoretical calculation of the deuteron wave function and is model-dependent. Like the proton electric form factor G_E^p, the neutron electric form factor can also be measured with the polarization method. The recoil polarization technique and beam-target asym-

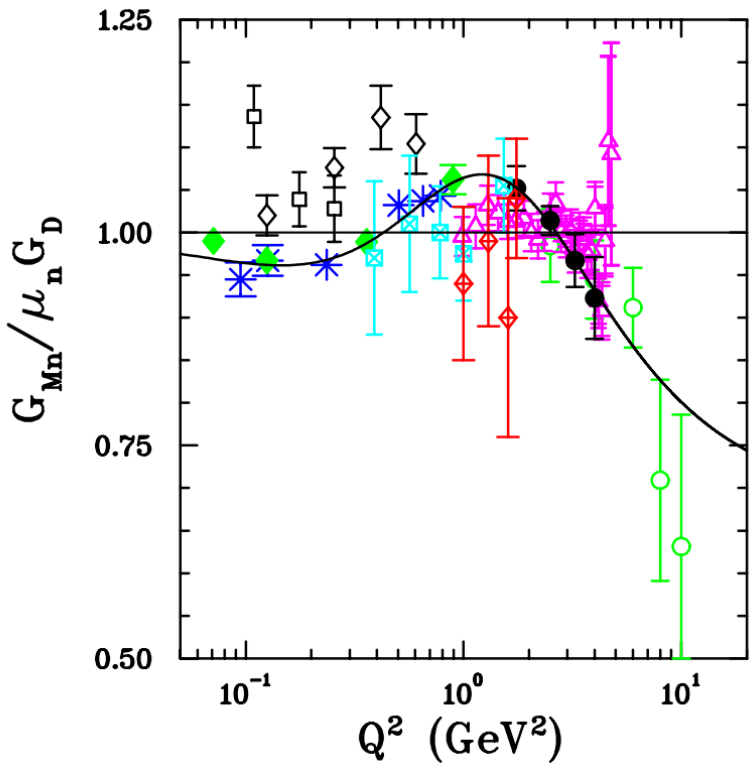

Figure 2-5: Neutron magnetic form factor data. The highest Q^2 data(green open circle) is from [8] at SLAC. The magenta open triangle are data with fine bins in Q^2 from experiment in Hall B at Jefferson Lab. Black open diamond[9] and blue star[10] are data from experiments using the ratio method. The solid line is a parameter fit of existing G_M^n data. Plot reproduced from [7]

metry technique have been used successfully with deuterium and helium targets to extract the ratio G_E^n/G_M^n. The GEn-I experiment in experimental Hall A at Jefferson Lab measured the nucleon form factor ratio G_E^n/G_M^n up to $Q^2 = 3.41$ GeV^2 using the beam-target asymmetry technique with a polarized electron beam and a polarized helium target[11]. This experiment more than doubled the available Q^2 range of previously existing data with good accuracy, providing a valuable benchmark for testing theories on nucleon structure. A collection of historical data on G_E^n/G_M^n using the polarization method can be found in Figure 2-6.

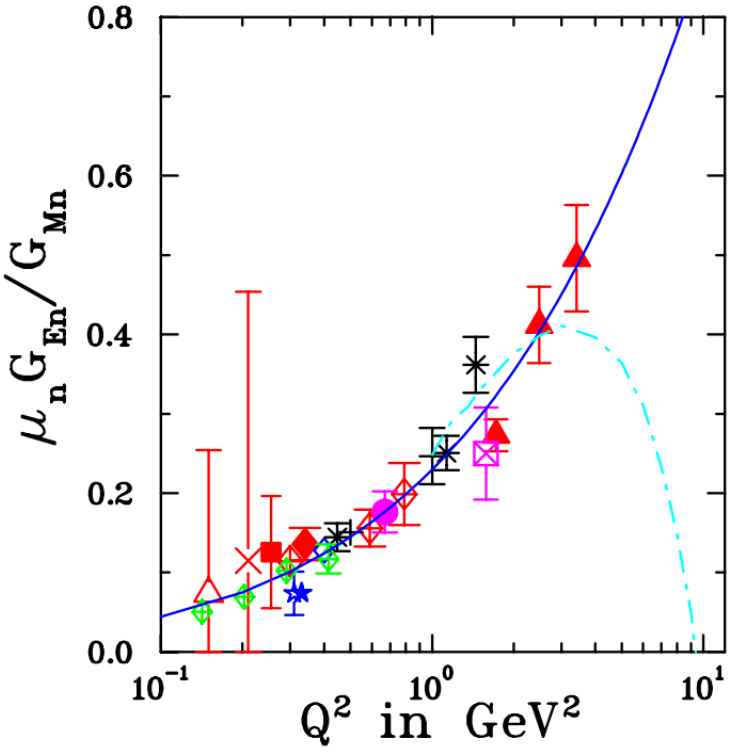

Figure 2-6: Neutron form factor ratio G_E^n/G_M^n using the polarization method. The highest Q^2 data(red solid triangle) is from GEn-I experiment at Jefferson Lab[11]. Other data using beam-target asymmetry techniques are: black asterisk[12], blue star[13], green diamond[14] and magenta circle[15]. Data using the recoil polarization method are: red open triangle[16], red diamond[17] and red solid diamond[18]. The solid line is a parameter fit of existing data. The cyan dashed line is a prediction of the ratio G_E^n/G_M^n by the DSE model[19]. Plot reproduced from [7].

2.4 Nucleon Structure Models

2.4.1 Dipole

One simple model for the nucleon form factors is the dipole model. In the low Q^2 range below 2 GeV^2, this model is rather successful in describing the proton electric form factor G_E^p, the proton magnetic form factor G_M^p and the neutron magnetic form factor G_M^n:

$$G_E^p = \frac{G_M^p}{\mu_p} = \frac{G_M^n}{\mu_n} = G_D \tag{2.25}$$

where $\mu_p = 2.79$ is the anomalous magnetic moment of the proton, $\mu_n = -1.91$ is the anomalous magnetic moment of the neutron and G_D is the dipole form factor defined as(when Q is in GeV^2):

$$G_D = \left(1 + \frac{Q^2}{0.71}\right) \tag{2.26}$$

In the low Q^2 limit where the form factors G_E and G_M can be regarded as the Fourier transform of the nucleon's charge and magnetization distribution, the dipole model corresponds to a spherically symmetric and radially exponentially decaying distribution:

$$\rho = \frac{\lambda^3}{8\pi} e^{-\lambda r} \tag{2.27}$$

The mean charge radius of the proton can be estimated to be 0.8 fm using 2.3, which is very close to the most up-to-date measurement which gives 0.83 fm.

Although the dipole model is very successful in the low Q^2 range, it struggles to accurately describe the proton electric form factor in the range of $Q^2 > 2$ GeV^2 . Three consecutive measurements of the proton electric form factor using the recoil polarization technique has shown that the proton form factor ratio G_E^p/G_M^p decreases almost linearly with Q^2[36][37][40], unlike what is predicted by the dipole model($G_E^p/G_M^p = 1/\mu_p$).

2.4.2 Galster

The Galster parameterization was given by Galster in 1971 to describe the neutron electric form factor G_E^n[46]:

$$G_E^n = -\frac{\mu_n \tau}{1 + 5.6\tau} G_D \tag{2.28}$$

where $\tau = \frac{Q^2}{4m^2}$ and $\mu_n = -1.91$ is the anomalous magnetic momentum of the neutron. The Galster fit has been rather successful in describing the neutron electric form factor G_E^n for decades. The mean charge radius of the neutron can be estimated to be -0.11 fm using 2.3, which indicates that the neutron has a positively charged core in the center although being neutral overall.

2.4.3 Perturbative QCD

QCD governs the strong interaction between the quarks and gluons in the nucleon. At low Q^2, the coupling constant $\alpha_s > 1$, makes the perturbative approach used for QED not applicable. However, at higher energies, α_s decreases. When α_s is small enough, perturbative QCD(pQCD) can be used to study the interactions inside the nucleon. Earlier calculation showed that there is a scaling behavior in the ratio of the Dirac and Pauli form factor of: Q^2F_2/F_1 *constant* as $Q^2 \to \infty$. However, previous measurements[36][37][40] on proton electric form factors at Jefferson Lab using the recoil polarization method has shown a clear deviation from this behavior. Later calculation[48] which takes the quark orbital angular momentum into consideration showed that at large Q^2, the scaling is:

$$\frac{Q^2}{log^2(\frac{Q^2}{\Lambda^2})}\frac{F_2}{F_1} = constant \tag{2.29}$$

where λ is a scale parameter. Previous G_E^p data at Jefferson Lab showed a good matching with this scaling behavior. The new GEp-V experiment will provide valuable data points at even higher Q^2 to check whether this scaling continues.

2.4.4 Constituent quark model

The Constituent quark model(CQM) states that the nucleon is the ground state of three quarks confined in a potential. The proton is composed of two up quarks and one down quark. And the neutron is composed of two down quarks and one up quark. The early non-relativistic versions of CQM had very successful predictions on nucleons' static properties, such as the masses, magnetic moments, and transition amplitudes[49][50]. However, non-relativistic CQMs have too small of predictions on form factors at high Q^2. Since the quarks within the nucleon contributes to only about 1% of the nucleon mass, relativistic treatment is essential. Prediction on the proton form factor G_E^p/G_M^p from relativistic versions of CQM[51][52][53] had rough agreement with experimental data using the recoil polarization method at Jefferson

Lab.

2.5 Form factors data in the near future

Thanks to an upgrade of the beam energy at Jefferson Lab, several experiments investigating the structure of the nucleon will bring us into further unexplored regions of four-momentum transfer squared(Q^2). In experimental hall A, a new Super BigBite Spectrometer(SBS) is built and ready to run for measuring three of the four nucleon form factors. The four form factor experiments of the SBS program are: GEp-V, GEn-II, GEn-RP, and the GMn experiment. The GEp-V experiment will measure G_E^p/G_M^p up to $Q^2 = 12$ GeV^2. The GEn-II experiment will measure G_E^n/G_M^n up to $Q^2 = 10$ GeV^2. The GEn-RP experiment will measure the G_E^n/G_M^n at $Q^2 = 4.5$ GeV^2. The GMn experiment will measure G_M^n up to $Q^2 = 14$ GeV^2. In experimental hall B, the new CLAS12 spectrometer will measure G_M^n with Q^2 up to 14 GeV^2. A plot of the nucleon form factors of the coming experiments at Jefferson Lab is shown in Figure 2-7. Together they are bring new insights in our understanding of the nucleon structure.

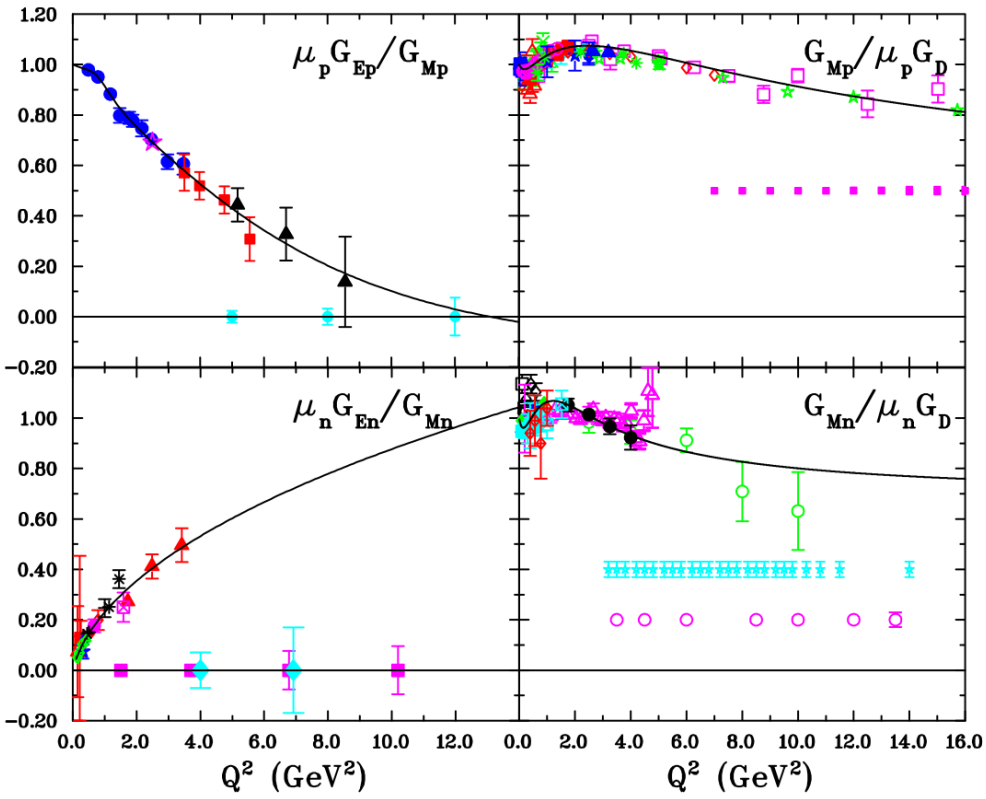

Figure 2-7: Coming nucleon form factor experiments at Jefferson Lab and their projected error bars. The top left plot is for the proton electric form factor G_E^p. The data points and the error bars are shown as cyan circles. The top right plot is for the proton magnetic form factor G_M^p. The GMp experiment run in experimental hall A at Jefferson Lab shown as magenta squares is under analysis. The bottom left plot is for the neutron electric form factor G_E^n. The GEn-II experiment in experimental hall A is shown as magenta squares and the experiment E12-11-009 at experimental hall C is shown as cyan diamonds. The bottom right plot is for the neutron magnetic form factor G_M^n. The GMn experiment is shown as magenta circles and the experiment in hall B is shown as cyan stars. Plot reproduced from [7].

Chapter 3

Description of the SBS Experiments

The SuperBigBite project consists of four ground-breaking measurements of the nucleon's elastic form factors. It will start running in 2020 and will continue for two years. The experiments in this program are:

- GEp-V: Measurement of the Proton Form Factor Ratio, G_{Ep}/G_{Mp} up to 12 GeV^2 Using Recoil Polarization Method (E12-07-109).

- GEn-II: Measurement of the Neutron Electromagnetic Form Factor Ratio G_{En}/G_{Mn} at High Q^2(at Q^2= 5.0, 6.8 and 10.2 GeV^2) (E12-09-016).

- GEn-RP: Measurement of the Neutron Electromagnetic Form Factor Ratio G_{En}/G_{Mn} at $Q^2 = 4.5GeV/c^2$ using recoil polarisation technique.

- GMn: Precision Measurement of the Neutron Magnetic Form Factor up to Q^2=13.5GeV^2 (E12-09-016).

In this chapter we will first introduce the common beam facility continuous electron beam accelerator facility(CEBAF) at Jefferson Lab and then describe the experimental technique and apparatus of these experiments.

3.1 CEBAF

The Continuous Electron Beam Accelerator Facility (CEBAF) at Jefferson Laboratory is a recirculating LINear Accelerator (LINAC). It consists of two superconducting LINACs, two recirculating arcs, a polarized electron gun and extraction elements. The original design [54] of CEBAF is shown in Figure 3-1 . CEBAF uses a 1497 MHz diode laser on a strained GaAs cathode to produce polarized electrons. The polarized electrons are then injected into the main accelerator. A Wien filter can be utilized to orient the polarization of the electrons. After the electron enters the accelerator, it is then accelerated by the north LINAC before guided into the south LINAC by the recirculating arc. Each LINAC consists of 20 cryomodules, each providing a boost of 25 MeV to the electrons. Within each cryomodule there are 8 superconducting RF cavities. For every loop an electron travels in the accelerator, it gained an energy of up to 1 GeV, depending on the tune. At the end of the south LINAC, the electrons are giuded by the extraction elements into one of the three experimental halls. During its pre-upgrade era, CEBAF provided continuous electron beams with polarizations up to 85% at energies up to 6 GeV and currents up to 180 μA to many experiments([55], [38],[11], etc) which led to many ground breaking new discoveries of nucleon structure at Jefferson Lab.

To further increase the range of physics programs and enable new insights into the nucleon structure, CEBAF was upgraded with 5 new cryomodules in each of the two LINAC as shown in Figure 3-2 [56]. Together with improved strength of the RF cavities which increased the boost per cryomodule to 100 MeV (compared to 20 MeV before the upgrade), CEBAF is now capable of delivering beam energies of 2.2 GeV, 4.4 GeV, 6.6 GeV, 8.8 GeV and 11 GeV to Experimental Halls A, B and C. Experimental Hall D was added on the opposite side of the accelerator from the three original halls as shown in the Figure 3-2. Electrons entering Hall D receive an extra boost from the North LINAC, which makes the energy cap of CEBAF to be 12 GeV.

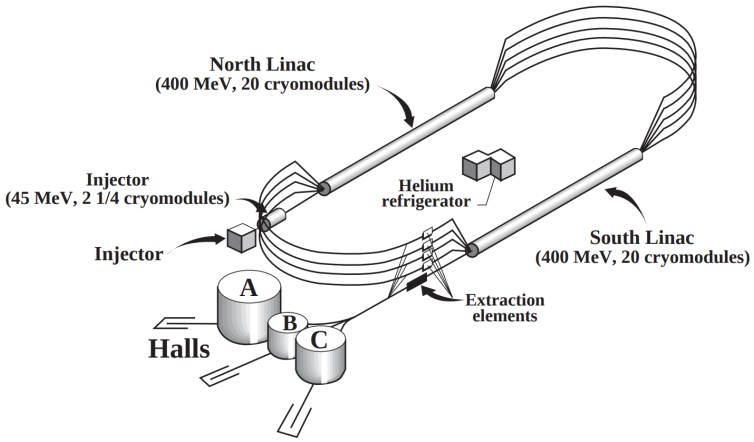

Figure 3-1: The original design of CEBAF: polarized electrons are generated from the polarized gun before going clockwise into the acceleration loop. The two LINACs accelerate the electrons, and the magnets in the circulating arcs guide the electron beam from one LINAC to the other one. The electrons can circulate up to 5 times before being extracted into of the three original experimental halls by the extraction elements.

3.2 GEp-V

The GEp-V experiment was the original motivation behind building the Super-BigBite spectrometer. It is the successor of the previous three successful GEp experiments [36][37][40] which showed that the decrease of proton form factors ratio with increasing momentum transfer Q^2. It aims to measure the proton form factor ratio up to a Q^2 value 12 GeV^2, a 50% increase over the available Q^2 range, using the recoil polarization method. This measurement of G_{Ep}/G_{Mp} at high momentum transfer will provide new data to test many phenomenological models and check the indication of the slowing down of the decrease of the proton form factor ratio from the GEp-III experiment[38][39][40]. GEp-V will use an electron beam with 85% polarization, accelerated up to 11 GeV in the CEBAF accelerator. The Electrons collide with a 40 cm liquid hydrogen target. The recoiling proton from the elastic scattering process will be measured by the SBS spectrometer. After being deflected by a single dipole magnet, the recoil proton will be measured by three sets of GEM trackers separated by two CH^2 analyzers before going into a hadron calorimeter. The scattered electron will be detected in a highly segmented electromagnetic calorimeter named BigCal,

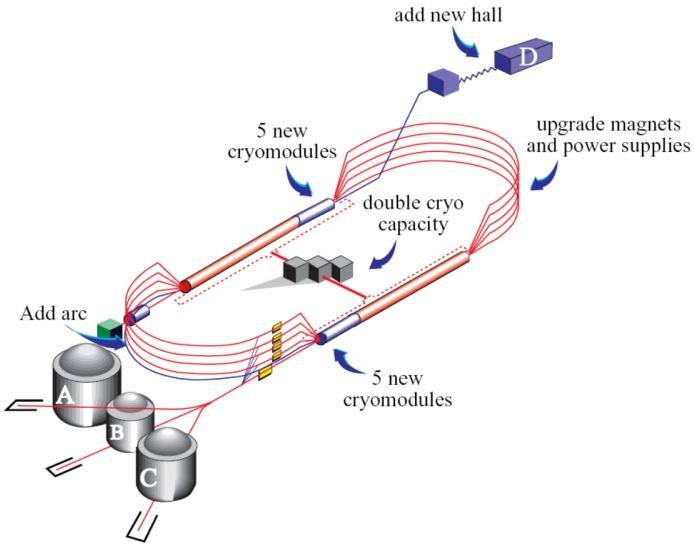

Figure 3-2: The 12 GeV upgrade of CEBAF: five additional cryomodules were added to the north and south LINAC, which made the boost of electron energy after one cryomodule to be 1 GeV. Magnets in the recirculating arcs were upgraded to accommodate the new beam energies. Cryo capacity of the helium refrigerator was also doubled for the additional cooling power needed.

which provides a highly effective way of suppressing inelastic backgrounds.

3.2.1 The Experimental Principle

The GEp-V experiment uses the recoil polarization method. In Chapter 2, we reached the relationship between the ratio of the two polarization components and the ratio of the Sachs form factors:

$$\frac{G_E}{G_M} = -\frac{P_t}{P_l}\frac{E_e + E'_e}{2m_p} tan\frac{\theta_e}{2} \tag{3.1}$$

where P_t and P_l are respectively the polarization components of the recoil proton perpendicular and parallel to the proton momentum in the scattering plane. In GEp-V, the ratio of the polarization transfer components, $\frac{P_t}{P_l}$ is measured by the focal plane polarimeter which consists of two CH_2 analyzers and two sets of GEM trackers. The ratio of the two polarization components results in a certain distribution of the angular deflection of the proton when it interacts, through the nuclear interaction, with the

E (GeV)	Q^2 (GeV)	θ_E (deg)	P_e (GeV)	Θ_p (deg)	P_p (GeV)	Days	$\delta\mu G_E/G_M$
6.6	5.0	25.3	3.94	29.0	3.48	1	0.023
8.8	8.0	25.9	4.54	22.8	5.12	10	0.032
11.0	12.0	28.2	4.60	17.4	7.27	30	0.074

Table 3.1: Kinematics and expected accuracy of GEp-V experiment

atomic nuclei in the CH_2 analyzer as it passes through the analyser. The relationship can be written as[32]:

$$f(p,\theta,\phi) = \frac{\epsilon(p,\theta)}{2\pi}(1 + A_y(p,\theta)S_y cos\phi - A_y(p,\theta)S_x sin\phi) \tag{3.2}$$

where $f(p,\theta,\phi)$ describes the distribution density, $\epsilon(p,\theta)$ is the efficiency of polarimeter, S_x and S_y are the spin components of the proton and A is the analyzing power which measures the relation between polarization of the proton and the final asymmetry in the azimuthal distribution.

3.2.2 The Experimental Setup

The GEp-V experiment is located in experimental hall A at Jefferson Lab. An electron beam at 75 μA with 85% polarization is generated from the CEBAF accelerator. The beam polarization is kept at the maximum to maximize the asymmetries measured in the focal plane polarimeter. The main target is 40 cm liquid hydrogen for the measurement of the asymmetries. Additionally, a carbon target consisting of thin carbon foils will be used for optical studies. The detector set consists of two major parts, the electron arm and proton arm. The setup of the experiment is shown in Figure 3-3. The kinematics of the experiment is shown in Table 3.1

Focal Plane Polarimeter

The proton polarimeter aims to measure the polarization of the recoil proton by measuring the azimuthal asymmetries of the scattered protons that passed through the analyzer. It consists of two 40 cm analyzer blocks and three sets of GEM detectors.

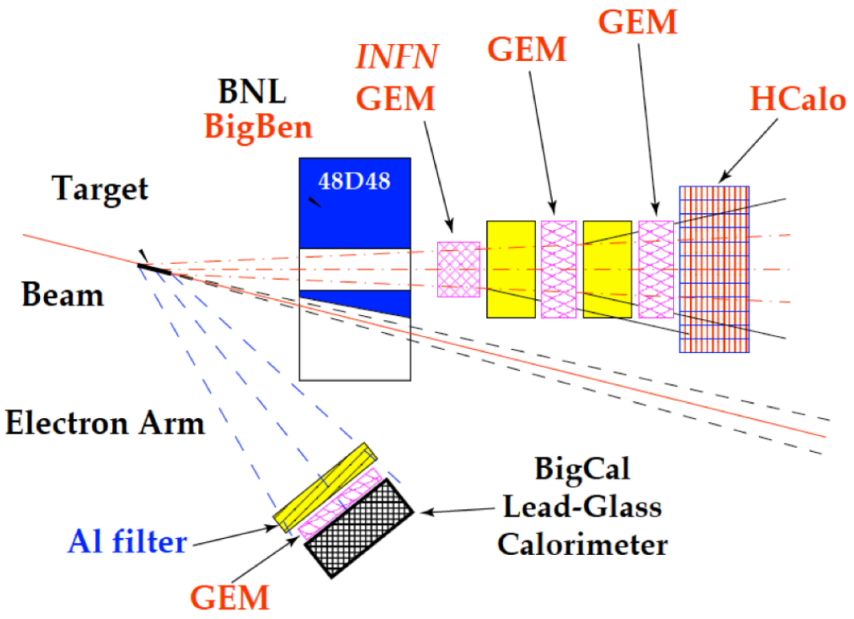

Figure 3-3: The experimental setup of GEp-V experiment.

CH_2 is selected as the material for the analyzer blocks to maximize the analyzing power while keeping the construction and operating costs at a reasonable level. Compared to liquid H_2 which has the ideal analyzing power, CH_2 is much more cost-effective and more importantly much safer to operate. Compared to another possible material candidate Carbon, the calibration measurement at the Joint Institute for Nuclear Research(JINR) showed that CH_2 offers 12% higher analyzing power[57]. The thickness of the analyzer is determined to maximize the efficiency of the polarimeter. Theoretically the thicker the analyzer is the larger the fraction of protons scattered by the material is. However, increasing the thickness also increases the effect of multiple scattering which can potentially decrease the accuracy of the polarimeter. The measurement at JINR also showed that the integral efficiency does not increase with the thickness of the material after one nuclear collision length[57]. Each CH_2 analyzer block is sandwiched between two sets of GEM trackers, which makes one proton polarimeter. The two analyzer blocks are placed one after the other along the track of the scattered protons and is used as two independent polarimeters to increase efficiency.

The first GEM tracker(referred as the front trackers) in front of both analyzers

consists of 6 layers of 40 cm x 150cm GEM chambers. Each of these chambers consists of three 40 cm x 50 cm GEM modules which are constructed at Istituto Nazionale di Fisica Nucleare(INFN). The other two GEM trackers(referred as the back trackers) consist of 5 layers of 60 cm x 50 cm GEM chambers. Each of the chambers consist of four 60 cm x 50 cm GEM modules which are constructed at the University of Virginia(UVa). These GEM detectors offer high rate capability up to 100 MHz/cm^2 and good spatial resolution of 70 μm. More details on GEM detector will be discussed in Chapter 4.

Hadron Calorimeter

The hadron calorimeter(HCAL) is used to measure the energy of the recoil proton. It consists of 11 x 22 modules each with size of 15 cm x 15 cm x 100 cm. Within each module there are forty 20 mm iron plates that pair up with a scintillator plate, wave-length shifter, a photomultiplier tube(PMT) and a PMT base. The design of a hadron calorimeter module is shown in figure 3-4[58]. The Hadron calorimeter was built at JINR and successfully used in the NA58 COMPASS experiment at CERN. The energy resolution for hadrons and spatial resolutions for the two directions are[58]:

$$\frac{\sigma_\pi(E)}{E[GeV]} = \frac{59.4 \pm 2.9}{\sqrt{E}} \oplus (7.6 \pm 0,4)\% \tag{3.3}$$

$$\sigma_{x,y} = 15mm \tag{3.4}$$

A threshold on the energy in the HCAL can be set to reduce the trigger rate caused by the open configuration of the SBS spectrometer. Unwanted pions can also be eliminated by using the HCAL. Additionally, because of the good spatial resolution in the HCAL, the track reconstruction(which suffers from the large random background) can greatly benefit from a cut based on projected position on the HCAL plane.

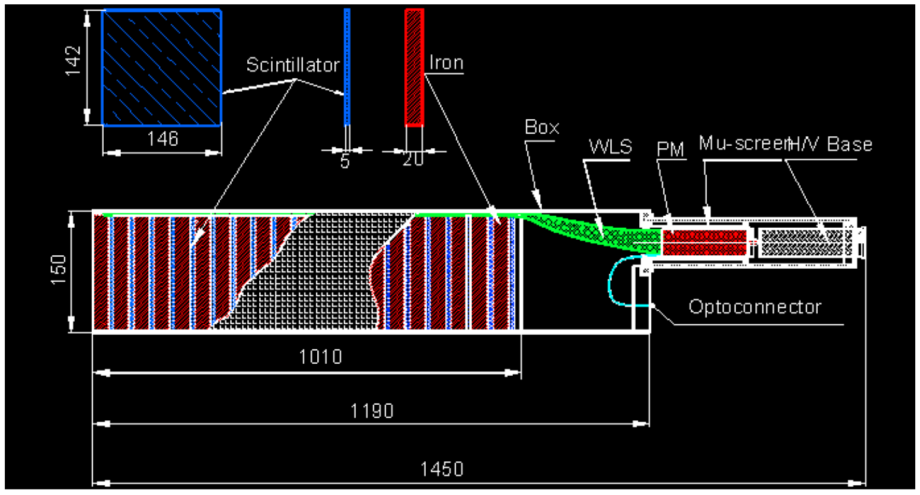

Figure 3-4: The design of the hadron calorimeter module in the GEP-V experiment.

Electromagnetic calorimeter

The scattered electron is detected in the 1744 channel lead-glass electromagnetic calorimeter BigCal(Figure 3-5). The BigCal consists of two groups of lead-glass blocks. A total of 32 x 32 glass blocks constructed at the Institute for High Energy Physics(IHEP), are each 38 x 38 x 450 mm^3, form the bottom part of the calorimeter. The other group of 30 x 24 blocks with size of 40 x 40 x 400 mm^3, which was used in the Real Compton Scattering experiment(RCS) in experimental hall A at JLab, form the top part of the calorimeter. A schematic of the BigCal is shown in Figure 3-6. The BigCal provides millimeter level coordinate resolution. Combined with information of the interaction vertex which is extracted from proton arm, the coordinate position of the electron on BigCal can be transformed into scattering angle of the scattered electron for elastic events. Given the coordinate resolution and the distance of the BigCal from the target, the angular resolution is around 2 $mrad$. The energy resolution is expected to be around $\frac{5\%}{sqrt(E)}$(where E is in GeV) [59].

The main purpose of the BigCal is to detect the scattered electron in coincidence with the recoiled proton. The BigCal is thick enough to fully stop electrons up to 10 GeV. Combined with the information of the recoiled proton collected in the proton arm, the scattering angle and energy of the electron can be used to identify elastic events from inelastic backgrounds. The BigCal covers an area of 120 x 220 cm^2, which

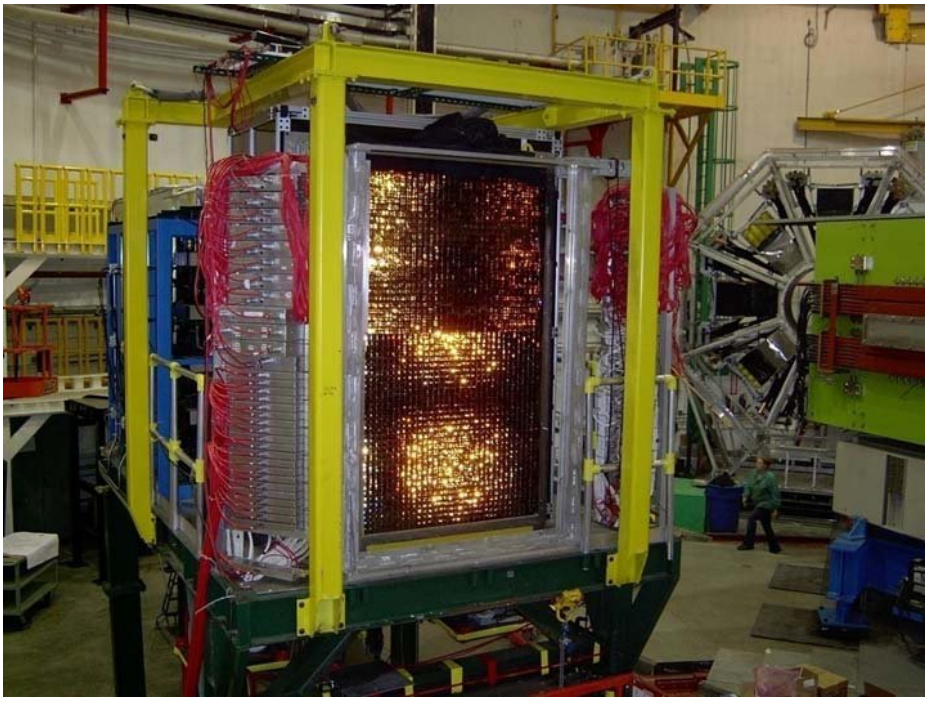

Figure 3-5: Photograph of the BigCal at Jefferson Lab[20].

matches the acceptance of the proton in the SBS spectrometer. For elastic events, the energy of the scattered electron can be extracted from the scattering angle of the electron and vice versa. Since the resolution of energy extracted from the scattering angle is much better than the energy resolution of the BigCal itself, the final energy of the electron will be determined by its scattering angle.

3.3 GMn

The GMn experiment is scheduled to take place in experimental hall A at Jefferson Lab in 2020. The goal of the experiment is to measure the neutron magnetic form factor at Q^2 = 3.5, 4.5, 6.5, 8.5, 10.0, 12.0, 13.5 GeV^2 using the "ratio method" that is discussed in detail in the next section. Electrons from the CEBAF accelerator with energy up to 11 GeV will collide with a liquid deuteron target. Both scattered protons and neutrons will be detected by the BigHAND detector after passing through the field of a dipole magnet, BigBen, which is used to deflect the protons away from the neutrons. The momentum and angle of the scattered electrons will be measured

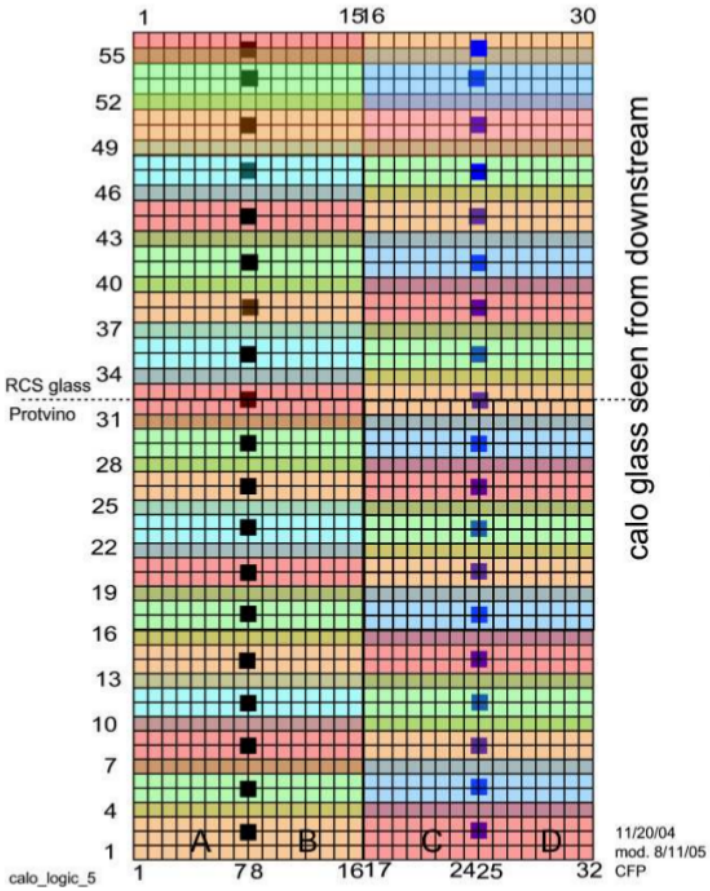

Figure 3-6: The arrangement of the 1744 lead-glass blocks of BigCal. Different colors identify the different groups of trigger channels.

by the upgraded BigBite spectrometer. The kinematics of the GMn experiment are shown in Table 3.2

3.3.1 The Experimental Principle

The GMn experiment measures the G_{Mn} using the "ratio method" by measuring both recoiled protons and recoiled neutrons from quasi-elastic electron scattering off the deuteron. The measured ratio of quasi-elastic cross sections:

$$R'' = \frac{\frac{d\sigma}{d\Omega}|_{d(e,e'n)}}{\frac{d\sigma}{d\Omega}|_{d(e,e'p)}} \tag{3.5}$$

E (GeV)	Q^2 (GeV)	θ_e (deg)	P_e (GeV)	Θ_n (deg)	P_n (GeV)
4.4	3.5	32.5	2.5	31.1	2.6
4.4	4.5	41.9	2.0	24.7	3.2
4.4	5.7	58.4	1.2	17.5	4.0
6.6	8.1	43.0	2.1	17.5	5.4
8.8	10.2	34.0	3.5	17.5	6.2
8.8	12.0	44.2	2.4	13.3	7.3
11.0	13.5	30.0	1.6	14.9	8.1

Table 3.2: Kinematics of GMn experiment

can be related to the ratio of elastic cross sections after taking the nuclear effect into account:

$$R' = \frac{\frac{d\sigma}{d\Omega}|_{n(e,e')}}{\frac{d\sigma}{d\Omega}|_{p(e,e')}} = \frac{R''}{1+\epsilon_{nuc}} \tag{3.6}$$

where ϵ_{nuc} is the nuclear correction that can be accurately calculated. The difference between the cross section for quasi-elastic scattering and the cross section for elastic scattering from free nucleon is substantial due to final-state interactions and other nuclear effects. However, in the "ratio method", the correction ϵ_{nuc} to the ratio of the cross sections is very small because the corrections to the cross section of the proton and that of the neutron is almost identical and cancel. Arenhövel calculated the correction factor and found the correction to be very small, which is shown in Figure 3-7.

Based on calculations in Chapter 2, the differential cross section for electron scattering off a spin$\frac{1}{2}$ target in one-photon approximation can be written as:

$$\frac{d\sigma}{d\Omega} = \eta \frac{\sigma_{Mott}}{1+\tau}\left((G_E)^2 + \frac{\tau}{\epsilon}(G_M)^2\right) \tag{3.7}$$

where $\sigma_{Mott} = \frac{\alpha^2}{4E_e^2 \sin^4\frac{\theta_e}{2}} \frac{E'_e}{E_e} \cos^2\frac{\theta_e}{2}$ is the Mott cross section, θ_e is the scattering angle, E'_e is the energy of the scattered electron, E_e is the initial energy of the electron, α is the electromagnetic coupling constant, $\tau = \frac{Q^2}{4M^2}$, Q^2 is the square of the four-momentum transfer, M is the mass of the target, $\epsilon = \left[1 + 2(1+\tau)\tan^2\frac{\theta_e}{2}\right]^{-1}$, and G_E and G_M are the Sachs Electric and Magnetic form factors.

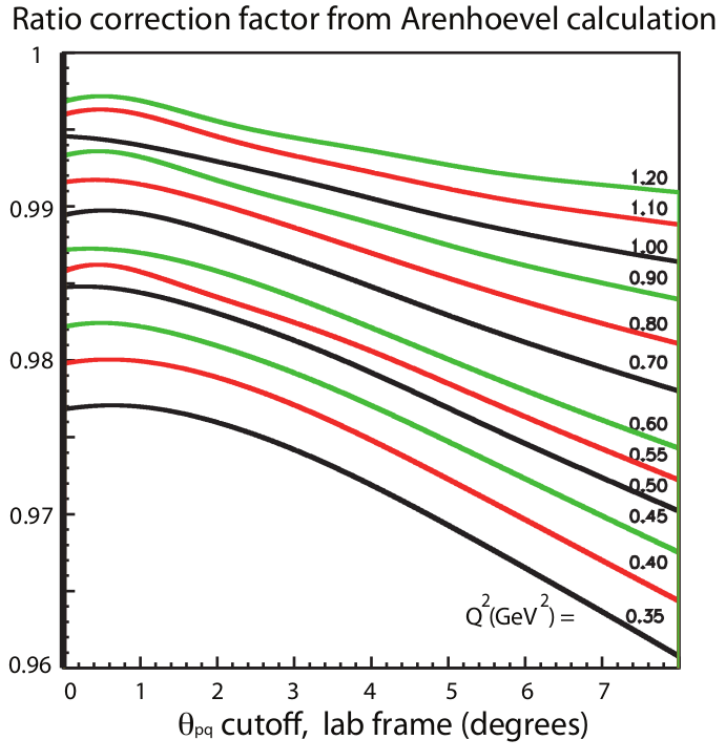

Figure 3-7: predictions of nuclear corrections as a function of the maximum θ_{pq} allowed in acceptance. The correction decreases with Q^2 and is small in case of a right cut on θ_{pq}. Plot reproduced from [21]

Thus, the ratio of neutron and proton elastic cross sections can be written as:

$$R' = \frac{\eta \frac{\sigma_{Mott}}{1+\tau}\left((G_E^n)^2 + \frac{\tau}{\epsilon}(G_M^n)^2\right)}{\frac{d\sigma}{d\Omega}|_{p(e,e')}} \tag{3.8}$$

Then the ratio of interest is:

$$R \equiv \frac{\eta \frac{\sigma_{Mott}}{1+\tau}\frac{\tau}{\epsilon}(G_M^n)^2}{\frac{d\sigma}{d\Omega}|_{p(e,e')}} = R' - r \tag{3.9}$$

with

$$r = \frac{\eta \frac{\sigma_{Mott}}{1+\tau}(G_E^n)^2}{\frac{d\sigma}{d\Omega}|_{p(e,e')}} \tag{3.10}$$

Calculations have shown that if the neutron electric form factor, G_E^n, follows the Galster parameterization, the term to be subtracted from R', r, will be very small(less than 1%) compared to R' and can be neglected compared to other systematic errors.

Results from the other SBS experiment GEN(2) will also be used to confirm this calculation and make corrections if needed.Thus the neutron magnetic form factor G_M^n can be determined from the ratio of interest R which can be related to the direct measurement of this experiment R'' by correcting the small nuclear correction ϵ_{nuc} as discussed above.

3.3.2 Experimental Setup

The GMn experiment will take place in experimental hall A at Jefferson Lab. The experiment uses an unpolarized electron beam with energy up to 11 GeV on an unpolarized deuterium target. Two major detector package will be used in the experiment: the BigHAND nucleon detector as the hadron arm to detect recoiled protons and neutrons and the upgraded BigBite spectrometer to detect the scattered electrons. The layout of the experiment apparatus is shown in the Figure 3-8.

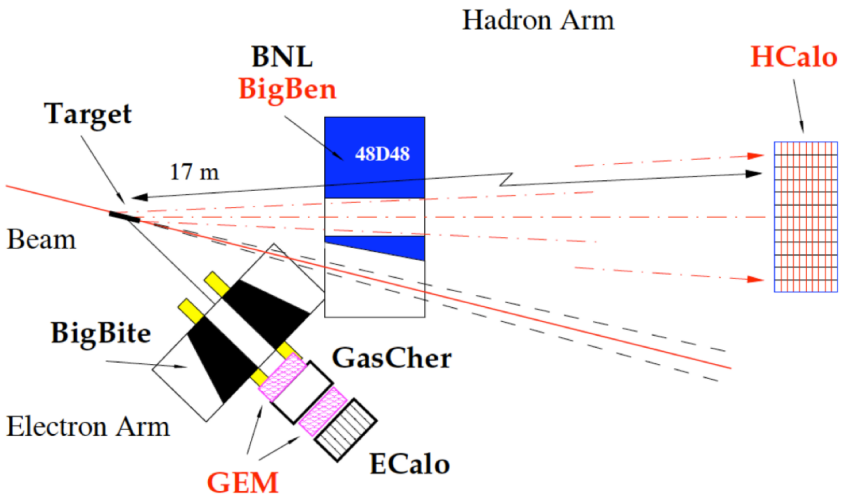

Figure 3-8: The experimental setup of GMn experiment

BigBite Spectrometer

BigBite is a medium resolution spectrometer with a moderately large acceptance which is used to measure the direction and magnitude of the momentum of the scattered electrons in this experiment. BigBite consists of a dipole magnet for deflecting

charged particles for momentum analysis, followed by a detector stack for tracking and particle identification. BigBite[60] was initially constructed for an experiment at National Institute for Subatomic Physics(Nikhef) and was moved to Jefferson Lab experimental Hall A. There, the BigBite detector package was replaced with a newly constructed detector package consisting of a Cerenkov detector, and a lead-glass calorimeter and three high-resolution, high-rate Multi-Wire Drift Chambers(MWDC). This set of WMDCs was developed and fabricated by the UVa group. This newly upgraded BigBite was successfully used for a series of 6-Gev experiments at Jefferson Lab[11][61][62][63]. This series included the E02-013 experiment: Measurement of the Neutron Electric Form Factor GEN at High Q2[11] which more than doubled the high-Q^2 reach of the neutron elastic form factor. Furthermore, the success of this experiment demonstrated the potential of the idea of using a medium to large acceptance, open configuration, simple dipole spectrometer to increase the figure of merit of high Q^2 nucleon form factor experiments. This directly led to the SBS project: BigBite spectrometer forms the electron spectrometer for several approved SBS project experiment including GEn-II, GEn-RP and GMn. In order to meet the high rate conditions expected in these high-Q^2 experiments BigBite was upgraded yet again with a new detector package consisting of 5 layers of GEM detectors for track reconstruction, a high-granularity gas Cerenkov counter[64] and a lead-glass electromagnetic calorimeter[65] for providing trigger and random background rejection, as shown in Figure 3-9 The BigBite spectrometer will be positioned close to the target with its entrance aperture of the dipole 1.55 m away from the target. The acceptance will be about 50 msr with luminosity roughly xxxx. To address the challenge of efficient and accurate track reconstructing with such high luminosity and large acceptance, the previous multi-wire drift chambers will be replaced with 5 layers of SBS GEM detectors newly constructed by our UVa GEM group. The layout and size of the SBS GEM detectors is shown in Figure 3-10. These GEM detectors provides a spatial resolution less than 100 μm and stable operation in this highly demanding experimental condition. Details about the GEM detectors will be discussed in the next chapter. The electromagnetic calorimeter consists two parts, shower and

preshower, and has a spatial resolution about 5 cm and energy resolution of $5\%/\sqrt{E}$. The reconstructed position on the calorimeter will provide a rough position cut for rejecting random background GEM hits due to large amounts of soft photons. In addition, by combining the information in shower and preshower, it will also help in particle identification.

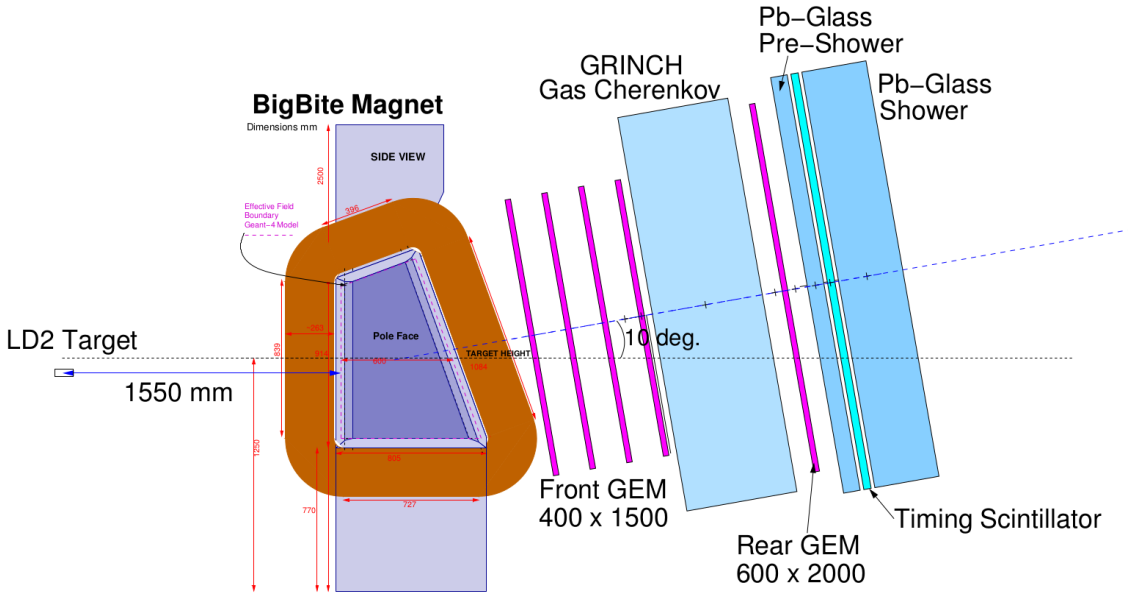

Figure 3-9: Side view of BigBite spectrometer

BigBen magnet

The BigBen magnet consists of a large dipole magnet with opening of 46 x 25 cm and depth of 48 cm as shown in Figure 3-11. The magnet was known as 48D48 at Brookhaven and is modified at JLab with new coils. It will be located 1.6 m away from the target chamber. A slot is made in the magnet to let beam line pass through as shown in Figure 3-12. With a field integral about 2 T·m, the BigBen magnet is able to deflect the high energy recoiled protons upwards and away from the neutron by 1 m on the neutron detector plane. This is the main method to differentiate neutron from protons. Meanwhile charged particles with energy below 1 GeV will be swept completely away from the neutron detector, which decreases the background greatly.

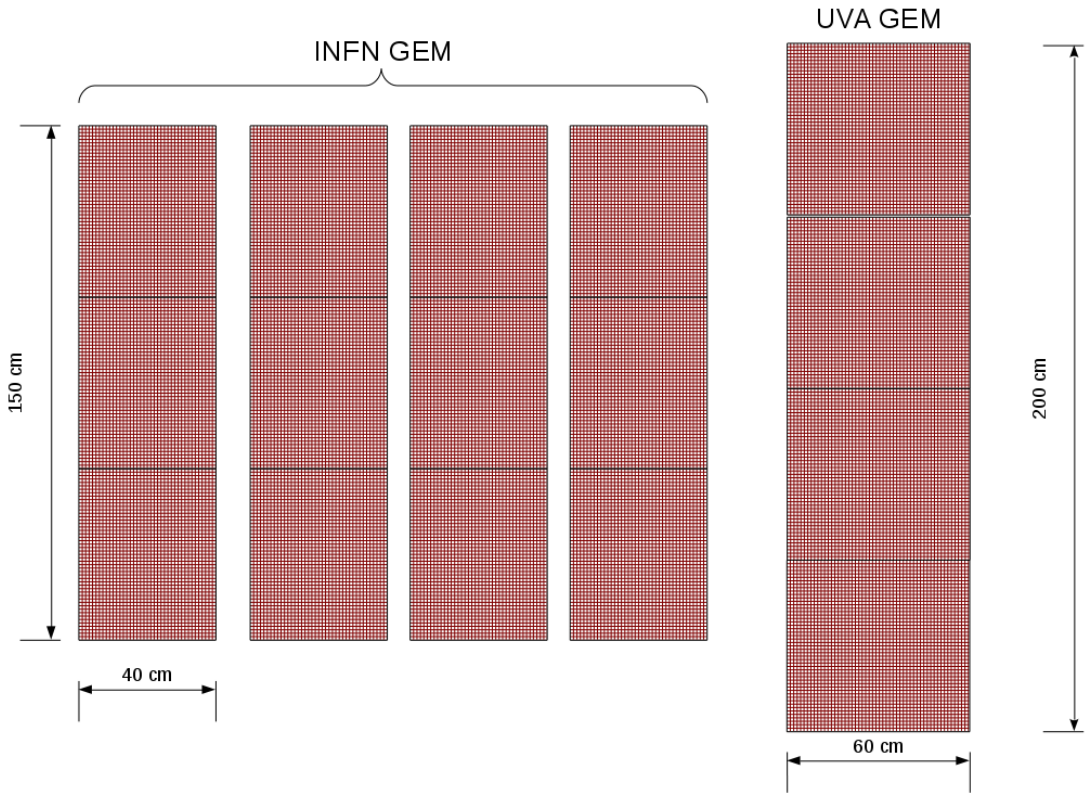

Figure 3-10: GEM detector layout in BigBite spectrometer. The first 4 GEM layers are constructed at INFN. Each of these layer consists of 3 GEM modules which has an active area of 40 x 50 cm^2. The last layer is built at UVa and consists 4 GEM modules each with an active area of 50 x 60 cm^2

BigHAND nucleon detector

The BigHAND is a large wall of scintillator detectors with iron converters to initiate hadronic showers which increase the possibility of detecting nucleons, as shown in Figure 3-13. The BigHAND also provides certain level of identification of protons and neutrons, time of flight, and the position of the nucleon hit. From these the magnitude and direction of the nucleon can be determined. The BigHAND locates at 17 m away from the target. The spatial resolution of the detector is vertically 4 cm and horizontally 7 cm. This resolution will provide essential cuts on the θ_{pq}, the angle between the recoiled nucleon and the momentum transferred from the electron. The time of flight resolution is about 400 ps and will provide some level of background rejection. A 'veto' layer will be instrumented in front of the iron converters as one way

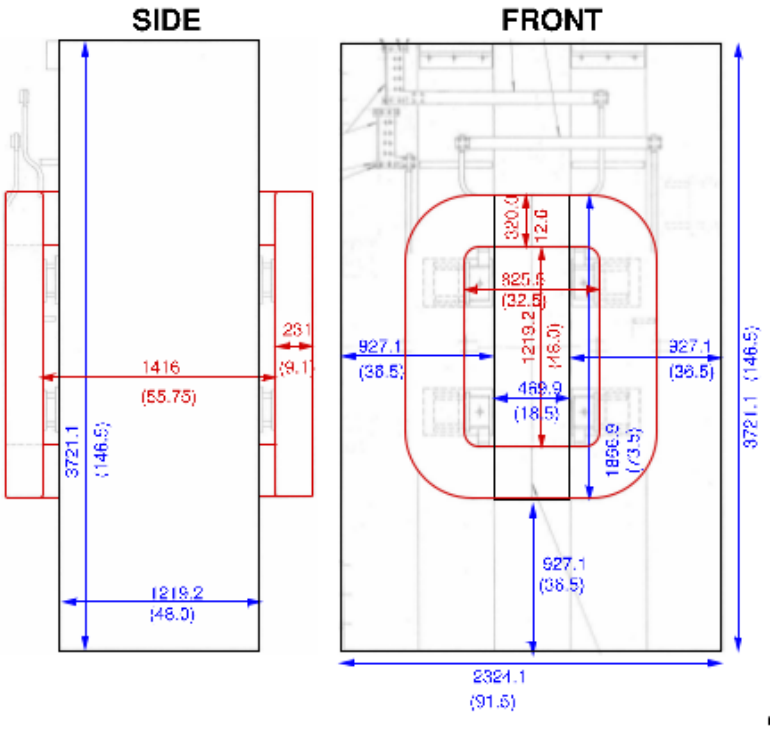

Figure 3-11: Schematic of BigBen magnet

of proton/neutron identification in addition to the method discussed in the BigBen magnet section above.

3.4 GEn-II

The GEM-II experiment aims to measure the electromagnetic form factor ratio of the neutron, G_E^n/G_M^n, at high four-momentum transfer values of $Q^2 = 5.0$, 6.8 and 10.2 GeV^2 using the so called double polarization method. The experiment uses polarized electron beam and a polarized ^3He target. In quasi-elastic kinematics, transverse asymmetry of the cross section arise for different orientation of the polarization of the electron and target. The asymmetry is measured by alternating the beam helicity. The electromagnetic form factor ratio G_E^n/G_M^n can be related to and extracted from this transverse asymmetry $A_\perp$. 60 μA of electron beam with 85% polarization at beam energies of 4.4, 6.6 and 8.8 GeV comes from the CEBAF accelerator and hits on the polarized ^3He target. The beam polarization will be measured with the Hall

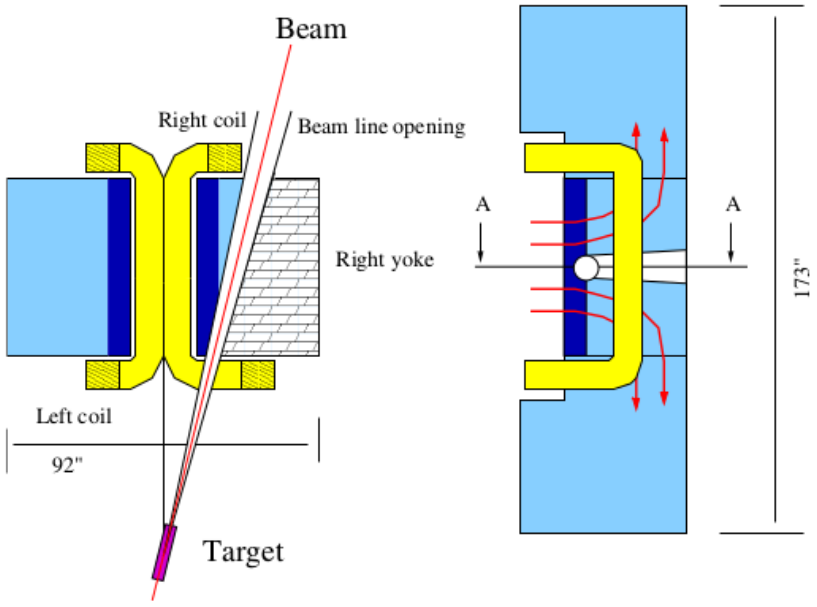

Figure 3-12: Beam line passage in BigBen magnet

A Møller polarimeter with system uncertainty of 3%. The scattered electrons will be detected in the BigBite spectrometer and the neutrons will be detected in the BigHAND nucleon detector.

3.4.1 The Experimental Principle

In the GEn-II experiment, both electron and target are polarized. In 2.2.2, we discussed the double polarization technique and concluded that the asymmetry of the cross section can be written as:

$$A_{phys} = A_{\perp} sin\theta^* cos\phi^* + A_{\parallel} cos\theta^* \tag{3.11}$$

where

$$A_{\perp} = -\frac{2\sqrt{\tau(\tau+1)}tan\frac{\theta}{2}\frac{G_E^n}{G_M^n}}{\frac{G_E^n}{G_M^n}^2 + (\tau + 2\tau(1+\tau)tan^2\frac{\theta}{2})} \tag{3.12}$$

and

$$A_{\parallel} = -\frac{2\tau\sqrt{1+\tau+(1+\tau)^2tan^2\frac{\theta}{2}}tan\frac{\theta}{2}}{\frac{G_E^n}{G_M^n}^2 + (\tau + 2\tau(1+\tau)tan^2\frac{\theta}{2})} \tag{3.13}$$

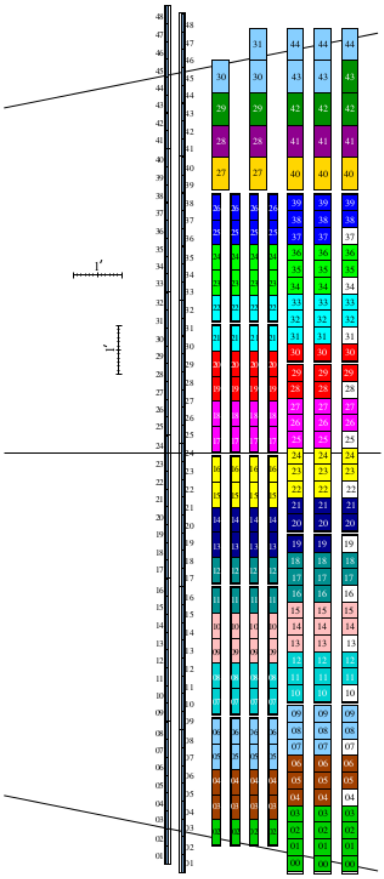

Figure 3-13: The cross section view of the Hall A nucleon detector(BigHAND).

The angle between the target polarization and the momentum transfer is best set to be = 90°. However, due to the definite acceptance of the spectrometer, the angle can not be set to be always = 90°. In this case, the $A_parallel$ term is not completely dropped out and needs to be corrected. In addition, the derivation assumed both the electron beam and the target are 100% polarized. However, in the actual experiment 85% polarized electron beam and 60% polarized polarized ^3He target will be used. Since the neutron is bound in the ^3He nuclei, nuclear corrections needs to be made to accurately extract the form factor ratio. The kinematic points of the experiment is shown in Table 3.3.

E (GeV)	Q^2 (GeV)	θ_E (deg)	P_e (GeV)	Θ_n (deg)	P_n (GeV)
4.4	5.02	48.0	1.73	21.6	3.49
6.6	6.77	34.0	3.00	22.2	4.44
8.8	10.18	34.0	3.38	17.5	6.29

Table 3.3: Kinematics of GEn-II experiment

3.4.2 The Experimental setup

The GEn-II experiment shares the same detector setup with the GMn experiment. Scattered electrons are detected in the BigBite spectrometer arm. In the hadron arm, the BigBen magnet deflects recoil protons to separate them from neutrons. The recoil neutrons are detected by the BigHAND hadron detector. The major difference is in the polarized ^3He target which will be described in detail in the following section. The description of the detector sets can be found in the GMn experiment setup section.

Polarized ^3He target

The GEn-II experiment uses the double polarization method and thus requires a polarized neutron target. However, since the lifetime of the neutron is 881.5 pm 1.5 s, polarized ^3He target was used as substitute for polarized neutron target. In a polarized ^3He, the S state in which the two protons has spins anti-parallel to each other dominates the ground state and 86% of the nuclear spin is carry by the neutron[66][67]. This makes it an effective neutron target. The ^3He was polarized by the spin-exchange optical pumping technique[68] which has been successfully used in GEn-I experiment[11] and many other previous experiments at Jefferson Lab. In the spin-exchange optical pumping technique, alkali metal metal vapor is added to helium. The technique first uses circularly polarized laser light to polarized the alkali metal under a magnetic field, which is known as the process of optical pumping. In the optical pumping process, the S state and P state of the single valence electron of the alkali metal atom each splits into two substates with $m_s = -1/2$ and $m_s = 1/2$ under the applied magnetic field. The energy of the circularly polarized photon from the laser device is tuned so that it can be absorbed by the spin down ground state

$S_{1/2}$ to the spin up excited state $P_{1/2}$. There are two possibilities for electrons in the spin up $P_{1/2}$ state: 1). decay down to the spin up $S_{1/2}$ state; 2). transit via collisional mixing with other atoms to the spin down $P_{1/2}$ state, from which they can decay back to the spin down $S_{1/2}$ state. This whole process will result in accumulation of alkali metal atoms with their valence electron in the spin up ground state $S_{1/2}$, which marks the end of the optical pumping process. The second stage is the spin exchange process where the spin of the polarized alkali metal atom is transferred to helium atom through a hyperfine interaction[69].

Traditionally rubidium works as the alkali metal vapor. The total amount of time to polarized a target cell is about 10-20 hours and the highest polarization of ^3He reached is about 30-40%. In the GEn-II experiment, to increase the polarization level and speed up the polarizing process, a mixture of rubidium and potassium is used as apposed to only rubidium in traditional method[70]. It is much easier for the potassium to transfer its polarization to ^3He atoms in the spin exchange process. The rubidium works as a proxy to receive polarization from the circularly polarized photon and transfer the polarization to the potassium. The addition of potassium greatly increased the efficiency of angular momentum transfer from the circularly polarized photons to ^3He atom(from a few percent to 20-30%) and decreased the amount of time needed to polarize the ^3He target by a factor of 2.

In addition to helium, rubidium and potassium, nitrogen with density around 0.1 amg is added to the target to maximize the polarization efficiency. When electrons decay from $P_{1/2}$ to $S_{1/2}$ state, it can emit an unpolarized photon that can be absorbed and re-emitted by other alkali atoms before escaping the target cell, which decreases the polarization efficiency. When nitrogen is added, the electrons at $P_{1/2}$ state can decay to $S_{1/2}$ state through kinetic collision with the nitrogen molecules without radiation, which reduces the depolarization caused by the unpolarized photon.

The high pressured helium, rubidium and potassium vapor and nitrogen is filled in a glass cell that has two chambers connected by two transfer tubes as shown in Figure 3-14. The top chamber is usually referred as the pumping chamber where the optical pumping and spin exchange between alkali metal atoms and ^3He nucleus happens.

The bottom chamber is the target chamber where high electron beam travels in the direction along the target chamber and interacts with the polarized ^3He nucleus. One of the transfer tube is heated to create convection in the target cell to quickly transfer polarized ^3He from the pumping chamber to the target chamber.

Compared to the target used in GEn-I, the polarized target in GEn-II experiment will be able to provide around 15 times higher effective luminosity.

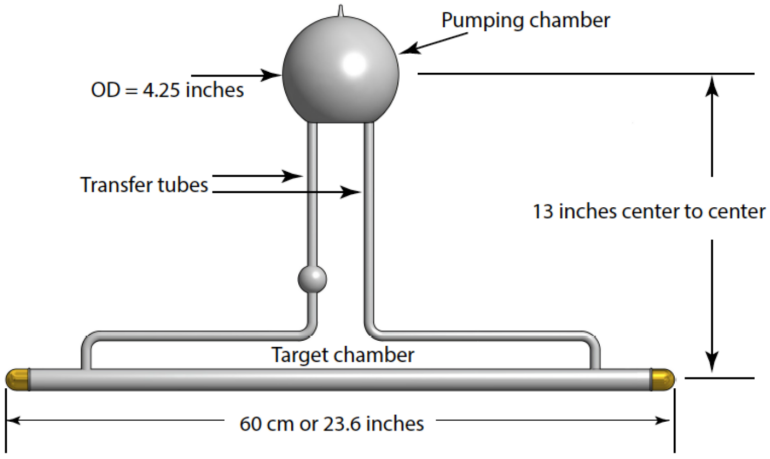

Figure 3-14: The design of the polarized ^3He target in the GEn experiment.

3.5 GEn-RP

The GEn-RP experiment aims to measure the electromagnetic form factor ratio of the neutron, G_E^n/G_M^n, at hour-momentum transfer $Q^2 = 4.5GeV^2$ using recoil polarimetry technique. It utilizes 30 μA polarized electron beam on 15 cm liquid Deuterium target. The scattered electron and neutron is measured by the same experimental apparatus of the GMn experiment. Instead of measuring the cross section asymmetry in GEn-II experiment, the GEn-RP experiment measures the polarization transfer to the recoil neutron by adding a recoil neutron polarimeter between the SBS magnet and the Coordinate detector in the hadron arm. The experimental setup of the GEn-RP experiment is shown in Figure 3-15. The experiment is based on the same principle for the GEp-V experiment discussed in 3.2.1. Descriptions of the rest of the experimental apparatus can be found in 3.3.2.

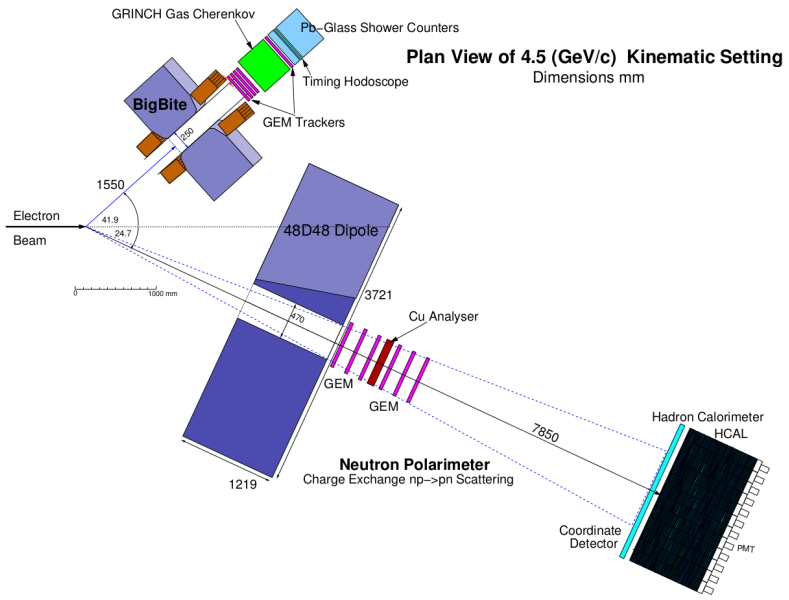

Figure 3-15: The experimental setup of the GEN-RP experiment. A neutron polarimeter is inserted between 48D48 dipole magnet and CDet in addition to the GMn setup at 4.5 GeV^2 kinematic setting.

Chapter 4

GEM Detector

Gas Electron Multiplier(GEM) detector was invented by Sauli at the European Organization for Nuclear Research (CERN) in 1997. GEM belongs to the group of micro pattern gaseous detectors, which were developed starting around late 1980's that detect particles through gas-ionization. Compared to one of the previously widely used gaseous detectors, Multi-wire Drift Chamber, the GEM detector provides higher spatial resolution and much higher rate capability. In this chapter we will first discuss the design and working principle of the GEM detector in the JLab SBS project and then present the characteristics of the GEM detectors.

4.1 GEM Structure and Working Principle

4.1.1 GEM Foil

The GEM foil is the core components of a GEM detector. It is made of a Kapton foil with thickness around 50 μm. The Kapton is covered by NNN-Angtrom layers of copper on both sides. This Cu-Kapton-Cu sandwich is perforated by a high density of holes. The GEM holes usually ranges from 50 μm to 100 μm and has a pitch around 150 μm. The overall structure is shown in Figure 4-1. A very strong electric field is developed in the GEM holes when a few hundred volt electric potential difference is applied across the two copper layers of the GEM foil as shown in 4-2. The electrons

that drift into the strong electric field inside the holes will accelerate between two successive collisions with the gas atoms and gain enough energy to ionize the operating gas. Electron avalanche happens when electrons from these ionization also gain energy from the field and causes further ionization. The GEM operating gases are selected to minimize the likelihood for recombination of the electrons and ions created in this avalanche process and thus to maximize the gain factor. The gain also depends on the GEM hole geometry and on the potential difference across the copper layers of the GEM foil. The typical single foils gain factor used in a triple GEM detector is around 20.

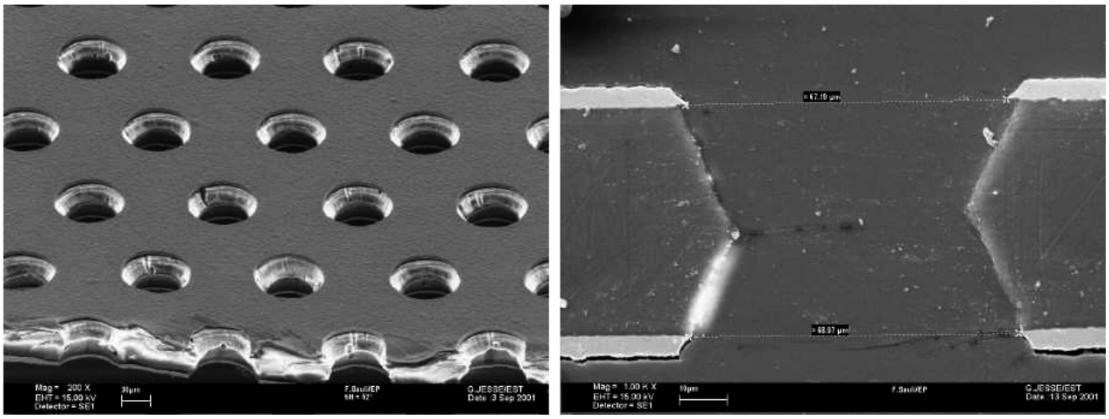

Figure 4-1: Left: GEM foil from an optical microscope. Right: cross section of a GEM hole from an electron microscope

4.1.2 SBS GEM Structure

The SBS GEM is a triple GEM detector with an active area of 60×50 cm^2 based on the design of COMPASS GEM detector. It consists of 3 layers of GEM foils separated by 2 mm between each other, a drift cathode that is 3 mm above the top layer GEM foil and a readout board that is 2 mm below the bottom layer GEM foil as shown in Figure 4-3.

When a charged particle enters the GEM chamber, it ionizes the atoms of the operating gas in the drift region. The electrons from ionization drift downwards in the moderate electric field between the foils and through the GEM foils and are amplified

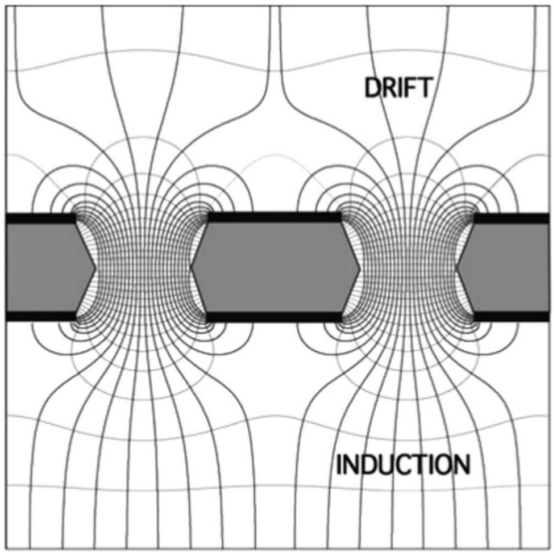

Figure 4-2: The electric field around a GEM foil when voltage is applied to the two copper layer of a GEM foil. The electric field lines are squeezed into the GEM holes and make the field in the holes very high

in the GEM holes. After the amplification stage, the electrons keep drifting towards the readout board. This causes induction of signals in the readout strips generating pulses which can be detected by electronics attached to the readout board.

4.1.3 Particle through Drift Region

GEM detector detection process of a particle is initiated by the interactions between the particle and the matter(the Ar/CO^2 gas mixture) in the GEM detector. While there are many interactions that can occur when a particle travels through matter, the electromagnetic interactions are much stronger than the other possible interactions, and are more likely to happen. In this section we will discuss these interactions for classes of charged particles as well as neutral particles.

Heavy Charged Particles and Electrons

Heavy charged particles deposit energy mostly through coulomb interaction with electrons and atoms in the material. At very high energy, radiation losses like Bremsstrahlung become increasingly more important. The average energy loss rate,

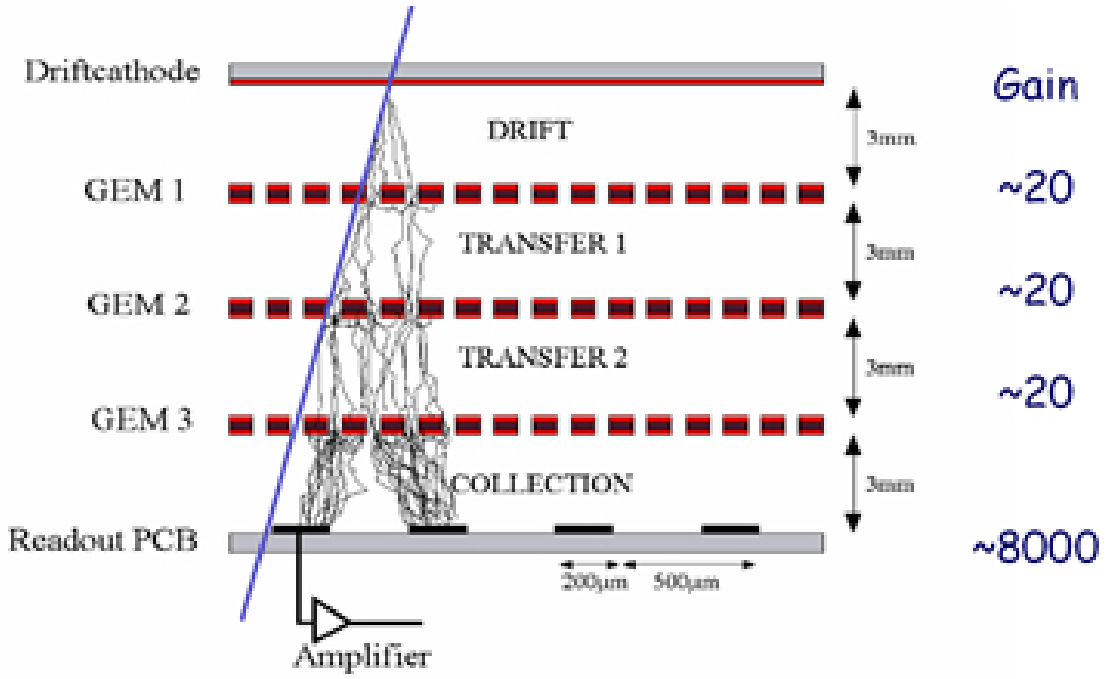

Figure 4-3: GEM structure and working principle.

$\frac{dE}{dx}$, of a moderately relativistic($0.1 \lesssim \beta\gamma \lesssim 1000$) charged particle travelling through material can be well-described by the "Bethe equation" with an accuracy of a few percentage[71]:

$$\left\langle \frac{dE}{dx} \right\rangle = Kz^2 \frac{Z}{A} \frac{1}{\beta^2} \left[\frac{1}{2} ln \frac{2m_e c^2 \beta^2 \gamma^2 W_{max}}{I^2} - \beta^2 - \frac{\delta(\beta\gamma)}{2} \right] \tag{4.1}$$

where $K = 4\pi N_A r_e^2 m_e c^2$, $r_e = \frac{e^2}{4\pi\epsilon_0 m_e c^2}$ is the classical electron radius, z is the charge number of incident particle, Z is the atomic number of the absorber, A is the atomic mass of the absorber, $W_{max} = \frac{2m_e c^2 \beta^2 \gamma^2}{1+2\gamma_e/M+(m_e/M)^2}$ is the maximum energy transfer in a single collision, M is the mass of the particle, I is mean excitation energy, and $\delta(\beta\gamma)$ is the density effect correction due to polarization of the absorber. For practical purposes, the energy loss rate for a given material depends mostly on β and a minimum can be found at $\beta \approx 0.95$. Most relativistic particles have energy loss rate close to this minimum until radiative losses set in. These particles are usually called the "Minimum Ionizing Particles"(MIPs). The recoil protons in the Gep-V experiment, which the SBS GEM detectors aim to detect, belong to this group. For the

Ar/CO^2 gas mixture(at approximately the standard pressure and temperature) that is planned to be used in the GEM detector, the energy loss rate can be calculated using corresponding weight of the material of the mixture as[72]:

$$\left\langle \frac{dE}{dx} \right\rangle = \sum w_i \left\langle \frac{dE}{dx} \right\rangle_i \tag{4.2}$$

For the recoil protons in the Gep-V experiment, the energy loss rate in Ar/CO^2 mixture with ratio of 70/30 deposit around 600 eV in the 3 mm drift region of the GEM detector.

For electrons with energy under critical energy of a few tens MeV ionization dominates. For higher energy electrons Bremsstrahlung dominates. As an example the energy loss rate percentage of electron in Lead is shown in Figure 4-4[72]. A minimum of the energy loss rate can be found around $\gamma = 3.3$, which is similar to the minimum ionizing particles. The electrons to detect in the GMn and GEn-II experiments have energy of a few GeV and roughly deposit 700 eV in the 3 mm Ar/CO^2 gas mixture in the drift region.

Photons

Photons interacts with matter differently from heavy charged particles and electrons. As shown in Figure 4-5, three main processes contributes to the energy loss of photon through matter: photoelectric effect, Compton scattering and pair production. At low energy photoelectric effect dominates. Compton scattering rises at mid energy and pair production dominates above tens of MeV. Most of the random backgrounds from the SBS experiments have low energies and the photoelectric effect is the main process these photons deposit energy into the GEM detector.

4.1.4 Ionization

When more energy than the average ionization energy of the gas mixture is deposit, an electron-ion pair is generated. The total number of electron-ion pairs is given

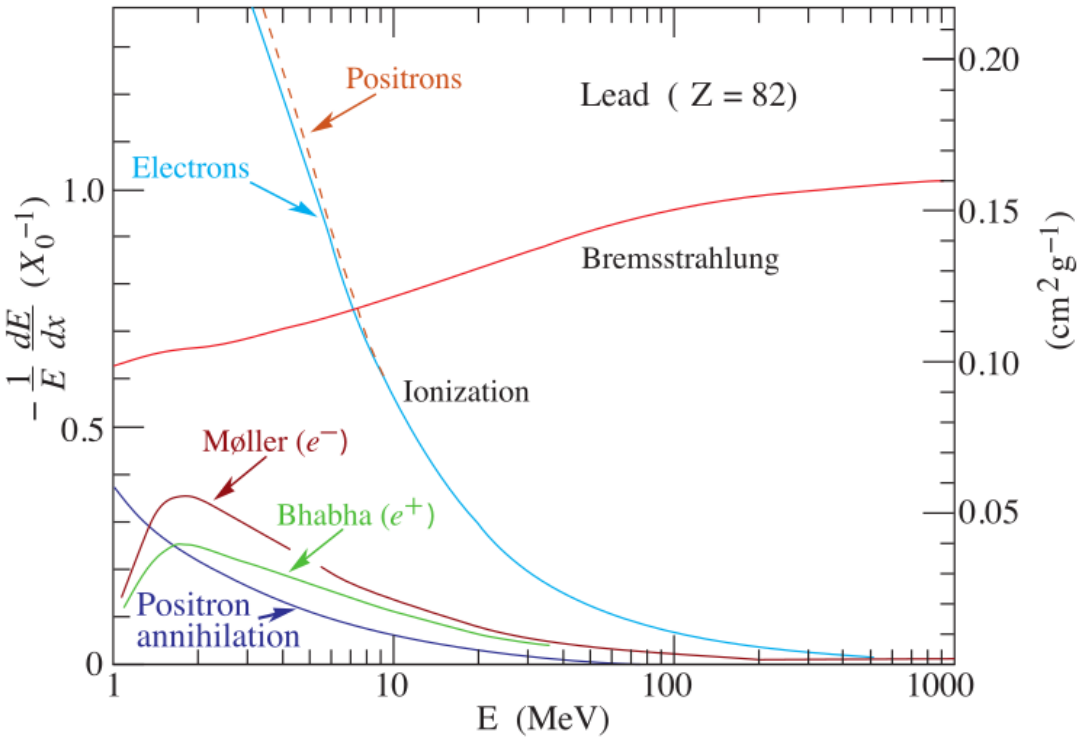

Figure 4-4: The fractional energy loss of electron and positron per radiation length in lead as a function at different energy. Plot reproduced from [22]

by(Sauli 1997):

$$n = \frac{\Delta E}{W_i} \tag{4.3}$$

where ΔE is the total energy deposit and W_i is the average energy needed to produce one electron-ion pair. For the $Ar/CO^2(70/30)$ gas mixture, $W_i \approx 26eV$

4.1.5 Drift and diffusion

Electrons and ions from ionization will drift along the electric field in the GEM chamber. Electrons drift towards the readout board while ions drift towards the cathode with a speed orders slower due to their much higher mass. Here only the drift speed of electrons is discussed since the signals recorded originates from electrons. The average drift speed depends on the strength of the field and the type of gas mixture in the chamber and the dependency is shown in Figure4-6. One effect the drift speed has on the GEM characteristics is the time resolution of the final signal.

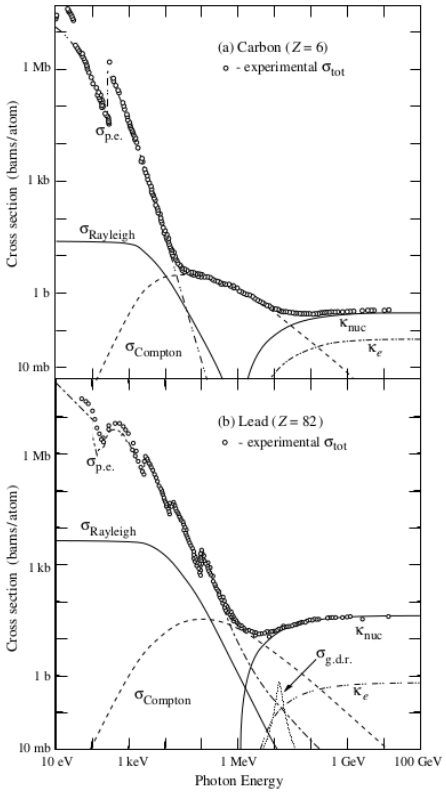

Figure 4-5: The cross sections for different process as a function of energy. The top plot is for scattering in carbon and the bottom is for lead. Plot reproduced from [22]

This is especially important for the high background SBS experiments that utilizes signal arrival time as criteria to reject random GEM hits. Given the size of the drift region, gas mixture and the drift voltage, the intrinsic time resolution of the SBS GEM chambers is around 10 ns. More details on the time resolution of SBS GEM chambers will be discussed in later chapters.

In the mean time of drifting in the filed, electrons and ions also diffuses due the scattering with gas molecules which diversify the velocities of the electrons and ions. Both longitudinal and transverse diffusion is present. The longitudinal diffusion drops the time resolution by tiny bit and the transverse diffusion affects the final spatial resolution of the chamber. As an approximation model, the distribution of the final charge collection on the readout board can be treated as Gaussian. The standard deviation of the distribution can be expressed in terms of the diffusion constant of

the operating gas D and the total time elapsed t as:

$$\sigma = \sqrt{2Dt} \tag{4.4}$$

More realistic models will be discussed in later chapters and applied in the digitization of the GEM simulation data.

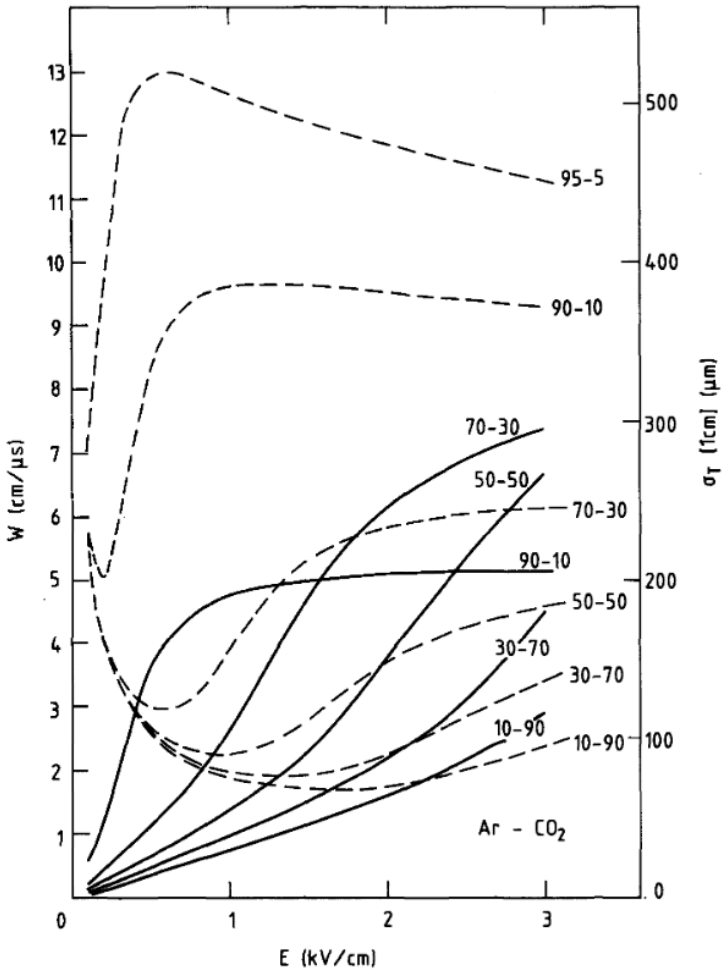

Figure 4-6: The drift speed and diffusion rate of electrons in mixture of $Ar - CO_2$ within different Ar/CO_2 ratio. Plot reproduced from [23]

4.1.6 Amplification

As described above, the GEM foil provides a strong electric filed in its GEM holes when voltage is applied to its copper layers. With this field, an electrons that en-

ters the GEM holes gains enough energy in between collisions to ionize the next gas molecules and generate another electron ion pair, which results in two electrons. A chain of such processes happens and results in an electron avalanche. The GEM detector works in the "proportional" region, where the space-charge(mainly ions which moves slower compared to electrons) from ionization has negligible effects on the initial field and the field is static. In such a region, final the number of electrons after the amplification is proportional to the initial number of electrons and the amplification factor is a constant with given GEM foil structure and given operating voltage.

4.1.7 Charge Collection on Readout Plane

The SBS GEM detector adopts the 2D Cartesian strip type readout. The readout board consists two sets 5 μm thick copper strips that are orthogonal and spaced by 50 μm Kapton as shown in Figure 4-7. The strips has a pitch of 400 μm. The specific strip width of each set is optimized in a way that the final signal size for a given hit are the same in the two axis. This type of readout keeps the total number of channels at a manageable level even for the very large GEM active area to cover for the SBS experiments. As a cost friendly solution for large scale experiments, this type of readout can suffer from hit ambiguity issue in multiple hit situation. In moderate cases, one can utilize the signal amplitude and arrival time to help identifying the correct combination of hits in the two axis. In more severe situations, pad readout should be considered to replace strip readout to reconstruct meaningful hits. For experiments that has localized high rate region, a combination of pad readout and strip readout can be adopted.

After the amplification stage, the cloud of electrons induces current in the readout strips even before it reaches the readout board as shown in Figure 4-9. The signal strength maximizes at a certain stage before the electrons reaches the readout strips. It starts to decrease as more electrons is collected. The signal on the strips is amplified and processed using the APV-25 chip before being sent to be digitized and recorded. More details on the data acquisition system for GEM detector will be discussed in the end of this chapter.

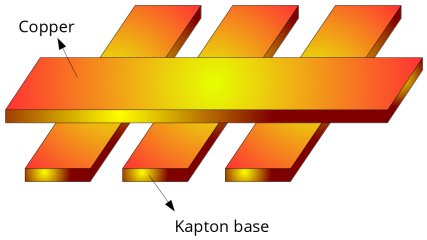

Figure 4-7: The readout strips of GEM detector.

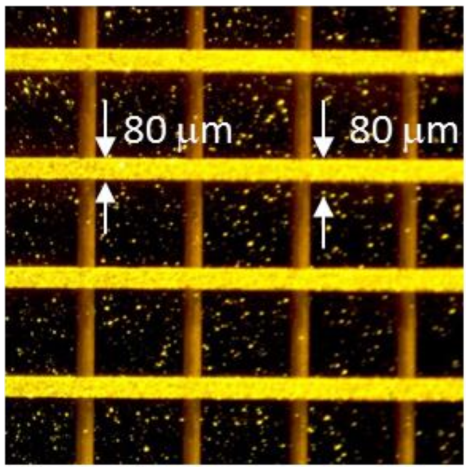

Figure 4-8: Readout board under scope

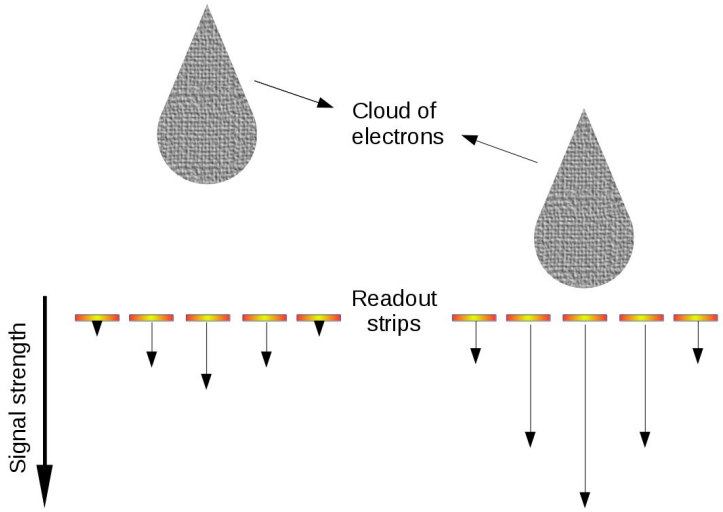

Figure 4-9: The induction of signal in the copper readout strips.

4.2 Performance under High Intensity X-ray

In the high rate SBS experiments there will be very high charge deposition into the GEM detector over large tracking area. This large charge deposition could affects GEM performance in multiple aspects. A X-ray test hut was built at UVa to study the performance of the SBS GEM detectors under high rate conditions. The setup provides 5 photon energy settings from 10 keV to 50 keV and rate up to 100 MHz/cm^2 at the surface of GEM detector while covering the whole active area of 60x50 cm^2. Photons in this energy range interacts with the operating gas mainly through pho-

toelectric effect. Within the 3 mm drift region, the conversion rate is roughly 0.5%. With the highest current setting, the X-ray tube is able to deposit around 100 times more charge than the most severe scenario in the SBS experiments. The intrinsic gain of a GEM foil has been proved to be stable up to 100 MHz/cm^2[23]. Despite this knowledge, number of other more practical issues could arise when operating GEM detector both under high rate situation and over large active area. In this section we will discuss these issues and the performance of the SBS GEM detectors.

4.2.1 X-ray Test Setup

The test is performed within a 1.5 m x 1.5 m x 2 m hut made of wood. The outer surface of the box is covered with 3 mm lead sheet as radiation protective layer. A X-ray tube is placed 70 cm away from the GEM detector and uniformly covers the whole active area of the GEM detector. The X-ray acts as large size of random backgrounds and a ^{90}Sr radiation source is placed around 10 cm away from the GEM detector acting as the hit of interest to study the characteristics of the GEM detector. An overall picture of the setup is shown in Figure 4-10

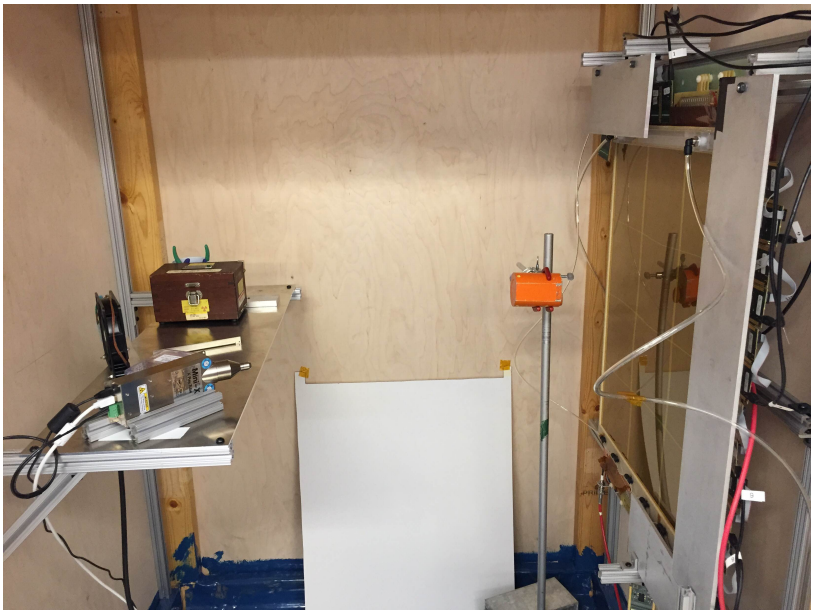

Figure 4-10: The X-ray test setup

4.2.2 GEM Chamber Stability

Under high level of charge deposition over large active area, the Kapton gas window of a traditional triple GEM "sticks" to the cathode after several hours of operation like shown in the top section in Figure 4-11. This is caused by the charge accumulation between the gas window and cathode due to the presence of electric field. This issue was fixed by replacing the normal Kapton gas window with aluminized Kapton foil and applying a potential same as the potential applied to cathode to the aluminized layer as shown in the bottom section in Figure 4-11

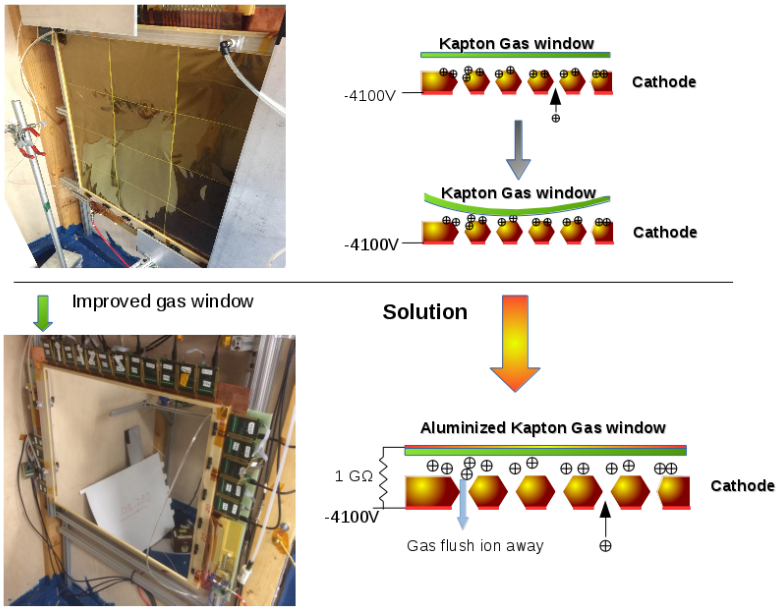

Figure 4-11: The new aluminized Kapton foil. The top section shows that the gas window sticks to the cathode after operation under high rate. The bottom section shows that the improved gas window stays stable even after two week's high rate operation.

4.2.3 Gain stability

The intrinsic gain of GEM foil at given voltage stays stable up to 100 MHz/cm^2. However, when the active area of the GEM detector is large enough like in the SBS experiments, the total amount of charge deposition would also increase the GEM current by significant amount. We observed a 20% increase in GEM current when

GEM is operated under a charge deposition rate equivalent to that of 7 MHz/cm^2 MIPs like shown in Figure 4-12. This increase of the total GEM current modifies the voltage distribution vastly and could cause drastic drop in the effective gain of the GEM detector when the GEM is operated at very high rate, Figure 4-13. In the case of SBS experiments, the drop of the gain is within 20% and can be fixed by simply increasing the operating voltage. In more hash conditions, a better design of the high voltage divider that minimizes the change in GEM current at high rate should be considered.

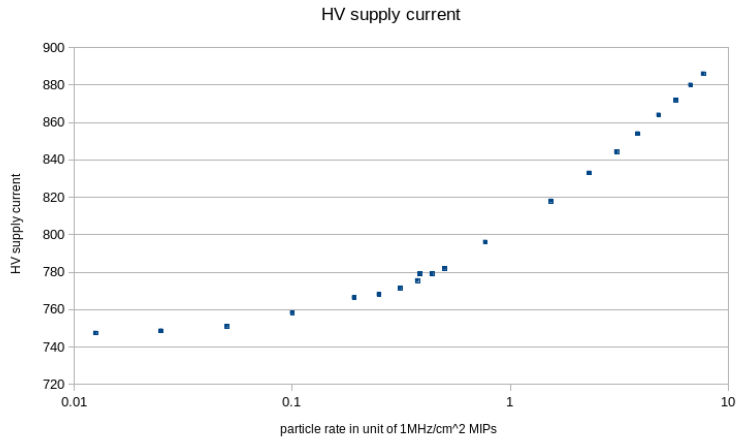

Figure 4-12: GEM current dependence on rate

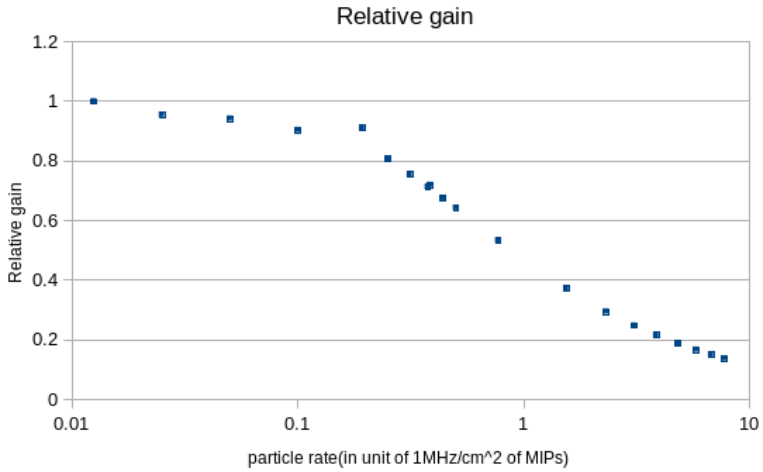

Figure 4-13: SBS GEM effective gain dependence on rate

4.2.4 Charge Ratio Stability

As stated in section 4.1.6, the ratio of the signal strength(usually know as "charge ratio") in two axis is roughly 1 by selecting the readout strip width. It provides a way of better matching hits in the two axis and decreases hit ambiguity. This is an important character of the SBS GEM detectors to have, especially in SBS experiments where there is high level of random backgrounds. At high charge deposition level, the charge ratio was observed changing by up to 50% due to the charging up effect in the readout board of a previous version in which there is spacing Kapton exposed to the drifting electron cloud. After improving the readout board, a test was done to study this effect and the result shows that the charge ratio of SBS GEM detectors holds constant even at the worst situation in SBS experiments, as shown in Figure 4-14

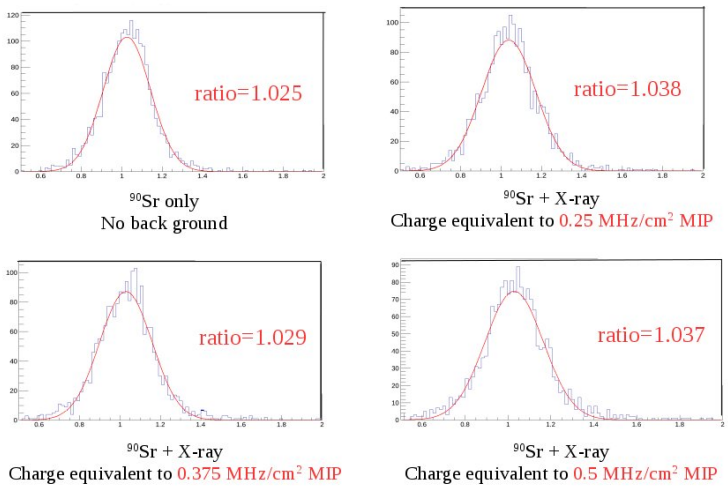

Figure 4-14: Charge Ratio between two readout axis at different background rate. The test is done with highest X-ray setting that corresponds a background rate equivalent to 0.5 MHz/cm^2 minimum ionizing particle.

4.3 Test Run in Hall A at JLab

A set of 5 GEM modules built at UVa was tested parasitically in Hall A at JLab during the running of DVCS and GMp experiment in the Fall of 2016. The main goal was to test the performance of the GEM detectors in real experimental conditions

and the capability of the background rejection algorithm. With the limitation of the available locations for the setup, an occupancy of 1.5% was reached in this test. At this occupancy, signal of interest was separated from random backgrounds very well and accurate tracking results was achieved.

4.3.1 Setup

The setup was located at an angle of 70° from the downstream of the beam and 12 meters away from the target. It faces directly to the target and consists of a 5-layers GEM tracker, scintillator layer in front of the tracker and calorimeter behind the tracker. A picture of the setup is shown in Figure 4-15. The GEM tracker consists of 5 GEM modules spaced by 13 cm from each other. $Ar/CO^2(70/30)$ gas mixture was supplied to each GEM module in parallel with rate of 5 L/h. The trigger comes from the coincidence of the scintillator layer and calorimeter to ensure a good track of through the GEM tracker.

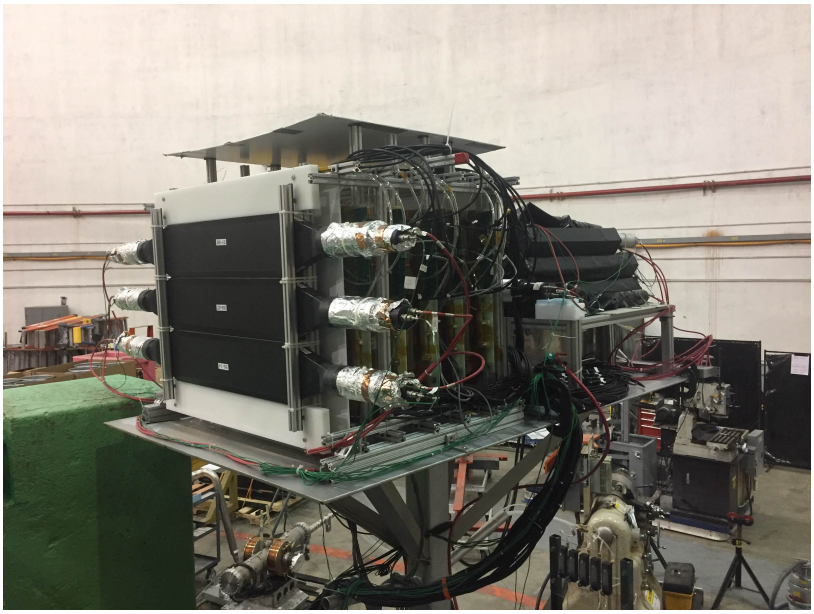

Figure 4-15: Hall A test setup

4.3.2 Calibration

GEM detector alignment

The SBS GEM detectors offers a spatial resolution around 70 μm when particle travels through upright. To achieve the best possible tracking accuracy from the 5-layer GEM tracker, the GEM modules needs to be aligned to very high level. In coming SBS experiments, experimental surveys can be performed and used for alignment. However, difficulties can be expected given the fact that displacement can happen among the 4 GEM modules that made up a full tracking layer. Here a method of extracting the offsets between GEM detectors from experiment data was developed and tested. The method is based on two facts. First, the tracks are straight when no magnetic field is present(the angle deviation from multiple scattering through the SBS GEM detector is negligible). Second, The overall width of position residual of the reconstructed tracks reaches minimum when the detectors are perfectly aligned. For this specific 5-layer GEM tracker, there are 24 independent parameters(3 translational offsets and 3 rotational offsets for each module) to determine to align the last 4 GEM detectors to the first one. The method uses a gradient descent algorithm for multiple iterations with increasing precision to find the minimum of the width of residual distribution. It was first tested with a set of cosmic data and then applied to the Hall A test data. The tracking residual using results from this method is shown in Figure 4-16.

GEM Timing correction

Good timing resolution in the GEM detector is one of the keys to reject random background hits and false tracks. The signal induced on readout strip by a hit is sent to one channel on the APV-25 chip to be amplified and shaped. The DAQ system will readout 6 sample data points of the signal pulse. Each sample is spaced by 25 ns. In the analysis of the GEM data, the 6 sample points is fitted to the APV-25 shaping function to extract the peaking time of the signal pulse. The timing of a hit is defined as the time interval between trigger and the hit's peaking time. Since the APV-25

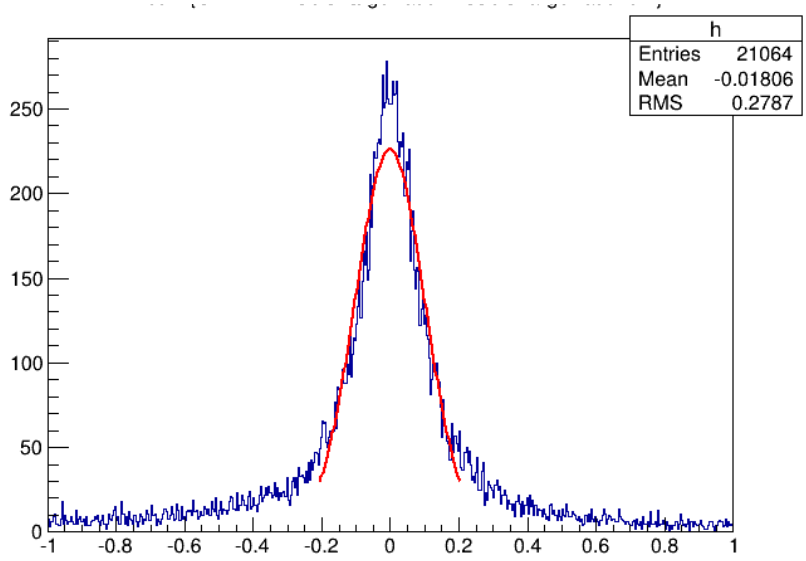

Figure 4-16: Position residual averaged over 5 layers

chip runs on a 40 MHz clock, the signal arrival time will be shifted by a certain amount that depends on the phase of the trigger in the APV-25 clock, as shown in Figure 4-17. For hits that comes from the same particle that triggers the DAQ, the timing of the hits should be centered around a certain value that only depends on the flight time of the particle, drifting time of the hit in the GEM chamber. While for a hit that comes from random background, the timing would have no correlation with the trigger and distributes uniformly. It is then possible to use this timing to reject random background hits. The better this timing resolution is, the more background can be removed. It is thus crucial to correct the random shift between trigger and APV-25 clock to get better timing resolution. The correction is done by sending both APV-25 clock and the trigger to a channel of TDC unit and measure the interval between them. Much better timing resolution of a trigger related hit was achieve after the correction as shown in Figure 4-18.

In the SBS GEM detectors, signal of a hit is received in readout strips of both x and y axis of a Cartesian type readout board. The timing of the signal in both axis should be tightly correlated and thus provides a way of matching up hits from the two axis to form a 2D hit. The timing correction mentioned above also significantly improved this correlation, which allows much tighter correlation cut can be set to

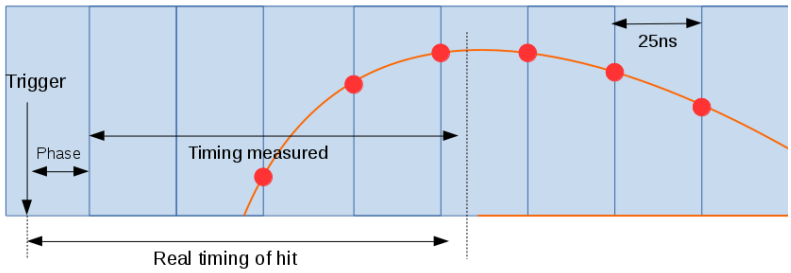

Figure 4-17: Timing shift due to the random phase of trigger in the APV-25 clock

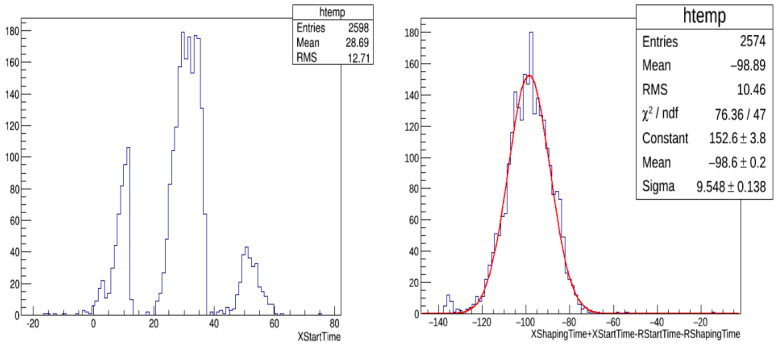

Figure 4-18: Timing resolution before and after clock phase correction

reject mismatched hits as shown in Figure 4-19.

The timing resolution of a GEM detector can also be affected by the uniformity of the GEM detector. Non-uniformity can lead to different drifting time needed for the electron to reach the readout strips at different location of the detector. This effect was seen to worsen the timing resolution of GEM detector by 2 to 5 ns in the Hall A test at JLab. To correct for this effect, localized timing offset was calculated as shown in Figure 4-20. Figure 4-21 shows the improvement of timing resolution for a GEM chamber that benefits the most from this correction in the 5 chambers used in the test.

4.3.3 Results

The main goal of the GEM test in Hall A was to test out the SBS GEM detectors in real experimental conditions and to test the background rejection analysis method.

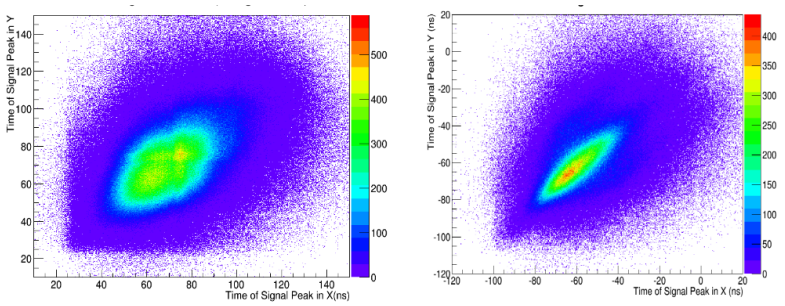

Figure 4-19: Timing correlation between readout axis before and after clock phase correction. The plots includes correctly matched hit, random background hits and mismatched hits, the high populated area corresponds to the good hits, the correlation of the good hits improved substantially after the clock phase correction.

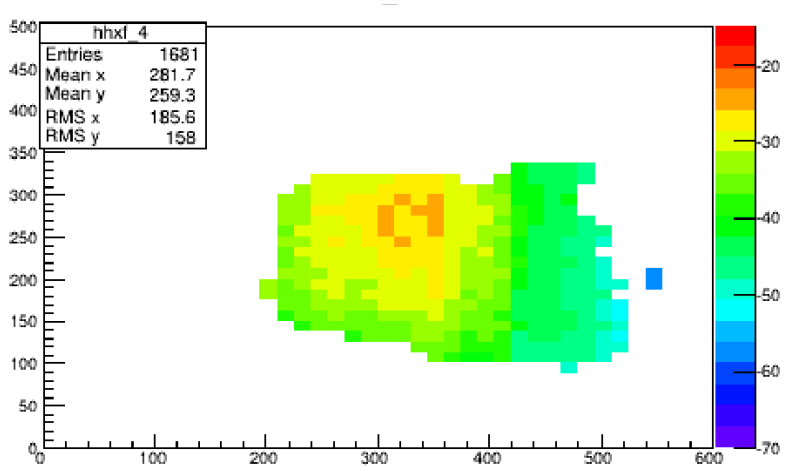

Figure 4-20: 2D plot of the timing offset at different locations. The acceptance of the setup covered only part of the detector.

The total active time of the test is about two weeks during which all of the 5 GEM modules used in the test showed good stability. Another objective of the test was to test the GEM analysis, especially background rejection method, under background level as high as the SBS experiments. Due to the limitation of available location of the setup, the average occupancy on the GEM detector is around 1.5% and the proposed GEM analysis routine easily separated the background hit and trigger correlated hit very well as shown in Figure 4-22. The detail of the GEM background rejection analysis will be discussed in Chapter 6 and results with much higher intensity background using digitized simulation data will also be presented.

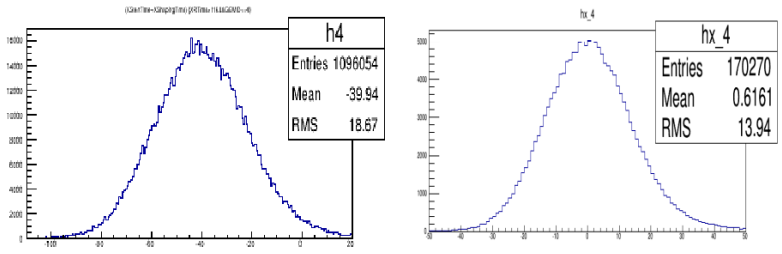

Figure 4-21: The left plot is the timing resolution before correcting localized timing offset. The rms value is around 19 ns. After the correction the rms value improved to 14 ns

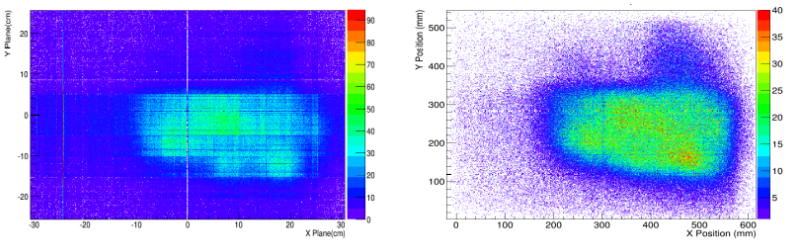

Figure 4-22: 2D hit map before and after background rejection

4.4 Fast GEM Data Acquisition System

In the SBS experiments, as a result of usage of large area and high resolution tracking detector, the raw data volume is extremely large. Taking the GMn experiment for example, given the 5-layers GEM tracker configuration, there are 40k channels to read on a total of 23 MPDs(Multi Purpose Digitizer). The total raw data volume per event is 0.5 MB(40k channels * 6 samples * 2 Bytes). At the trigger rate of 5 kHz, the raw data rate is 2.5 GB/s. This huge data rate is handled by a SSP(Sub System Processor) based system with online data reduction that can reduces the data size by factor of 10 to 15 with the 20% to 25% GEM occupancy in GMn experiment. The scheme of the system is shown in Figure 4-23.

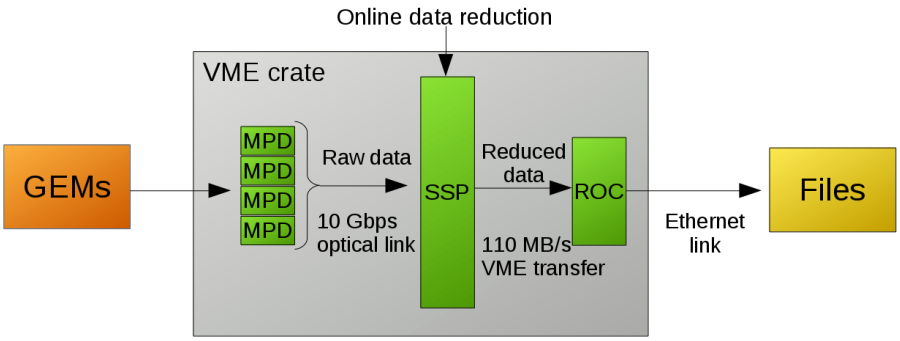

Figure 4-23: Data flow chart of the current SSP based system. MPD digitizes signals from APV card on GEMs and send it to SSP. Every 4 MPDs share a 10 Gbps optical link which goes into 1 of 8 optical port on SSP. Real time data reduction is performed on SSP and the SSP send reduced data through VME backplane which has an average transfer rate of 110 MB/s to readout control CPU.

4.4.1 Electronic hardware

APV-25

The APV-25 is a 128 channel analogue pipeline chip with low power consumption and low noise. It is adopted by the SBS project to read the GEM detectors for its radiation hardness and relative low cost per channel. The chip contains 128 channels of pre-amplifier and shaper driving a 192 column analogue memory. The chip is operated with a 40 MHz clock. The I2C standard is used for chip configuration, bias settings and error states. APV-25 chip outputs a signal in differential current form in the range of $\pm 4\ mA$. There are synchronisation pulses every 35 clock cycles when the chip is idle. When a trigger is registered, the chip waits until the start of the next 35 clock cycle period to output the data. The analog data consists a digital header, a digital address, an error bit, and an analogue data stream of 128 clock cycles representing the signal size of 128 channels.

MPD

The MPD Board is a FPGA based board designed by INFN to digitize and organize data from up to 16 APV front-end cards. It is responsible for controlling,

configuring, and receiving analog data streams from APV front-end cards and transmitting both the control and configuration signals. A schematic is shown in Figure 4-24. The MPD 4.0 is developed to avoid the use of expensive and not easily procurable HDMI type B cables, which is initially adopted in the original design. The board has been implemented in VME 6U x 160 mm format. After the analog-digital conversion the signals can be further processing such as zero suppression of the raw data. However, due to the limited resources on the MPD and the high rate running condition, this feature is turned off and the work is handled by the SSP unit. The internal clock of the MPD can be read from the front panel by injecting it into a TDC. This clock can be measured together with the event trigger to correct for the trigger jitter mentioned in earlier sections.

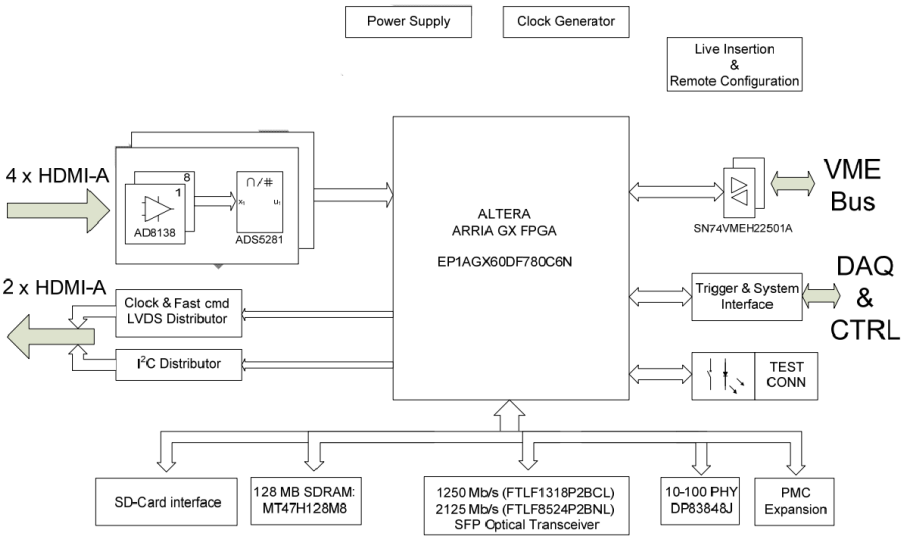

Figure 4-24: Block diagram of the MPD 4.0. The power supply voltages are generated on board with a single +5 V input. Thus the use of a VME crate is not mandatory. Once both control and data transfer of the MPD are done using fiber links driven by the SSP, the MPDs can be separated from readout controller.

SSP

The Subsystem Processor(SSP) is a module originally designed for processing logic operation for the Level 1 trigger for new coming 12 GeV experiments at Jefferson Lab. It can receive data streams from up to 8 channels through a 10 Gbps optical fiber link.

After processing data streams from multiple channels, the SSP can pass the output to either a Global Trigger Process(GTP) through the 2 lane full duplex copper link on the VXS backplane or a readout control CPU through the VME64x backplane. In the SBS experiments, each SSP handles data streams from up to 32 MPDs that are separated into 8 groups. Each group of 4 MPDs shares one optical fiber link.

4.5 GEM online reduction

4.5.1 Base version without online data reduction

The conventional SSP-MPD system without online processing has been established and used to take stable cosmic runs. In this version the SSP simply takes in all raw data and output it to the readout control CPU(ROC). The rate is limited by the 110 MB/s VME backplane link between SSP and ROC. For the full system of GMn experiment, the maximum trigger rate using this scheme is about 220 Hz per VME crate. For example, if there are 3 VME-ROC-SSP sets available, the rate cap is 660 Hz.

4.5.2 Online data reduction algorithm

In the online data reduction version, the SSP performs a set of computations and reduces data that is either from non-fired channels or fired channels of random background hits. The removal of non-fired channels is based on zero suppression. The removal of background channels is based on the random timing of background hits relative to trigger. The data reduction algorithm was tested with events that had high local occupancy up to 50% in the 2016 Hall A GEM test run that had an overall occupancy of 1.5%.

Zero suppression

Online zero suppression is the first part of the data reduction procedure. It requires computing the common mode of APV samples in real time(Figure 4-25). The accuracy

of the common mode calculation is the key to ensuring the correctness of the zero suppression. This is especially true in high occupancy scenarios as every fired channel may bias the common mode by considerable amount.

Traditionally in offline GEM analysis, this common mode is found by removing a certain number of channels that have higher rank after sorting on them by their ADC values aiming to remove fired channels. Since sorting is both computationally and memory expensive for the SSP, another simple yet effective algorithm is devised for the online reduction. The method takes the average of all channels that have ADC values between a wide potential range of common modes and then removes channels that have ADC values 10σ(σ: pedestal noise rms) higher than the average. After 3 iterations, the final average is taken as the common mode. This method uses constant memory and is 4 times faster than the sorting method. It was implemented and tested using data from the GEM test run in Hall A against the traditional offline analysis method and shows good accuracy as shown in Figure 4-26. The comparison is done up to 50% occupancy, where 64 channels out of all 128 channels in APV fire. The data came from the GEM test run in Hall A where overall occupancy was 1.5%. However, local occupancy within one APV can often be much larger. APVs are categorized by the total number of fired channels to look at the difference of the two methods at different occupancy level. As shown in the figure 4-26, the difference is well under 20 ADCs for occupancy up to 50%. For comparison, the ADC of a typical MIP hit in GEM is more than 400

Random background hit removal using time information of hits

The removal of background hits in the online reduction procedure is designed to be loose to avoid discarding good hits. It is based on the fact that the hit of interest is correlated with the trigger and its peak can be placed in the middle of the readout window, as shown in Figure 4-27. Since only on extremely rare occasions the signal has its peak in either the first or last time sample, channels that have such characteristic can be recognized as hits from random background and removed. Careful considerations needs to be taken here since this removal could potentially

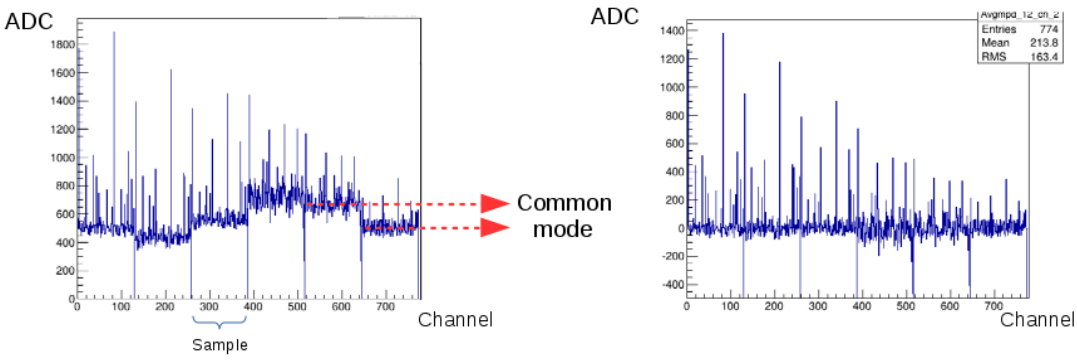

Figure 4-25: The plot on the left shows how the ADC baseline of channels in one APV fluctuates from sample to sample and thus needs to be computed and offset before applying threshold cut for zero suppression. Fired channels within the group bias the actual baseline and need to be excluded. The plot on the right is after common mode correction

remove a good hit since background hits can overlap with a hit of interest in high occupancy situations. However, usually when a background hit is large enough to make a channel's signal peak at the first time sample, the information of the good hit on that channel is not retrievable and the channel information is useless anyway. It depends on the final hardware capability and rate requirement whether or not to apply this removal. Overall, this removal can reduce about 60% of the total data size.

4.5.3 Hardware implementation status

As stated above, the correctness of the data processing algorithm has been tested using Hall A GEM test data by running the algorithm in parallel with traditional offline analysis and making a direct comparison. The proper implementation of the algorithm into the SSP has been verified with a small scale version of the final system. In the current system the SSP supports up to 4 MPDs. The final version aims to support up to 24 MPDs. This system has been implemented into the Jefferson Lab's standard data acquisition system CODA and used to take stable cosmic runs. The result is consistent with results from a system using offline data processing.

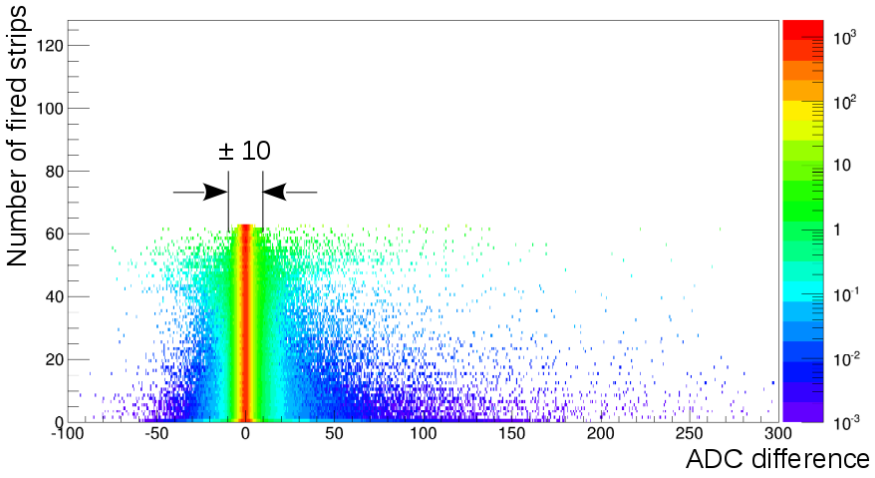

Figure 4-26: The difference between common mode results from offline analysis method and the new method used in the online data reduction system at different occupancy levels.

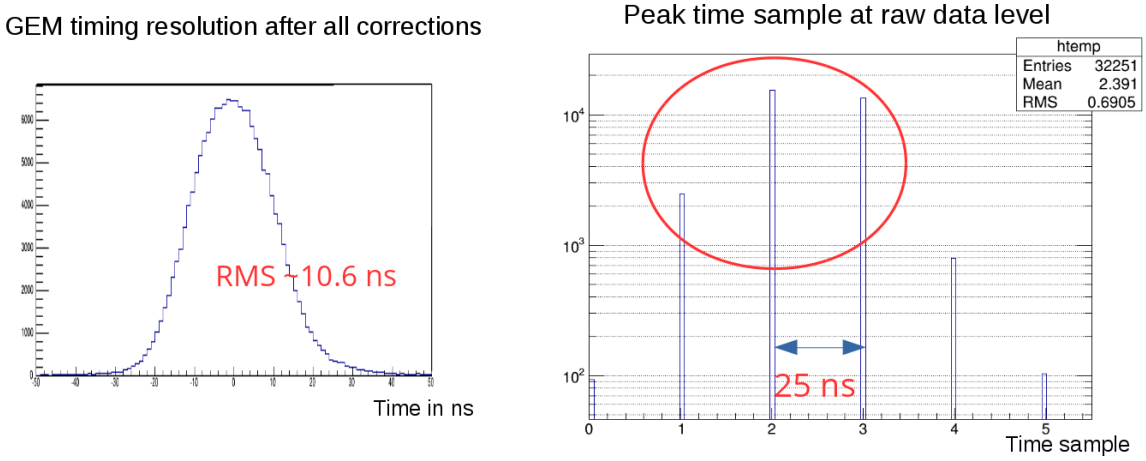

Figure 4-27: The final timing correlation of good hits with trigger has rms around 10 ns after corrections as shown in the left plot. At the raw data level before any correction, the timing of a good hit stays within 3 to 4 25 ns time samples(in red circle). This makes it possible to reject non-trigger-correlated background hits if a hit's peak time sample is out of this range.

Chapter 5

Tracking Analysis under High Accidental Background Rates

As mentioned in early chapters, the common challenge in carrying out the SBS form factors experiments comes from the high background rate. At the instrumentation level, the GEM detector is adopted as the tracking detector for its excellent rate capability, which ensures stable operation under high background rate. At the data acquisition level, the MPD-SSP based data acquisition system is designed and implemented into the Jefferson Lab's standard data acquisition framework CODA. A small scale of the system has been fully tested and exhibits expected performance. This ensures proper transfer and recording of the high volume data of the detector sets. In this chapter, we will discuss the most essential aspect of the challenge: how to efficiently interpret the data with high levels of contamination from background hits. Of all the analysis, the GEM tracking analysis suffers the most from the high background rates and is the most difficult part to handle. First, the analysis needs to be able to efficiently reconstruct the primary track in the GEM detectors. Second, the primary track needs to be identified from a large number of false tracks caused by the background hits. Third, the reconstructed primary track needs to have good resolution. A high background specialized tracking analysis is develop by exploiting character of the GEM detector. To demonstrate the effectiveness of the analysis, a comprehensive Geant4 simulation of the GMn experiment is done. The simulation

is further digitized by a digitization library in a way as realistic as possible where electronic noise, realistic GEM hit cluster profile, APV-25 cross talk and timing uncertainty are all taken into account. Finally, the GEM tracking analysis is applied on the simulated raw data files and evaluated by comparing its result to Monte Carlo information from the simulation.

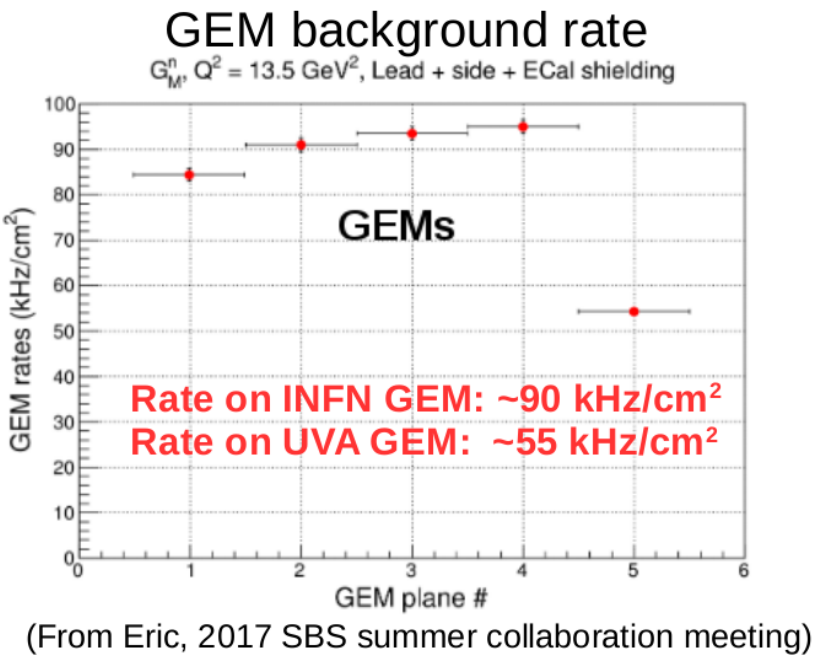

Figure 5-1: Random background rate in GEM layers in GMn experiment

5.1 Geant4 Simulation of GMn experiment

The Geant4 simulation of the GMn experiment in this thesis incorporates a 15 cm unpolarized deuteron target and an electron beam with current of 30 μA. The complete setup of the experiment in the simulation is shown in Figure 5-2. The accidental background rate in GEM from Geant4 simulation is around 100 kHz as shown in Figure 5-1. Elastic events are generated from an elastic generator and mixed with random background hits from a beam on target simulation. The amount of background to mix with 1 elastic event is determined by matching the expected background rate.

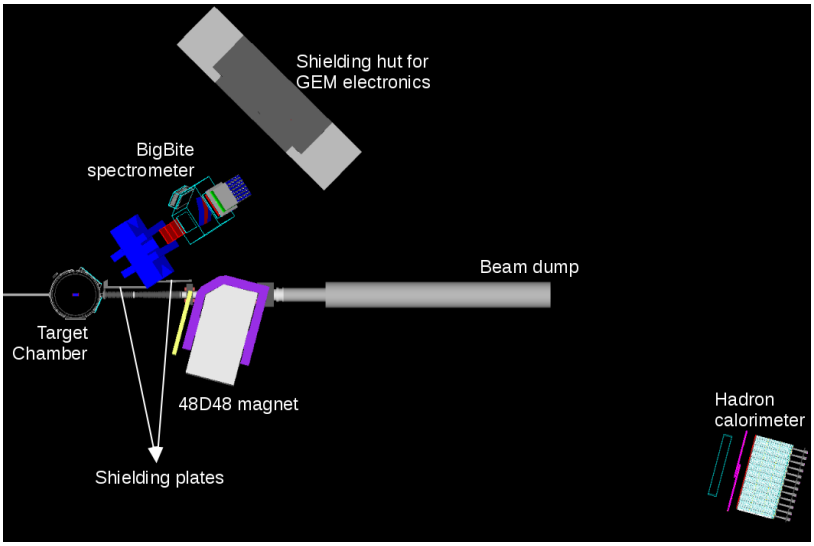

Figure 5-2: The experimental setup in Geant4 simulation (top view).

5.2 Digitization

The digitization procedure takes in the Monte Carlo simulation results and mixes in realistic effects to make the output raw data file as realistic as possible. The following are the major parts built based on experience with real data from cosmic tests, Hall A beam tests and X-ray tests.

5.2.1 Ionization

Based on the hit position, energy deposition and range of hit from simulation, electron-ion pairs are generated in the GEM drift region. The electron-ion pairs are distributed randomly in the range the hit covers within the GEM drift region. The number of electron-ion pairs is proportional to the energy deposition of the hit. Thus for a hit that is from the photoelectric effect of a soft photon, the cluster amplitude and size will be much larger than a hit from a MIP-like particle because such hits generally has much larger energy deposition. The GEM hit cluster size after the digitization in the GMn experiment is shown in Figure 5-4, which is actually much larger than in the previous assumption of three.

5.2.2 Amplification and Drift

The electrons are then amplified when drifting through GEM foils and propagated to the readout plane. Diffusion is also being taken into account. The ADC gain is tuned such that the MIP-like elastic electron in the GMn simulation shares similar hit cluster profile as cosmic hits from real cosmic tests(Figure 5-3).

5.2.3 Electronic noise

Pedestal noise of the same level as real data is added into both fired channels and non-fired channels. Common mode, which describes the group baseline level of 128 channels on an APV card, is not set explicitly in the digitization. However, it is also effectively being taken into account just like in real data because the analysis code always tries to figure out the common mode instead of using the real baseline of "0".

5.2.4 Cross talk

In the MPD-APV readout system, a strong hit channel always introduces a small detectable image signal in adjacent channels. This effect, often referred as "cross talk", is seen and measured in the PRad experiment. In the digitization, the ratio of the cross talk signal to the original signal has an average of 0.1 and an rms of 0.3. A cross talk signal is added to corresponding channels for every original signal.

5.2.5 Signal jitter in time

Signal from the MPD-APV readout system has a random jitter with a maximum of 25 ns due to the non-synchronization between the APV clock and MPD clock. Although this time jitter will be measured and corrected in real data runs, there will still be additional time residuals caused by this effect. This additional time uncertainty is also added to the intrinsic time uncertainty of GEM signals in the digitization procedure.

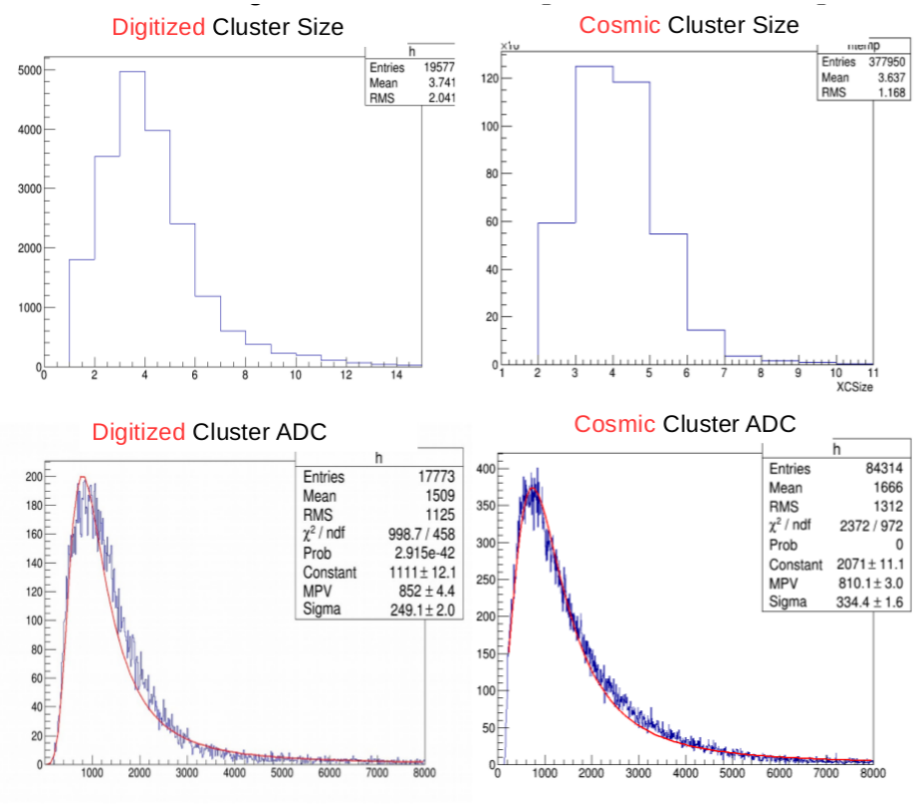

Figure 5-3: Cluster size and amplitude of digitized elastic electron hits and real cosmic hits

5.3 Analysis

One of the two major challenges in the data analysis of the SBS experiments comes from the high level of accidental background hits in the GEM detector. For example, in the GMn experiment, the average number of non-trigger-correlated hits in one layer of GEM detector is 200 along with one single hit of interest. In such situations, discriminating these random background hits from trigger correlated hits is essential to accurately reconstruct tracks of interest from the detector set. The track reconstruction efficiency and accuracy play a very important role in the final accuracy of the nucleon form factors extracted from the experiment. In this chapter, we will first briefly describe the Hall A analyzer framework that the GEM analysis is built into and then discuss the GEM data analysis procedures and techniques that are newly designed and developed to handle the high random background hit rates. The fully digitized simulated data for the GMn experiment will be used to demonstrate

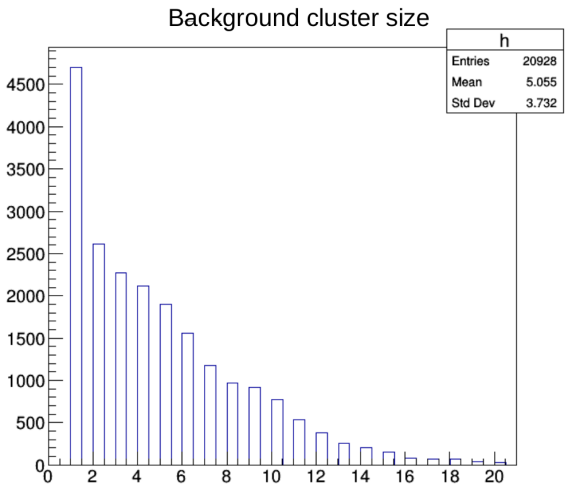

Figure 5-4: Cluster size of background hits after digitization. As can be seen in the plot, most of the background hits have a large cluster size

and test the analysis procedures. The analysis of the GEM related data consists of four parts: decoding the raw data, GEM hit reconstruction, track reconstruction and finally interaction vertex reconstruction. At the end of this chapter, the track reconstruction efficiency and reconstructed interaction vertex variable accuracy are presented to show the effectiveness of the current GEM analysis procedure in dealing with the high level of backgrounds.

5.3.1 Hall A analyzer

The Hall A analyzer is an object-oriented, highly modular and extensible framework built on top of ROOT. The framework provides three major types of base class: Apparatuses, Detectors, and Physics Modules. These type of classes are processed automatically in the core package of the Hall A analyzer in order. For a given new experiment, only new classes need to be derived from these base classes to include new features and they will be scheduled in the run accordingly without the need of writing the core process. The analyzer replay flow chart is shown in Figure 5-5. Real raw data files or digitized simulation data files are fed into the analyzer. They are handled differently by its own specialized decoder. The analysis stage consists of three major parts: detector decoding, reconstruction and physics calculation.

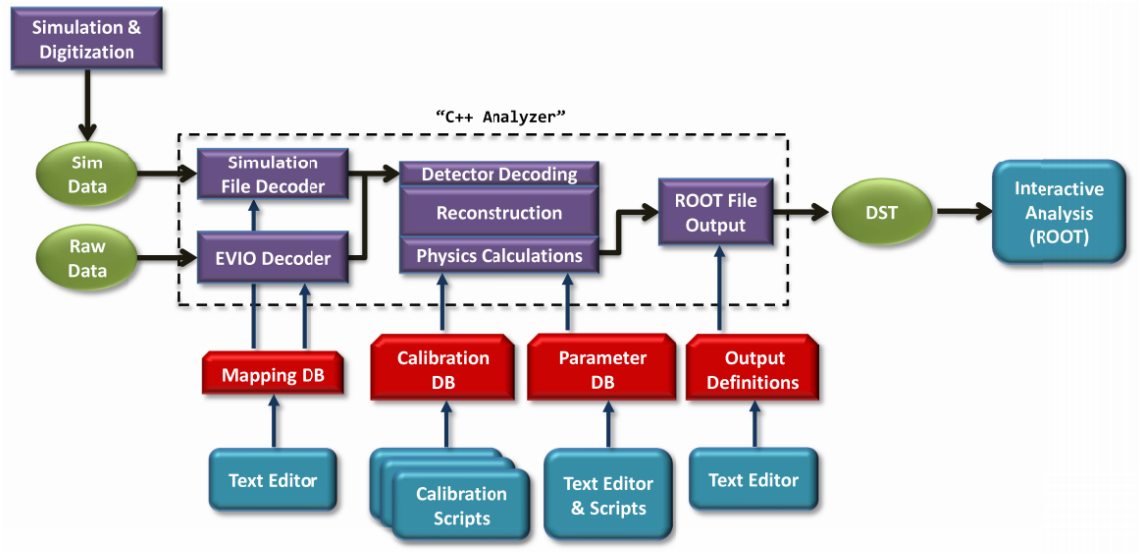

Figure 5-5: Physics replay components of Hall A analyzer. Figure from Hall A analyzer group.

5.3.2 Decode

The raw data file recorded by the CODA DAQ system is in the format of EVIO. Each EVIO file consists of one or several containers called "banks". A bank contains major data types or other child banks. In the case of the SBS experiments, the raw data file will contain multiple banks, each of which holds the data from a different detector group. In the GEM detector bank, the data start with the SSP block header, event header and trigger time that contains information like the slot ID, number of events, number of blocks, number of words in this block and trigger number. The MPD section is wrapped within the SSP block and starts with MPD block header, clock phase, and APV header followed by hit information on each readout strip. The Hall A analyzer decoder class decodes the raw data and converts to physical signal information on detector readout strips for further analysis.

In the case of analyzing digitized data from simulation, the data will first be transformed into the same format of real data and then go through the same procedure as real data. Since the data are from simulation, additional true information like true track information, energy deposition of a hit needs to be recorded for later

evaluation of the analysis. A newly developed "SBSSimDecoder" class takes care of theis information and stores it for later usage. This true information is never used in any aspect in the analysis process and solely used to evaluate the analysis results.

5.3.3 Hit Reconstruction

In the GMn experiment, the average random background hit rate is about 100 kHz/cm^2. For each hit of interest, the number of background hits detected within the 325 ns effective readout window is roughly 100 on every GEM module of size 60x50 cm^2. The chance for a hit of interest to overlap with background hits is very high as shown in Figure 5-6. Thus the analysis needs not just be able to reconstruct hits from strip information, but more importantly be able to disentangle overlapping hits as much as possible to minimize the influence of random background hits on hits of interest. Background hits are generally both larger in size and amplitude. If a hit of interest overlaps with background hits and is not separated from the background hit well enough, the position and timing of the hit could be severely distorted as shown in Figure 5-7. This results in the decrease of the detector efficiency when misidentified as an background hit and the decrease of the accuracy of the hit position reconstructed. A set of hit reconstruction procedures is designed to address this issue. They are described in detail in this section and their results are shown at the end of this section in terms of how much background they suppress and how well they disentangle the hit of interest from background hits.

Common mode subtraction

Common mode subtraction is the very first step when treating any GEM data taken with APV-25 cards. It is necessary because all of the 128 channels in one APV-25 card fluctuate up and down by the same amount from event to event and time sample to time sample as shown in Figure 5-8. This fluctuation shouldn't be treated as electronic noise since it can be corrected by measuring the group shift of all channels. The group shift is referred as "common mode" and the correction is referred

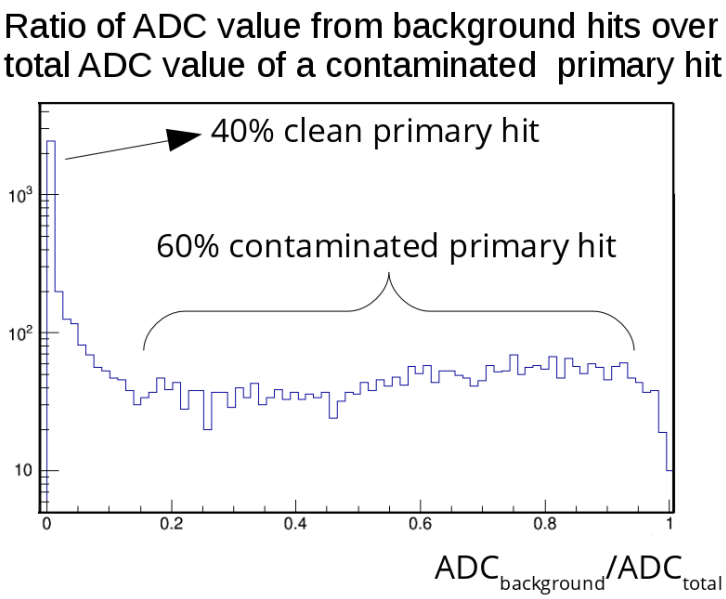

Figure 5-6: Ratio of ADC value from background hits over total ADC value of a contaminated primary hit. 60% of all the primary hits are contaminated to different levels. Some of the primary hits are completely dominated by random background hits.

as "common mode subtraction". If there are no fired channels in the group, the group shift can be measured by just taking the average of all 128 channels in the group. However, when there are fired channels, theses channels need to be removed from the group before taking the average to avoid influencing the accuracy of the estimate of the group shift. At this stage, the baseline of the channels isn't determined, thus it is not possible to identify fired strips using zero suppression based on the electronic noise level. One traditional method of identifying fired strips is first sorting the strips in ascending order by ADC value and checking weather a strip is outside a reasonable range(usually 10 times of the electronic noise) from the average.

In the GMn experiment, the raw data volume is extremely high. As discussed in Chapter 4, online data reduction will be done on SSP. This requires evaluating the common mode in real time. The method discussed above takes O(nlogn) time and O(n) space, neither of which are available on the SSP device due to the huge number of channels to process. For this, a new method of calculating the common mode in real time is developed. This method takes O(n) time and uses constant space on the

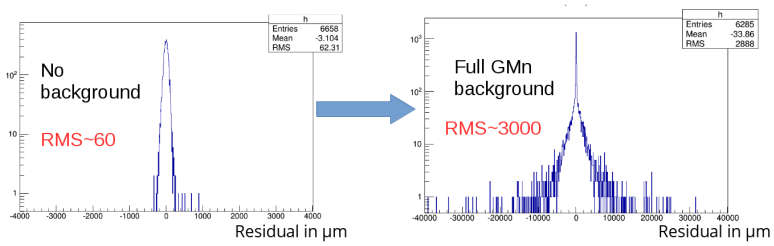

Figure 5-7: Distorted position resolution. The left plot is the position resolution without background. The right plot shows the greatly decreased position resolution under full GMn background when there is no separating mechanism between primary hit and background hits.

SSP. The memory on SSP is extremely tight as each one of them needs to process data from multiple MPDs. In the new method, first a range of possible common modes for a certain APV-25 card is determined by examining the distribution of the baseline in pedestal runs. During real time processing of high occupancy data, an average of all the channels that are within this range is calculated. Then channels that have an ADC value more than 10 times the pedestal noise sigma larger than the first average are excluded from the set before calculating a new average of the new set of channels. After 3 iterations, the final average is used as the common mode. In this thesis, the new method is adopted.

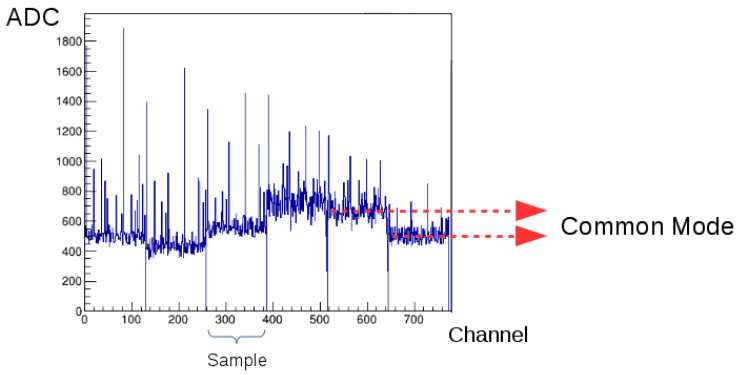

Figure 5-8: Fluctuation of common mode movement of 128 channels.

Pedestal

As the first part of the analysis procedure, pedestal analysis needs to be done with dedicated pedestal runs. In a pedestal run, beam is turned off. The data are taken with artificial high rate triggers. There will be no hits in the GEM detectors except on very rare occasions when a cosmic ray passes through. Cosmic rate will be negligible compared to the artificial trigger. The pedestal analysis aims to measure the electronic noise level of each channel and use it to determine whether a channel is fired in further analysis of experimental data. In the GMn experiment, GEM detectors are read out by APV-25 cards. Each APV-25 card provides 128 channels to amplify signals from 128 readout strips. It is observed that each of these channels has different level of electronic noise and each has its own baseline level compared to others. For every strip, after the common mode subtraction, the average ADC of all time samples recorded is calculated and accumulated over all events in the pedestal data. The electronic noise level for each strip can be retrieved by taking the rms value of the averaged ADC distribution of that strip. The baseline level can be retrieved by taking the average. The pedestal result of 128 channels on one of the APV-25 cards is shown in Figure 5-9. The pedestal results can also be used to identify broken or hot channels in the readout. Pedestal runs needs to be taken regularly given that the pedestal results could change during the experiment especially when environmental conditions change.

Zero suppression

Zero suppression is a routine after common mode subtraction to identify fired strips using pedestal results from pedestal runs. An average ADC of all time samples is calculated for each channel. The channel's pedestal offset is subtracted from the average ADC. The result is compared to an empirical threshold of 5 times of this channel's pedestal noise rms. If it is above the threshold, this channel is considered to have fired. Channels with an ADC value below the threshold is considered as idle and removed from future analysis.

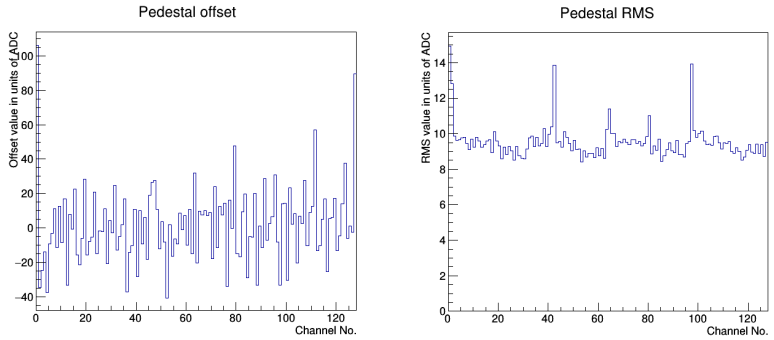

Figure 5-9: The pedestal data of one APV that has 128 channels. The left plot shows the offsets among the 128 channels. The right plot shows the rms value of the pedestal noise. It reflects the quality of a specific channel. A slightly higher noise level is common and acceptable since the average signal size is around 700 ADC, which is much higher than the noise level.

Cross talk removal

Cross talk is a phenomena that happens on the APV-25 cards. When a channel has a large signal, adjacent channels(the one before or after) will have a small signal which is usually about 10% of the large signal. The main reason of this "cross talk" behavior is because the phase offset between the APV-25 clock and the MPD's clock. The 128 channels on one APV-25 cards are packaged and output in a pipeline with 40 MHz clock. When this clock is not perfectly synchronized with the MPD clock, a signal on one channel can blend into the other like shown in Figure 5-10. This issue is extremely critical when there are considerable amounts of background hits along the signal hit since it can potentially double the amount of non-signal hits. A correction can be made to remove the cross talk channel based on two facts. First, the ratio between the original signal and cross talk signal is stable. Second, the adjacent channels on the APV-25 cards aren't adjacent physically and there is a fixed relation. In the cross talk correction, the ADC of the "adjacent" channel of a fired channel is checked. If the signal is below a threshold, for instance, 10% of the original signal, then this channel is discarded. This method is very effective when number of background hits is not extremely high. In the case of high occupancy still effectively removes cross talk channels. But it will have higher chance of eliminating the signal of interest, leading to lower detection efficiency. In order to increase tracking efficiency

in the GMn analysis, this routine is not included because ghost background hits are well rejected by cuts at other levels.

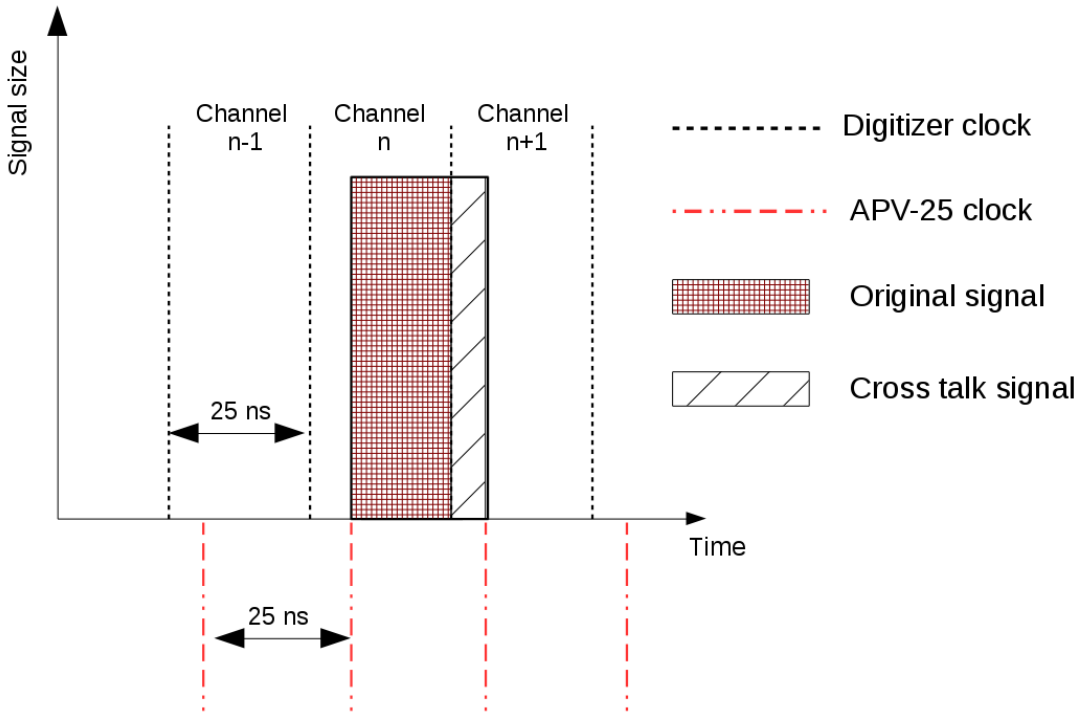

Figure 5-10: Cross talk and phase offset between the digitizer clock and APV-25 clock. In the case above there is a shift between the APV-25 clock and digitizer clock. As a result, the original signal is split into channel n and channel n+1. This makes one original large signal appears as one large signal accompanied by another small image of the large signal.

Extract timing information of a signal

In the GMn experiment, each channel of the GEM detector is sampled six times with interval of 25 ns once a trigger is issued. The evolution of a channel's ADC value can be used to extract the timing of the signal relative to the trigger. This timing information provides a simple and reliable way to reject random background hits since they are unrelated to the trigger. The resolution of the timing information then becomes critical in how well can it be used to reject backgrounds. The extraction of a signal's timing and methods to improve the timing resolution are discussed below.

The original signal from induction on the readout strips is amplified by the APV-25 chip and goes through a shaper that outputs a certain pulse shape. The signal timing is acquired by fitting the 6 sampled data points to the pulse shape using maximum likelihood estimation. An empirical function is used to describe the pulse:

$$f(t) = A(t - t_0)e^{-\frac{t-t_0}{t_s}} \tag{5.1}$$

Where A is the normalization factor, t_0 is the start time and the t_s is the shaping time which characterize how fast the pulse shape evolves. An example of sampled data points and its fitting curve is shown in Figure 5-11.

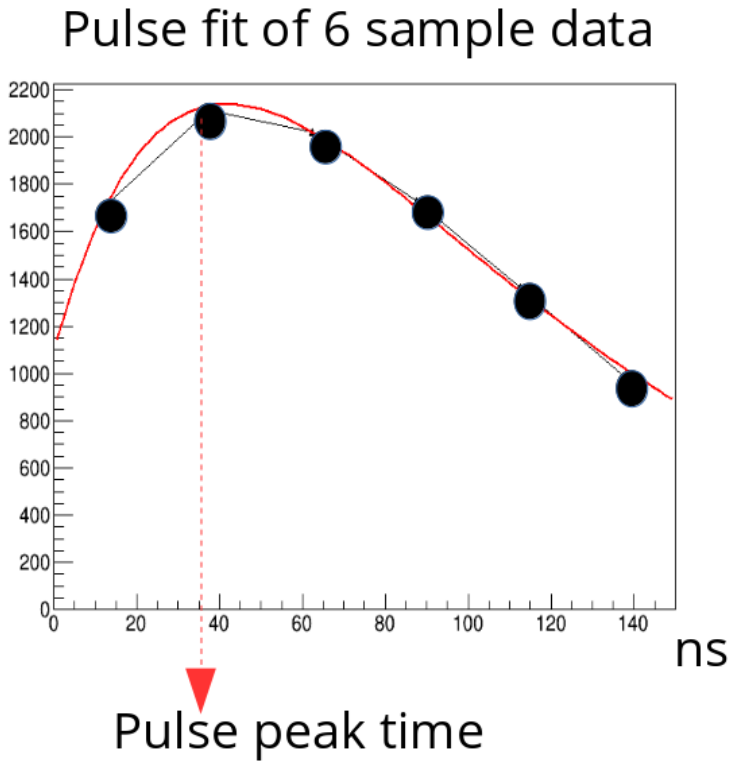

Figure 5-11: Sampled data points and the fitting result from one event in the data. A clean hit without any overlapping hit is selected here just to show the performance of the fitting

As discussed in Chapter 4, additional timing corrections need to be carefully treated to achieve good timing resolution. One is the correction for the random phase of the trigger within the APV-25 clock and the other is correction for the

minor non-uniformity across the whole GEM module. The effectiveness has been tested and verified in the GEM test run in Hall A at JLab as described in Chapter4. In the digitized simulation data, the uncertainty of these corrections are factored into the uncertainty of the trigger time.

A first-level rough rejection of fired strips from background hits is executed based on the results of the timing fit. If the peak time of the signal on a strip is less than zero or larger than 150 ns, this strip is discarded. In the online data reduction on the SSP, another similar cut can be performed by requiring that the highest sampled ADC value is neither in the first sample nor the last sample. This way the total data volume after the SSP is reduced by another factor of 2.

Clustering

Clustering is a stage where individual fired strips are identified as originating from same cluster and grouped as a hit cluster. As discussed above in the beginning of this section, the probability for the primary hit to overlap with a random background hit is very high. 60% of all the primary hits overlap with background to certain extent. Without special treatment, the reconstructed primary hit is severely polluted and gives extremely bad efficiency and accuracy. A new cluster reconstruction analysis is designed to minimize the influence of the background hits to primary hits.

A comprehensive method is searching for clusters using a 3D diagram with the position of the strip being x axis, the time sample number being y axis and the ADC of that strip in that time sample being the z axis. This method searches for local maximum of the ADC value to determine the number of clusters. In th event of overlapping clusters, the ADC of a strip is split by the ratio of expected ADC values of clusters calculated based on its maximum and the location of the maximum. In principle, this method can highly disentangle overlapped clusters. However, due to the limitation of data acquisition electronics in SBS experiments, the electronic noise is high and local maximum is usually hard to define. This is because the relative large interval between time samples and the limit on the total number of samples. In a experiment where DAQ electronics suffice, this method provides best separation of

overlapped clusters.

In the actual analysis of digitized simulation data of GMn experiment, another similar method that utilizes information both in position and time is designed and used. In this method, the analysis looks at only the position of strips and uses the timing result of strips as criteria to separate clusters in addition to local maximum of ADC in the position of strips. When a new strip is examined, if its timing information is far away from the previous strips, then this strip is considered to be in a "shared strips" category. The "shared strips" are split into two parts when a new set of strips well grouped in time is found. The split ratio is based on the ratio of the maximum ADC value in the two clusters. A new cluster timing is extracted by fitting the ADC sum of all strips in the cluster at each time sample. A second-level timing cut of 30~90 ns is applied to all clusters to reject clusters from random background hits. Figure 5-12 shows the improvement in efficiency of reconstructed primary hits using the new analysis compared to analysis without effort in splitting overlapping hits and an analysis that uses only position information to split. At the end of the clustering routine, 85% of original primary hits are reconstructed and remain "accurate"(with residual within 500 μm) enough to form good tracks. The position and timing resolutions of the reconstructed hits are shown in Figure 5-13. In the condition with the highest level of background in GMn experiment, 85% of all the reconstructed hits have a reconstructed position deviating from their true position by less than 500 μm. 91% of the reconstructed hits have their reconstructed peak time within the timing cut of 30 ns to 90 ns. For the no background condition, 99% of hits have a good reconstructed position and reconstructed timing parameter. The result showed that the cluster splitting method not only increased the hit reconstruction efficiency, but also the accuracy. Along with the primary hit, there are also on average 50 hits that are indistinguishable from the primary hit on each tracking plane. Figure 5-14 shows the distribution of the number of indistinguishable background clusters per event per plane up to this stage of the analysis. These background hits are fed into the track reconstruction stage of the analysis along with the primary hit.

Percentage of primary hit still available(not cut off)

	No background	Full GMN background (~200 hits)		
		No split	Split in space	Split in space and time
Pass time cut (30~90ns)	99%	79% →	85% →	91%
Pass time cut and form good track (residual within 500 um)	99%	62% →	79% →	85%

Figure 5-12: Comparison of different clustering methods. The improvement from 60% to 85% corresponds to drastically different tracking efficiency

5.3.4 Track Reconstruction

Once clusters are reconstructed from information on strips and coarse background rejection based on timing information is done, the next step is to reconstruct tracks from these candidate clusters. The task is to reconstruct and identify the track of the scattered electrons from hit clusters on the 5 tracking planes with the influence of on average 50 random background hits per tracking plane. The final goal of this stage is to reconstruct and identify the one primary track out of all false tracks formed from background hits. In this section we will describe the track reconstruction and multiple background rejection routines.

TreeSearch Tracking Algorithm

TreeSearch in the Hall A analyzer framework is a fast straight track reconstruction algorithm based on pattern matching. The algorithm divides tracking planes into bins and pre-calculates and stores possible bin patterns that a straight track can leave in the tracking planes. When analyzing actual events, the algorithm compares the pattern of the analyzed event with pre-calculated patterns and checks whether there is a match. The set of hits within the matched patterns then becomes a track candidate. This process is repeated for multiple iterations. In the beginning the whole tracking plane is considered as one bin and the number of bins increases by a factor of 2 for each deeper level iteration. Figure 5-15 shows an example of the base method. In the analysis of the GMn digitized simulation data, the number of iterations is determined as 12 in vertical axis and 10 in horizontal axis so that the

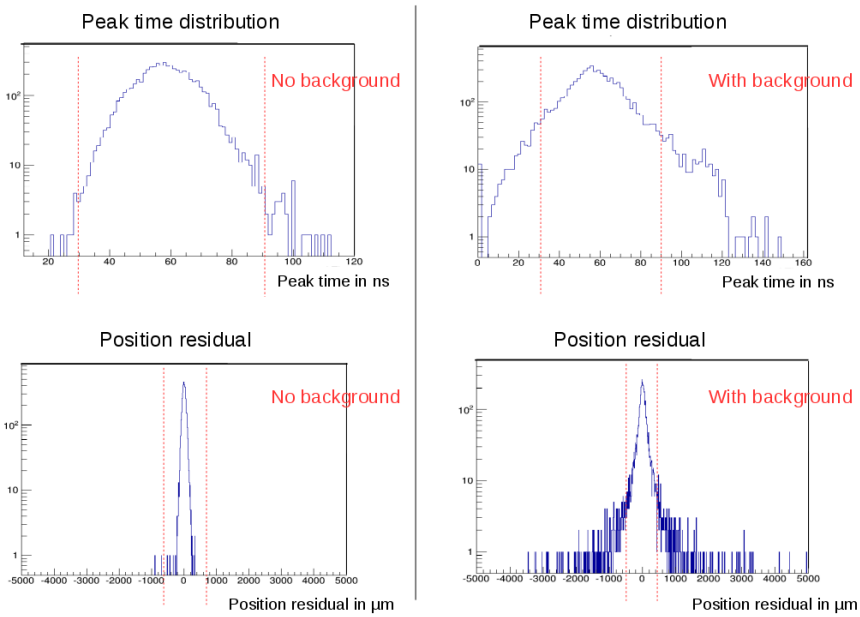

Figure 5-13: Position residual and timing performance of reconstructed primary hits. Plots on the left side are results from data without any background. Plots on the right side are results from data with the highest level of background in GMn experiment. The red dashed lines show the cut on the peak time and the position of the reconstructed hits as a method of evaluating the percentage of hits reconstructed with good accuracy.

minimum bin width is 500 μm in vertical axis and 600 μm in horizontal axis. The different setting between the two axes is due to the different plane sizes, with one being 2 m and the other being 0.6 m. The goal of the setting is to have the minimum bin size a few times larger than the average resolution of a GEM detector which is around 100 μm. This way the algorithm will not count different tracks close to each other as one due to too large search bin size, neither will it miss any good tracks due to a search bin size that is too small. The advantage of this algorithm is that it is very fast by identifying track candidate using pattern matching instead of fitting all possible combinations of hits.

2D Track forming and background rejection

Three type of cuts are applied to reject false tracks from background hits:

Module order cut. The TreeSearch algorithm outputs a collection of "roads"

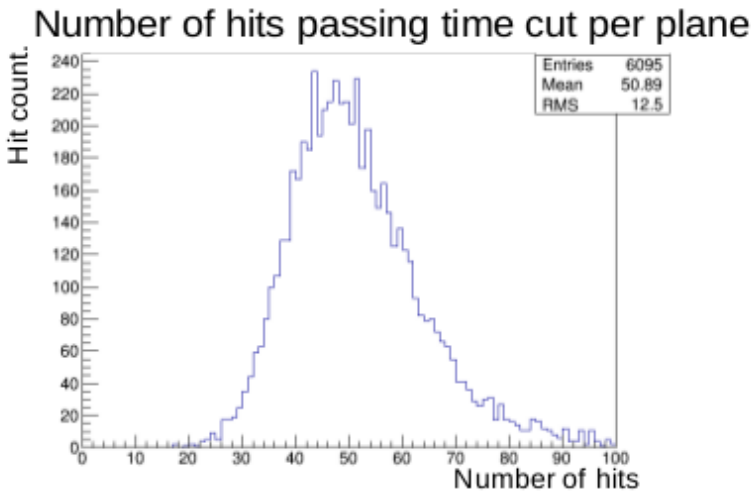

Figure 5-14: Number of background clusters indistinguishable from primary hit per plane

for both vertical and horizontal axes. The "road" consists of a set of lighted bins that form a straight line in the detector. The GEM hits within these bins will be analyzed and used to reconstruct tracks. From now on, the vertical axis will be noted as the X axis, the horizontal axis as the Y axis and the axis orthogonal to both X and Y as the Z axis. After the pattern matching step, there are on average 40 candidate tracks in the X-Z plane and 140 candidate tracks in the Y-Z plane. The drastic difference between the two planes is explained as follows: multiple GEM modules are placed side by side along the X axis to make up a full tracking plane and information on modules of the same plane is summed together. In this way, hits from multiple modules stack in the same range in the Y axis but scatter to different part of the the X axis. So hits in the Y axis is denser than hits in the X axis, which make the number of candidate tracks in the Y-Z plane much more than the X-Z plane. It is necessary to sum information on modules and do tracking at the plane level since there could be tracks that passes through modules with a different module order. However, this will include additional fake tracks in the Y-Z plane as shown in Figure 5-16. These fake tracks are rejected by a step that checks the order of the modules in the track. A set of possible orders of module IDs is pre-computed and used to check whether a track has reasonable order of module IDs. Figure 5-16 shows an example of module

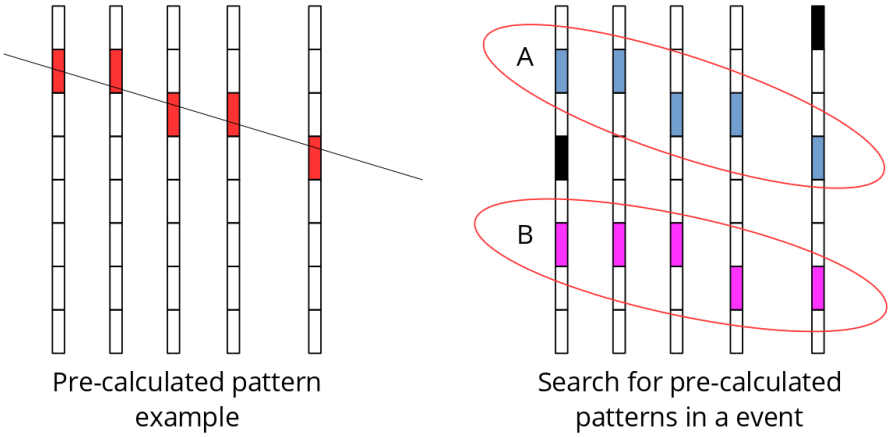

Figure 5-15: TreeSearch algorithm. The left figure shows an example of a pre-calculated hit pattern in the five tracking planes. The right figure shows an example of the tracking process. In this case, there are two tracks reconstructed. Track A is from a pattern that consists of 5 blue hits. Track B is from pattern that consists of 5 magenta hits. The black hits represents random background and noise hits.

ID order selection.

Position cut based on Calorimeter hit. The lead glass shower and preshower in the GMn setup function as a electromagnetic calorimeter. By itself, it provides measurements of position and energy of the scattered electron and some degree of particle identification between electron and pion by looking at the amplitude of the signal in preshower. The position of a hit is reconstructed by taking the amplitude weighted sum of the positions of fired blocks. The position resolution is around 1 cm. A primary track is formed by high energy electrons which deposit energy in the calorimeter while a ghost track from random background hits doesn't have a corresponding calorimeter hit. Thus the position of the reconstructed hit in the calorimeter provides an expected projected position of the primary track. The analysis requires a track's projection point on the calorimeter plane to be less than 10 times the calorimeter position resolution away from its closest calorimeter hit for it to be considered as a good track. The position resolution of the calorimeter and the residual of reconstructed tracks' projected position on the calorimeter plane are shown in Figure 5-17. This position cut based on calorimeter hits reduces the number of false

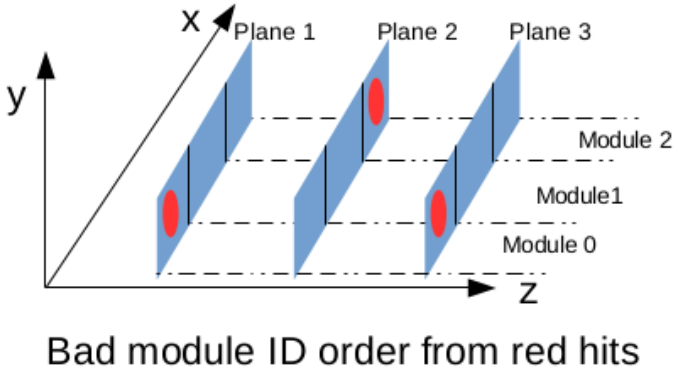

Figure 5-16: The false tracks that can be rejected by module order selection. A false track in the Y-Z tracking plane consists a sets of hits(red dots in the figure) from GEM modules that is impossible to form a straight track in the X-Z tracking plane.

tracks by roughly a factor of 10.

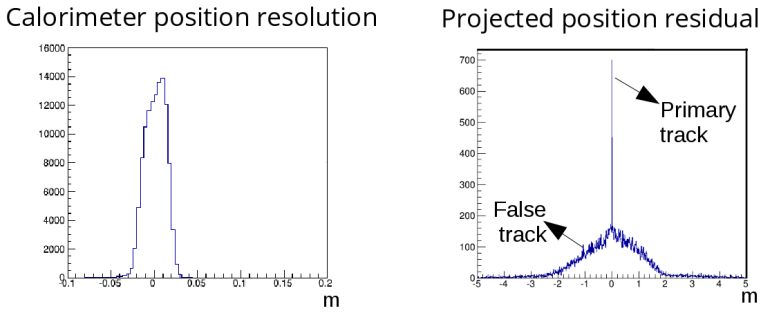

Figure 5-17: Calorimeter resolution and projected position residual of reconstructed tracks. The sharp peak in the center corresponds to projected positions from primary tracks, which indicates a good match between the projected position and the position of the calorimeter hit. An extremely large amount have very bad matches with the calorimeter hit and are thus rejected.

Elastic kinematics cut. For the elastic tracks, there is a strong correlation between the slope and intercept of the track. This is utilized to reject false tracks from random background hits and inelastic tracks. The correlation and the actual cut applied on candidate tracks is shown in Figure 5-18

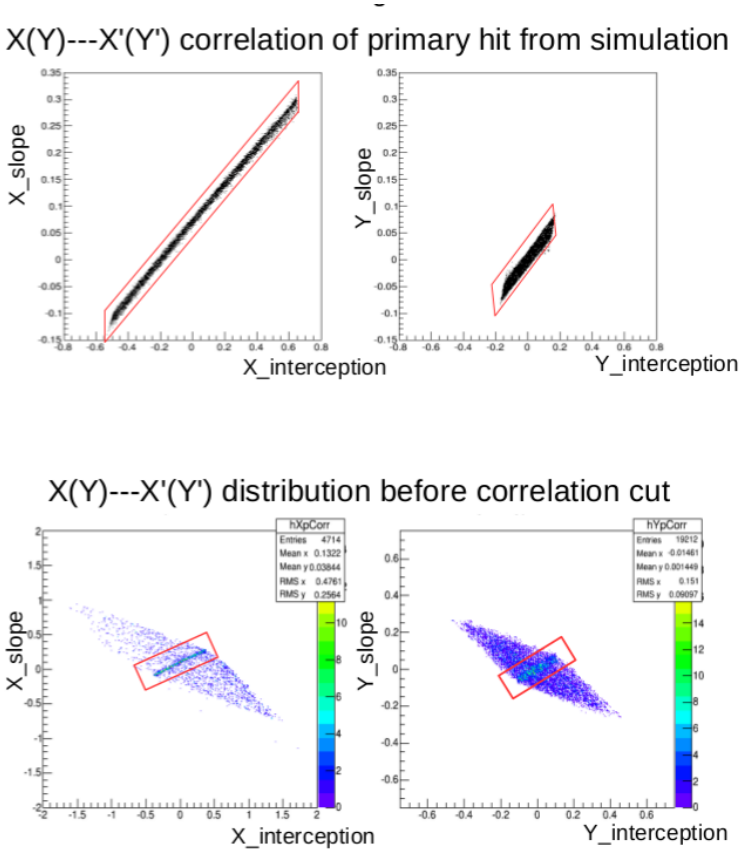

Figure 5-18: The top plot shows the correlation between the slope and intercept of simulated elastic tracks. The red rectangle in the bottom plot shows the cut applied to reconstructed candidate tracks.

3D Track forming and background rejection

Up to this stage, we have reconstructed 2D tracks and cleaned up background hits as much as possible. The horizontal and vertical tracking planes are treated separately in the above analysis. In the next step we match tracks in the two tracking planes together to form a 3D track. In this process, there will be multiple false matches and only 1 good match should exist since it is rare for two false tracks from two tracking planes to have a good match. Additional cuts are applied to reject 3D tracks from backgrounds. These cuts mainly use the hit information from different tracking layers and are applied step by step to eliminate false track matching pairs from backgrounds. These cuts are described as follows:

- **Cuts based on module ID** Each GEM layer consists of either 3 or 4 indi-

vidual GEM modules in the GMn experiment. Each hit within a track has its associated module ID indicating which module the hit comes from. For a 2D track pair to be "good", the module ID of hits on the same plane has to be the same since a good hit pair has to come from same GEM module.

- **Cuts based on hit amplitude** The readout board of the SBS GEM detector is designed so that the signal amplitudes in the two axes are roughly the same as discussed in Chapter 4. Thus on the same GEM layer, hits are required to have similar amplitudes for two tracks to match with:

$$\frac{ADC_x - ADC_y}{2(ADC_x + ADC_y)} < \epsilon \tag{5.2}$$

  where ADC_x is the ADC value of the hit in x axis, ADC_y is the ADC value of the hit in y axis and ϵ is the maximum asymmetry allowed which is determined by the characteristics of each GEM module. For the case of the SBS GEM detectors ϵ is set as 0.3.

- **Cuts based on timing** Aside from good amplitude correlation, the SBS GEM detector also has good signal timing correlation between the two readout axes. As discussed in Chapter 4, the timing correlation can be as good as 6 ns in low occupancy conditions. Thus on the same GEM layer, hits can be required to have similar timing for two tracks to match. However, due to the high occupancy levels in the GMn experiment, the primary hit's timing is distorted greatly by background hits which makes the timing resolution much worse. This leads to an efficiency drop when a tight cut on timing is applied like for the low occupancy case. In the actual analysis this cut is not included since backgrounds are already well cleaned up and the cut only decreases tracking efficiency. In future experiments where more backgrounds are present, this cut helps reduces the mismatching of tracks. The tightness of the cut needs to be carefully evaluated to maintain good tracking efficiency.

Tracking result

Due to the open configuration of the GMn experiment, the random background level is extremely high in the GEM trackers. Rejecting these random background hits is the most crucial part to reconstruct clean and accurate elastic electron tracks. As a starting point we have around 100 hits per tracking layer accompanying the single elastic electron hit. After various cuts on the hit level and track reconstruction, there are tens of 2D tracks on each tracking plane. These candidate tracks are cleaned up step by step by methods described above. The number of candidate tracks throughout the analysis is shown in Figure 5-19. As the final step of the track reconstruction, the track with the best fitting results is selected among the on average 1.2 tracks left. The position resolution of the final track is shown in Figure 5-20.

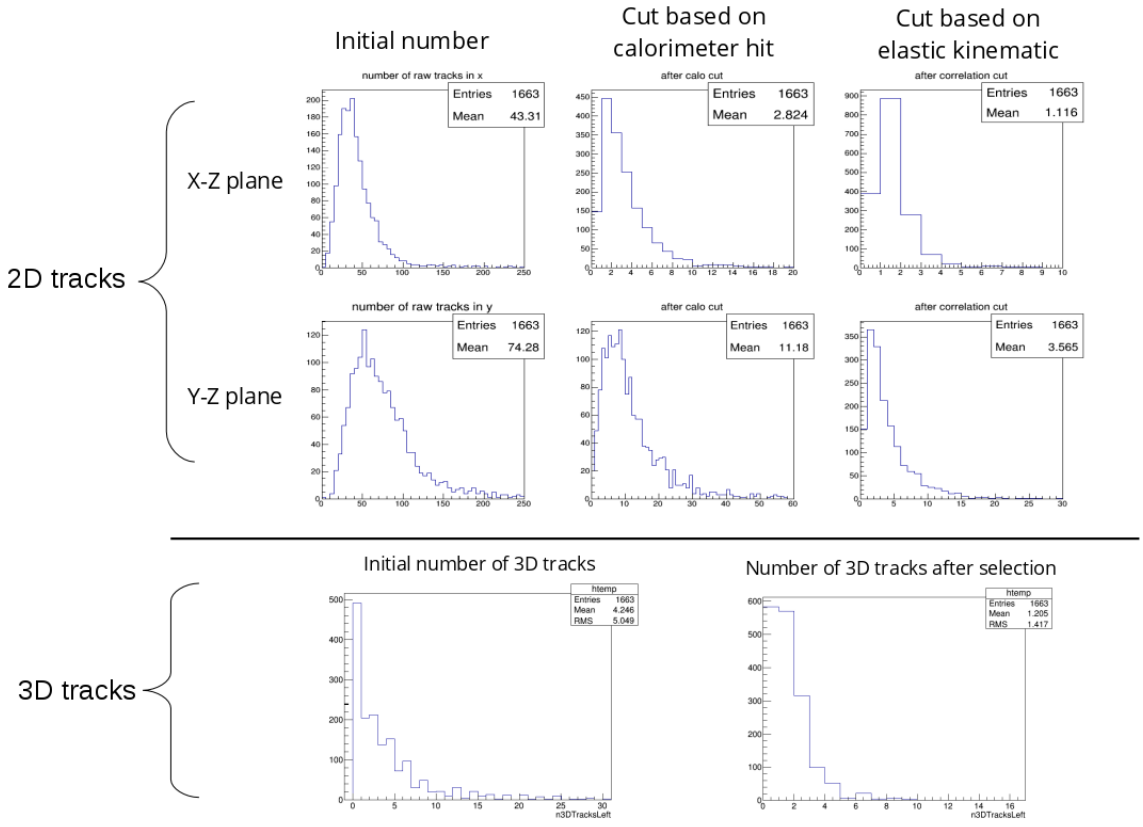

Figure 5-19: The number of tracks throughout the tracking analysis. It is worth noting that in the 2D tracking stage, the initial number of tracks for the Y-Z plane will be about 2 times more than shown on plot if the module order selection in the track finding stage is absent.

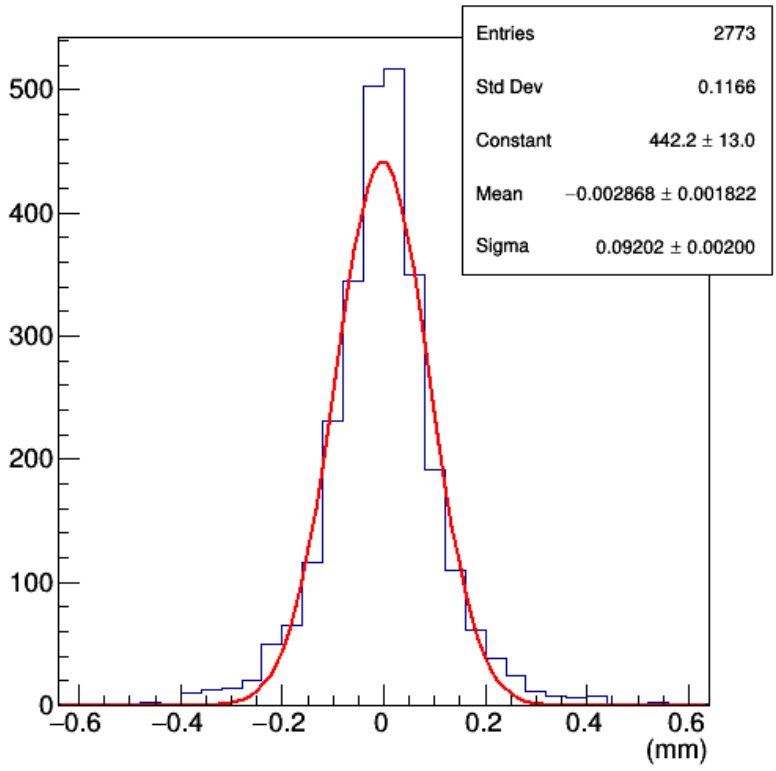

Figure 5-20: The position residual of the final selected primary track. The rms value is around 90 μm, which is a very good result given the intrinsic GEM position resolution of 70 μm for perpendicular tracks.

5.3.5 Interaction vertex variable reconstruction

Once the final track at the detector side is obtained, it is then transformed back to the target to reconstruct the information of the interaction vertex through a set of optic matrix elements. Before going further, it is useful to describe the three coordinate systems involved. The first one is the global coordinate system. The X axis is horizontal to beam left. The Y axis is vertically up. And the Z axis is in the beam direction. The second one is the transport coordinate system. The X axis is along the dispersive direction and in the direction of increasing momentum (vertically down). The Z axis is horizontal in the direction of the BigBite spectrometer forming an angle of θ_0 (the placement angle of the BigBite spectrometer) with the beam. The Y axis is along the non-dispersive direction such that XYZ forms an right-handed Cartesian coordinate system. The third coordinate system is the local

spectrometer coordinate which can be obtained when the Z axis of the transport coordinate is rotated upward by 10° around its X axis. The goal is to transform the tracking information in the local spectrometer coordinate back to interaction vertex information before the BigBite magnet. The formalism used is:

$$\begin{bmatrix} x'_{tar} \\ y'_{tar} \\ y_{tar} \\ p\theta_{bend} \end{bmatrix} = \sum_{i,j,k,l,m=0}^{i+j+k+l+m\leq n} \begin{bmatrix} C_{ijklm}^{x'_{tar}} \\ C_{ijklm}^{y'_{tar}} \\ C_{ijklm}^{y_{tar}} \\ C_{ijklm}^{p\theta} \end{bmatrix} x^i y^j x'^k y'^l x_{tar}^m \tag{5.3}$$

where x, y, x', and y' are the position and slope of the track after the BigBite magnet in the local spectrometer coordinate system, x_{tar}, y_{tar}, x'_{tar}, y'_{tar} are interaction vertex variables in the transport coordinate system, and the $p\theta_{bend}$ is the product of the momentum of the scattered electron and the trajectory bend angle in the magnet. The matrix is obtained by fitting on the relation between spectrometer tracking information and interaction vertex variables in simulated events. The reason x_{tar} is included in the expansion is because the problem of reconstructing five track parameters at the target (x', y', x, y, p) from four measured track parameters at the spectrometer (x, y, x', y') is under-determined. Or in other words, one can't solve four equations for five unknowns without bringing in extra constraints. That is why we fix x_{tar} on each iteration of the reconstruction using the best available information. Fortunately, the vertical bend mostly decouples the measurement of the momentum and the out-of-plane angle from the measurement of the vertex coordinate and the in-plane angle. The x_{tar} can be initially set to 0 and reconstructed in this iterative process, which converges fairly rapidly. A second order fit of the matrix with six iterations was used in the analysis and achieves good resolution. The fitting result can be found in Appendix A. A comparison of true interaction vertex variables with interaction vertex variables reconstructed using true track information in the BigBite was used to benchmark the performance of the fitting results of the optic matrix as shown in Figure 5-21.

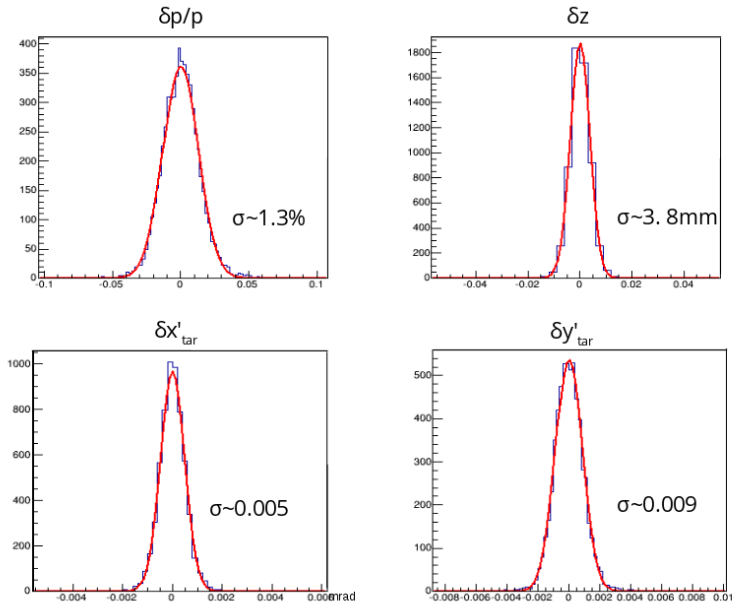

Figure 5-21: Comparison of true interaction vertex variables with reconstructed interaction vertex variables using true track information. The top left plot is momentum difference in percentage. The top right plot is difference in z location of interaction vertex in global coordinates. The bottom left and bottom right plots are respectively the difference in X and Y intercepts in the transport coordinate system.

5.3.6 Results

Tracking accuracy under background expected in GMn

The optic matrix is then used for the reconstructed track from actual analysis to reconstruct interaction vertex variable. The result is compared to true interaction vertex information. The accuracy of the reconstruction for data without background and with full background expected in GMn experiment are shown respectively in Figure 5-22 and Figure 5-23.

In the case of no accidental background, the final tracking efficiency is 90% with good accuracy. The final tracking efficiency is defined as the ratio of the final number events that have the primary track reconstructed over the total number of events. The relatively low tracking efficiency is due to two intended settings:

1). The gain of the GEM chamber during the digitization step is intentionally set to be lower than the normal operating gain of the GEM. At this gain setting the

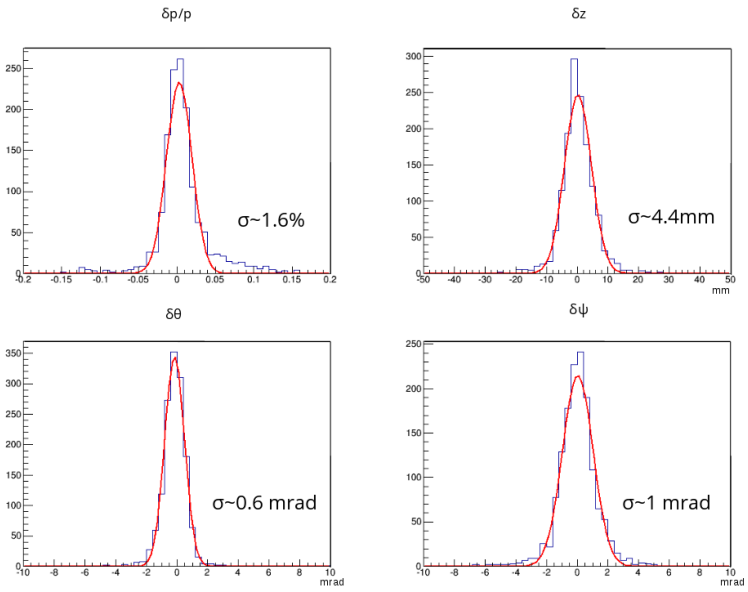

Figure 5-22: No background case. Comparison of true interaction vertex variables with reconstructed interaction vertex variables using selected track from analysis of digitized data. The top left plot is momentum difference in percentage. The top right plot is difference in z location of interaction vertex in global coordinates. The bottom left and bottom right plots are respectively the difference in the out-of-plane angle and in-plane angle of scattered electron in transport coordinate system.

detection efficiency of the GEM detector is 93% instead of 97% which can be easily achieved by bumping the high voltage applied to GEM by 50 V. At 93% detection efficiency a tracking reconstruction requiring 4 out of 5 tracking planes has tracking efficiency of 95%, while at 97%, the tracking efficiency is 99%. The reason of this low gain setting is the conservative consideration in two aspects. First because of the high number of hits in the GEM detector during the experiment, the charge deposition into the GEM detector will be considerably high. A lower gain setting will prolong the life of the detector. Thus an investigation of the tracking performance at such low gain setting is beneficial. Second since most of the accidental background hits in the GEM detector come from low energy photons, the signal size of the accidental hits are generally two times larger than that of the scattered electron hit which deposits energy close to a minimum ionizing particle. This makes possible a separation between the primary hits and accidental hits based on signal size. Note that this separation method is not used in the current analysis. This separation method is only possible

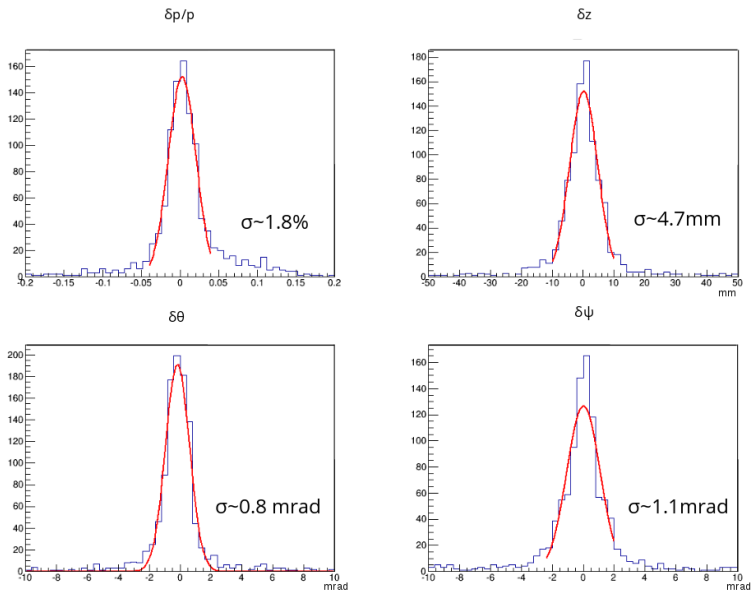

Figure 5-23: Full GMn background case. Comparison of true interaction vertex variables with reconstructed interaction vertex variables using selected track from analysis of digitized data. The top left plot is momentum difference in percentage. The top right plot is difference in z location of interaction vertex in global coordinates. The bottom left and bottom right plots are respectively the difference in the out-of-plane angle and in-plane angle of scattered electron in transport coordinate system.

in relatively low gain setting where the accidental background hit signal saturates the electronics while the primary hit signal does not. The study of tracking performance in a low gain setting is for one reason to evaluate the feasibility of low gain operation of the GEM detector to implement this separation method to further reject background hits.

2). In the analysis, the track selection step tries to select track candidates that originate from the target by looking at the correlation between intercept and slope of the candidate track along the dispersive direction. The cut on this tight and momentum-dependent correlation cuts off 5% of the primary electrons that have higher energy loss before the tracking plane. Thus the tracking efficiency of 90% in the no accidental background case is fully understandable and as expected. It is a result of multiple trade-offs between the considerations as discussed above. In any case, because the goal of this analysis is to investigate how to deal with high levels of accidental backgrounds, the key is to compare the tracking performance between the

no background scenario and the high background scenario. The absolute performance depends on specific gain settings of the GEM detector.

In the case of full GMn background case, the final tracking efficiency dropped by about 21% from 90% to 69% for the no background case. The reconstructed interaction vertex variables are broadened by tiny amount but are still within the requirement of the experiment. The main reason for the drop in tracking efficiency is due to the large amount of background hits. In the highest energy setting in the GMn experiment where the average rate on GEM detector is up to 100 kHz/cm^2, the average number of accidental background hits that accompany the primary electron hit is about 200. In this case, 60% of primary electron hits overlap with accidental background hits and are contaminated to different levels. This contamination could either affect the accuracy of the information of the reconstructed primary electron hit or even fully covers the primary electron hit since background hits are generally much larger. In fact, if there is no special treatment to this issue, it will decrease hit reconstruction efficiency in each plane from 93% (the GEM intrinsic efficiency at a relatively low gain setting) to 57%. This will lead to a very low tracking efficiency of about 10%. With the new analysis method, the hit reconstruction efficiency is about 80% in the highest energy setting in the GMn experiment with the highest level of background. This hit reconstruction efficiency of 80% in principle leads to a tracking efficiency of 74%. However, not all of the reconstructed hits are primary hits. On each tracking plane, the hit caused by the electron is accompanied by 50 background hits that are not identifiable before the tracking stage. To avoid huge amounts of false tracks, a special tracking analysis is implemented as discussed in earlier sections in this chapter. Eventually the primary track is reconstructed and identified with the required accuracy under the experimental condition with the highest background level in the GMn experiment.

Tracking efficiency under various background level

To gain a comprehensive understanding of the experimental condition in the GMn experiments, a scan was done on the background level in the experiment. The relation

between the average occupancy in the GEM detector and the background level as a percentage of the highest background level (which happens with the highest beam energy kinematic setting) is shown in Figure 5-24. The raw occupancy ranges from 13% at 50% of the full GMn background to 45% at 200% of the full GMn background. The final occupancy after background hit rejection ranges from 5% at 50% of the full GMn background to 17% at 200% of the full GMn background. A similar study for the tracking efficiency is shown in Figure 5-25. At 50% of the full GMn background, the tracking efficiency is around 83%. It drops fast to 73% at 75% of the full GMn background. After that it decreases almost linearly to 57% at 200% of the full GMn background. The drop is due to the increasing occupancy with background rate. At higher occupancy, a larger percentage of the primary hits overlap with accidental background hits and get contaminated. Aside from decreasing the tracking efficiency, this effect also decreases the accuracy of the reconstructed tracks.

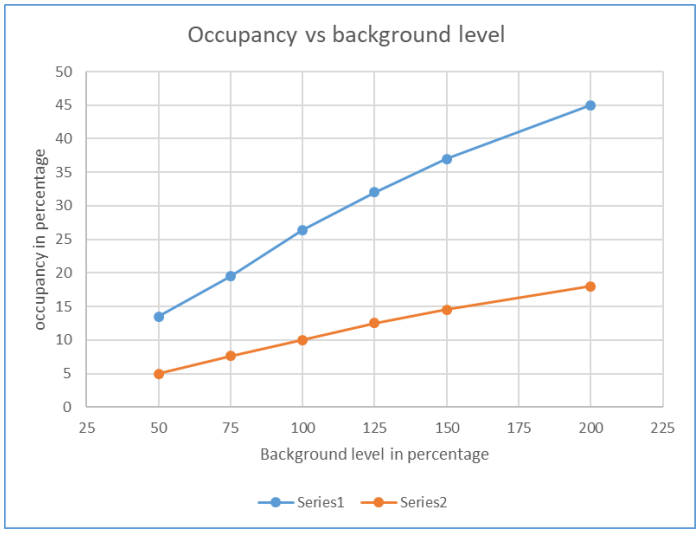

Figure 5-24: The relation between the average occupancy in the GEM detector and the background level. The background level is expressed as a percentage of the highest background level in the GMn experiment in the current run plan. The series1 (blue solid dots) stands for the raw occupancy and the series2 (red solid dots) stands for occupancy level after background rejection in the hit reconstruction stage.

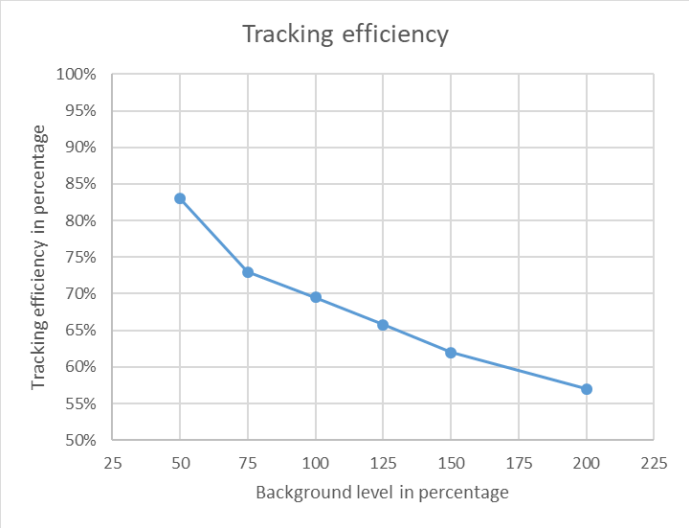

Figure 5-25: The relation between the tracking efficiency and the background level expressed as a percentage of the highest background level in the GMn experiment in current run plan.

5.4 Conclusion

To measure the nucleon form factors at large Q^2, the SBS experiments adopted an open configuration of the spectrometer. This leads to unprecedented levels extremely high rate background conditions at the location of the tracking detectors. While the newly developed and highly optimized GEM trackers are able to operate under these harsh conditions, the high background rates also make the tasks of data collection and transfer to storage media, as well as correctly reconstructing the primary track from among the background hits, extremely challenging.

We took the GMn experiment, the first experiment in the SBS program, as an example case to demonstrate a high background capable analysis (the GEn-II and the GEn-RP experiments have similar background rate level as the GMn experiment). In the GMn experiment, the background rate in the GEM tracker is up to 100 kHz/cm^2. At this background rate, the raw occupancy in the GEM detector is around 25%. Without special treatment, the tracking efficiency is as low as 10% due to the contamination of the background hits. The selection of the primary track out of large number of false tracks is highly challenging as well. In the analysis we presented, the primary electron track was identified with a 69% efficiency at 25% occupancy with

the required reconstruction accuracy for the GMn experiment. These demonstrated parameters are adequate for the successful running of not only the GMn experiment but as well as for GEn-RP and GEn-II experiments, the second and third experiments in the program.

This work forms a solid foundation for further improvements in both hardware level noise suppression as well as in the tracking performance for these three experiments. This work started here also will lead the way along the long and daunting task to achieve acceptable performance conditions for running of the GEp-V experiment, the most demanding experiment in the SBS program, with an expected background level at 500 kHz/cm^2.

Appendix A

A second order fit was used to reconstruct interaction vertex variable (x', y', x, y, p) from track information (x, y, x', y'). Details are described in Chapter 5. The formalism is:

$$\begin{bmatrix} x'_{tar} \\ y'_{tar} \\ y_{tar} \\ p\theta_{bend} \end{bmatrix} = \sum_{i,j,k,l,m=0}^{i+j+k+l+m\leq n} \begin{bmatrix} C_{ijklm}^{x'_{tar}} \\ C_{ijklm}^{y'_{tar}} \\ C_{ijklm}^{y_{tar}} \\ C_{ijklm}^{p\theta} \end{bmatrix} x^i y^j x'^k y'^l x_{tar}^m \tag{A.1}$$

The coefficients C^*_{ijklm} in A.1 is optimized using simulation data. The best fit coefficients are listed below:

					x'_{tar}	y'_{tar}	y_{tar}	$p\theta_{bend}$
i	j	k	l	m				
0	0	0	0	0	-0.0023399735	0.015109238	-0.027331411	0.2941023
1	0	0	0	0	0.52645922	0.14988183	-0.2723771	0.07478357
2	0	0	0	0	0.0065104967	0.3709808	-0.67658112	-0.60286403
0	1	0	0	0	0.0018963363	0.088318529	0.78330346	0.11253975
1	1	0	0	0	0.0087115222	0.28692542	-0.71091522	0.58089714
0	2	0	0	0	0.0071650568	-0.013479714	0.08741709	0.15567453
0	0	1	0	0	-0.41462549	-0.42388853	0.76590971	0.0040847318
1	0	1	0	0	-0.17605705	-2.1042098	3.8150433	2.9139543

					x'_{tar}	y'_{tar}	y_{tar}	$p\theta_{bend}$
i	j	k	l	m				
0	1	1	0	0	-0.021797217	-1.3232674	3.1921555	-1.5882112
0	0	2	0	0	0.25139511	2.982271	-5.3748764	-3.4971735
0	0	0	1	0	-0.001748101	0.64590809	-1.8710832	-0.38319288
1	0	0	1	0	-0.032169232	-1.0586556	2.2743557	-1.7668259
0	1	0	1	0	-0.005125073	-0.16766129	0.034086571	-0.054698427
0	0	1	1	0	0.072193233	4.3064981	-9.6447674	4.8951522
0	0	0	2	0	0.041399153	0.512273	-0.64909614	0.02066852
0	0	0	0	1	-0.55026914	0.15458845	-0.44502715	-0.0085892838
1	0	0	0	1	-0.14898488	-1.0635359	1.6586957	1.0789112
0	1	0	0	1	-0.1452705	-0.039156188	-0.087998471	-0.29255214
0	0	1	0	1	0.42329522	2.6415749	-3.8303551	-2.8335405
0	0	0	1	1	0.32063216	0.89331415	-1.336202	0.18283264
0	0	0	0	2	-0.15391043	1.2878076	-4.5094245	5.3426858

Bibliography

[1] L. N. Hand, D. G. Miller, and Richard Wilson. Electric and magnetic form factors of the nucleon. *Rev. Mod. Phys.*, 35:335–349, Apr 1963.

[2] T. Janssens, R. Hofstadter, E. B. Hughes, and M. R. Yearian. Proton form factors from elastic electron-proton scattering. *Phys. Rev.*, 142:922–931, Feb 1966.

[3] R.C. Walker, B.W. Filippone, J. Jourdan, R. Milner, R. McKeown, D. Potterveld, R. Arnold, D. Benton, P. Bosted, G. deChambrier, L. Clogher, A. Lung, S.E. Rock, Z.M. Szalata, A. Para, F. Dietrich, K. Van Bibber, J. Button-Shafer, B. Debebe, R.S. Hicks, S. Dasu, P. de Barbaro, A. Bodek, H. Harada, M.W. Krasny, K. Lang, E.M. Riordan, J. Alster, R. Gearhart, and L.W. Whitlow. Measurement of the proton elastic form factors for Q^2=1$\sim$3$(GeV/c)^2$. *Physics Letters B*, 224(3):353 – 358, 1989.

[4] G.G. Simon, Ch. Schmitt, F. Borkowski, and V.H. Walther. Absolute electron-proton cross sections at low momentum transfer measured with a high pressure gas target system. *Nuclear Physics A*, 333(3):381 – 391, 1980.

[5] M. E. Christy, A. Ahmidouch, C. S. Armstrong, J. Arrington, R. Asaturyan, S. Avery, O. K. Baker, and etc Beck. Measurements of electron-proton elastic cross sections. *Phys. Rev. C*, 70:015206, Jul 2004.

[6] I. A. Qattan, J. Arrington, R. E. Segel, X. Zheng, K. Aniol, O. K. Baker, R. Beams, E. J. Brash, and etc Calarco. Precision rosenbluth measurement of the proton elastic form factors. *Phys. Rev. Lett.*, 94:142301, Apr 2005.

[7] V. Punjabi, C. F. Perdrisat, M. K. Jones, E. J. Brash, and C. E. Carlson. The structure of the nucleon: Elastic electromagnetic form factors, 2015.

[8] S. Rock, R. G. Arnold, P. Bosted, B. T. Chertok, B. A. Mecking, I. Schmidt, Z. M. Szalata, R. C. York, and R. Zdarko. Measurement of elastic electron-neutron cross sections up to $Q^2 = 10$ $(\mathrm{GeV}/c)^2$. *Phys. Rev. Lett.*, 49:1139–1142, Oct 1982.

[9] H. Anklin, E.E.W. Bruins, D. Day, D. Fritschi, B. Groft, F.C.P. Joosse, J. Jourdan, J. Lichtenstadt, M. Loppacher, G. Masson, J. Mitchell, I. Sick, and H.J.J. van Veen. Precision measurement of the neutron magnetic form factor. *Physics Letters B*, 336(3):313 – 318, 1994.

[10] E. E. W. Bruins, Th. S. Bauer, H. W. den Bok, C. P. Duif, W. C. van Hoek, D. J. J. de Lange, A. Misiejuk, Z. Papandreou, E. P. Sichtermann, J. A. Tjon, H. W. Willering, D. M. Yeomans, H. Reike, D. Durek, F. Frommberger, R. Gothe, D. Jakob, G. Kranefeld, C. Kunz, N. Leiendecker, G. Pfeiffer, H. Putsch, T. Reichelt, B. Schoch, D. Wacker, D. Wehrmeister, M. Wilhelm, E. Jans, J. Konijn, R. de Vries, C. Furget, E. Voutier, and H. Arenhövel. Measurement of the neutron magnetic form factor. *Phys. Rev. Lett.*, 75:21–24, Jul 1995.

[11] S. Riordan, S. Abrahamyan, B. Craver, A. Kelleher, A. Kolarkar, J. Miller, G. D. Cates, N. Liyanage, B. Wojtsekhowski, A. Acha, and et al. Measurements of the electric form factor of the neutron up to Q^2=3.4 GeV^2 using the reaction ^{3}He→(e,e′n)pp. *Physical Review Letters*, 105(26), Dec 2010.

[12] R. Madey, A. Yu. Semenov, S. Taylor, B. Plaster, A. Aghalaryan, and et. al Crouse. Measurements of G_E^n/G_M^n from the $^2\mathrm{H}(\vec{e}, e'\ \vec{n})^1\mathrm{H}$ reaction to $Q^2 = 1.45$ $(\mathrm{GeV}/c)^2$. *Phys. Rev. Lett.*, 91:122002, Sep 2003.

[13] J. Becker, H.G. Andresen, J.R.M. Annand, K. Aulenbacher, K. Beuchel, J. Blume-Werry, Th. Dombo, P. Drescher, M. Ebert, and et. al Eyl, D. Determination of the neutron electric form factor from the reaction ^{3}He(e,e'n) at medium momentum transfer. *The European Physical Journal A - Hadrons and Nuclei*, 6(3):329–344, Nov 1999.

[14] E. Geis, M. Kohl, V. Ziskin, and *et al.* Charge form factor of the neutron at low momentum transfer from the ^{2}H(e, e'n)p reaction. *Phys. Rev. Lett.*, 101:042501, Jul 2008.

[15] J. Bermuth et al. The Neutron charge form-factor and target analyzing powers from polarized-He-3 (polarized-e,e-prime n) scattering. *Phys. Lett.*, B564:199–204, 2003.

[16] I. Passchier and *et al.* Charge form factor of the neutron from the reaction $^2\ \vec{H}\ (\vec{e}, e'n)p$. *Phys. Rev. Lett.*, 82:4988–4991, Jun 1999.

[17] B. S. Schlimme and *et al.* Measurement of the neutron electric to magnetic form factor ratio at Q^2=1.58 GeV^2 using the reaction ^{3}He→(e,e′n)pp. *Phys. Rev. Lett.*, 111:132504, Sep 2013.

[18] M. Ostrick et al. Measurement of the neutron electric form-factor G_E^n in the quasi-free ^{2}H(e,e'n)p reaction. *Phys. Rev. Lett.*, 83:276–279, 1999.

[19] I. C. Cloët, G. Eichmann, B. El-Bennich, T. Klähn, and C. D. Roberts. Survey of nucleon electromagnetic form factors. *Few-Body Systems*, 46(1):1–36, Jun 2009.

[20] Elke-Caroline Aschenauer, A Bazilevsky, Les Bland, K Drees, Charles Folz, Y Makdisi, A Ogawa, P. Pile, T Throwe, H. Crawford, J Engelage, Eleanor Judd, A Derevshchikov, N Minaev, Dmitry Morozov, L Nogach, Matthias

Grosse Perdekamp, and M. Liu. A n dy: Measurement of the analyzing power for large rapidity drell-yan production at rhic. 09 2019.

[21] E. Chudakov C. DeJager P. Degtyarenko J. Gomez O. Hansen D. W. Higinbotham M. Jones J. LeRose R. Michaels S. Nanda A. Saha V. Sulkosky B. Wojtsekhowski etc A. Camsonne, J.P. Chen. Precision Measurement of the Neutron Magnetic Form Factor up to $Q^2 = 18.0$ $(GeV/c)^2$ by the Ratio Method.

[22] M. et al. Tanabashi. Review of particle physics. *Phys. Rev. D*, 98:030001, Aug 2018.

[23] Anna Peisert and Fabio Sauli. Drift and Diffusion of Electrons in Gases: A Compilation (With an Introduction to the Use of Computing Programs). 1984.

[24] David Griffiths. *Introduction to elementary particles*. 2008.

[25] Murray Gell-Mann. A Schematic Model of Baryons and Mesons. *Phys. Lett.*, 8:214–215, 1964.

[26] G. Zweig. An SU(3) model for strong interaction symmetry and its breaking. Version 2. In D.B. Lichtenberg and Simon Peter Rosen, editors, *DEVELOPMENTS IN THE QUARK THEORY OF HADRONS. VOL. 1. 1964 - 1978*, pages 22–101. 1964.

[27] J I Friedman and H W Kendall. Deep inelastic electron scattering. *Annual Review of Nuclear Science*, 22(1):203–254, 1972.

[28] F. Halzen and Alan D. Martin. *QUARKS AND LEPTONS: AN INTRODUCTORY COURSE IN MODERN PARTICLE PHYSICS*. 1984.

[29] Ashot Gasparian. The PRad experiment and the proton radius puzzle. *EPJ Web Conf.*, 73:07006, 2014.

[30] P. G. Blunden, W. Melnitchouk, and J. A. Tjon. Two-photon exchange and elastic electron-proton scattering. *Phys. Rev. Lett.*, 91:142304, Oct 2003.

[31] A. I. Akhiezer and Mikhail.P. Rekalo. Polarization phenomena in electron scattering by protons in the high energy region. *Sov. Phys. Dokl.*, 13:572, 1968. [Dokl. Akad. Nauk Ser. Fiz.180,1081(1968)].

[32] A. I. Akhiezer and Mikhail.P. Rekalo. Polarization effects in the scattering of leptons by hadrons. *Sov. J. Part. Nucl.*, 4:277, 1974. [Fiz. Elem. Chast. Atom. Yadra4,662(1973)].

[33] Raymond G. Arnold, Carl E. Carlson, and Franz Gross. Polarization transfer in elastic electron scattering from nucleons and deuterons. *Phys. Rev. C*, 23:363–374, Jan 1981.

[34] A.S Raskin and T.W Donnelly. Polarization in coincidence electron scattering from nuclei. *Annals of Physics*, 191(1):78 – 142, 1989.

[35] T.W Donnelly and A.S Raskin. Considerations of polarization in inclusive electron scattering from nuclei. *Annals of Physics*, 169(2):247 – 351, 1986.

[36] M. K. Jones, A. Aghalaryan, A. Ahmidouch, R. Asaturyan, F. Bloch, W. Boeglin, P. Bosted, C. Carasco, R. Carlini, J. Cha, and et al. Proton G_E/G_M from beam-target asymmetry. *Physical Review C*, 74(3), Sep 2006.

[37] O. Gayou, K. A. Aniol, T. Averett, F. Benmokhtar, W. Bertozzi, L. Bimbot, E. J. Brash, J. R. Calarco, C. Cavata, Z. Chai, C.-C. Chang, T. Chang, J.-P. Chen, E. Chudakov, R. De Leo, S. Dieterich, R. Endres, M. B. Epstein, S. Escoffier, K. G. Fissum, and etc Fonvieille. Measurement of G_{E_p}/G_{M_p} in $\overrightarrow{e}\ p \rightarrow e\ \overrightarrow{p}$ to Q^2= 5.6 GeV^2. *Phys. Rev. Lett.*, 88:092301, Feb 2002.

[38] A. J. R. Puckett et al. Final Analysis of Proton Form Factor Ratio Data at $Q^2 = 4.0$, 4.8 and 5.6 GeV^2. *Phys. Rev.*, C85:045203, 2012.

[39] A. J. R. Puckett et al. Recoil Polarization Measurements of the Proton Electromagnetic Form Factor Ratio to $Q^2 = 8.5 GeV^2$. *Phys. Rev. Lett.*, 104:242301, 2010.

[40] A. J. R. Puckett et al. Polarization Transfer Observables in Elastic Electron Proton Scattering at Q^2 =2.5, 5.2, 6.8, and 8.5 GeV^2. *Phys. Rev.*, C96(5):055203, 2017. [erratum: Phys. Rev.C98,no.1,019907(2018)].

[41] J. R. Dunning, K. W. Chen, A. A. Cone, G. Hartwig, N. F. Ramsey, J. K. Walker, and Richard Wilson. Quasi-elastic electron-deuteron scattering and neutron form factors. *Phys. Rev.*, 141:1286–1297, Jan 1966.

[42] P. Stein, M. Binkley, R. McAllister, A. Suri, and W. Woodward. Measurements of neutron form factors. *Phys. Rev. Lett.*, 16:592–594, Mar 1966.

[43] J. Lachniet, A. Afanasev, H. Arenhövel, W. K. Brooks, and et. al Gilfoyle. Precise measurement of the neutron magnetic form factor G_M^n in the few-gev^2 region. *Phys. Rev. Lett.*, 102:192001, May 2009.

[44] D. Benaksas, D. Drickey, and D. Frerejacque. Deuteron Electromagnetic Form Factors for $3F^{-2} < q^2 < 6F^{-2}$. *Phys. Rev.*, 148:1327–1331, 1966.

[45] B. Grossetete, D. Drickey, and P. Lehmann. Elastic Electron-Deuteron Scattering. *Phys. Rev.*, 141:1425–1434, 1966.

[46] S. Galster, H. Klein, J. Moritz, K. H. Schmidt, D. Wegener, and J. Bleckwenn. Elastic electron-deuteron scattering and the electric neutron form factor at four-momentum transfers $5\text{fm}^{-2} < q^2 < 14\text{fm}^{-2}$. *Nucl. Phys.*, B32:221–237, 1971.

[47] S. Platchkov et al. Deuteron A(Q^2) structure function and the neutron electric form factor. *Nuclear Physics A*, 508:343 – 348, 1990.

[48] A. V. Belitsky, Xiangdong Ji, and Feng Yuan. Perturbative qcd analysis of the nucleon's pauli form factor $F_2(Q^2)$. *Phys. Rev. Lett.*, 91:092003, Aug 2003.

[49] A. De Rújula, Howard Georgi, and S. L. Glashow. Hadron masses in a gauge theory. *Phys. Rev. D*, 12:147–162, Jul 1975.

[50] Nathan Isgur and Gabriel Karl. p-wave baryons in the quark model. *Phys. Rev. D*, 18:4187–4205, Dec 1978.

[51] F. Cardarelli, E. Pace, G. SalmÃÍ, and S. Simula. Nucleon and pion electromagnetic form factors in a light-front constituent quark model. *Physics Letters B*, 357(3):267–272, Sep 1995.

[52] Franz Gross, G. Ramalho, and M. T. Peña. Pure s-wave covariant model for the nucleon. *Phys. Rev. C*, 77:015202, Jan 2008.

[53] J.P.B.C. de Melo, T. Frederico, E. Pace, S. Pisano, and G. SalmÃÍ. Timelike and spacelike nucleon electromagnetic form factors beyond relativistic constituent quark models. *Physics Letters B*, 671(1):153 – 157, 2009.

[54] J. Alcorn, B.D. Anderson, K.A. Aniol, J.R.M. Annand, L. Auerbach, J. Arrington, T. Averett, F.T. Baker, M. Baylac, E.J. Beise, J. Berthot, P.Y. Bertin, W. Bertozzi, L. Bimbot, T. Black, and W.U. Boeglin etc. Basic instrumentation for hall a at jefferson lab. *Nuclear Instruments and Methods in Physics Research Section A: Accelerators, Spectrometers, Detectors and Associated Equipment*, 522(3):294 – 346, 2004.

[55] D. Wang et al. Measurement of parity violation in electron-quark scattering. *Nature*, 506(7486):67–70, 2014.

[56] R D McKeown. The jefferson lab 12 GeV upgrade. *Journal of Physics: Conference Series*, 312(3):032014, sep 2011.

[57] L.S. Azhgirey, V.A. Arefiev, I. Atanasov, S.N. Basilev, Yu.P. Bushuev, V.V. Glagolev, M.K. Jones, D.A. Kirillov, P.P. Korovin, G.J. Kumbartzki, P.K. Manyakov, J. MuÅąinskÃ¡, L. Pentchev, C.F. Perdrisat, V. Punjabi, N.M. Piskunov, I.M. Sitnik, V.M. Slepnev, I.V. Slepnev, and E. Tomasi-Gustafsson. Measurement of analyzing powers for the reaction p + CH_2 at p_p = 1.75 - 5.3 GeV/c. *Nuclear Instruments and Methods in Physics Research Section A: Accelerators, Spectrometers, Detectors and Associated Equipment*, 538(1):431 – 441, 2005.

[58] N. V. Vlasov, O. P. Gavrishchuk, N. A. Kuz'min, V. V. Kukhtin, A. N. Maksimov, P. K. Man'yakov, Yu. V. Mikhailov, I. A. Savin, V. K. Semenov, A. B. Shalygin, and A. I. Yukaev. A calorimeter for detecting hadrons with energies of 10–100 gev. *Instruments and Experimental Techniques*, 49(1):41–55, Jan 2006.

[59] A. Danagoulian, V. H. Mamyan, M. Roedelbronn, K. A. Aniol, J. R. M. Annand, P. Y. Bertin, L. Bimbot, and P. etc Bosted. Compton-scattering cross section on the proton at high momentum transfer. *Phys. Rev. Lett.*, 98:152001, Apr 2007.

[60] D.J.J de Lange, J.J.M Steijger, H de Vries, M Anghinolfi, M Taiuti, D.W Higinbotham, B.E Norum, and E Konstantinov. A large acceptance spectrometer for the internal target facility at nikhef. *Nuclear Instruments and Methods in Physics Research Section A: Accelerators, Spectrometers, Detectors and Associated Equipment*, 406(2):182 – 194, 1998.

[61] Xin Qian. Double-Spin Asymmetry Measurements of Semi-Inclusive Pion Electro-Production on a Transversely Polarized ^{3}He Target Through Deep Inelastic Scattering. *Modern Physics Letters A*, 27(21):1230021–1–1230021–14, Jul 2012.

[62] Xin Qian. Measurement of single target-spin asymmetry in semi-inclusive pion electroproduction on a transversely polarized ^3he target. pages 3006–, 10 2010.

[63] M. Mihovilovič, S. Širca, K. Allada, B. D. Anderson, J. R. M. Annand, T. Averett, A. Camsonne, R. W. Chan, J. P. Chen, K. Chirapatpimol, C. W. de Jager, S. Gilad, D. J. Hamilton, and etc Hansen. Methods for optical calibration of the BigBite hadron spectrometer. *Nuclear Instruments and Methods in Physics Research A*, 686:20–30, Sep 2012.

[64] M. Iodice and *et al.* The CO_2 gas cherenkov detectors for the jefferson lab hall-a spectrometers. *Nuclear Instruments and Methods in Physics Research Section A: Accelerators, Spectrometers, Detectors and Associated Equipment*, 411(2):223 – 237, 1998.

[65] D. J. Hamilton, A. Shahinyan, B. Wojtsekhowski, and *et al.* An Electromagnetic Calorimeter for the JLab Real Compton Scattering Experiment. *arXiv e-prints*, page arXiv:0704.1830, Apr 2007.

[66] C. Ciofi degli Atti and S. Scopetta. On the extraction of the neutron spin structure functions and the gerasimov-drell-hearn integral from the process ^{3}He(e,e')X in the resonance region. *Physics Letters B*, 404(3):223 – 229, 1997.

[67] F. Bissey, A. W. Thomas, and I. R. Afnan. Structure functions for the three-nucleon system. *Phys. Rev. C*, 64:024004, Jul 2001.

[68] Thad G. Walker and William Happer. Spin-exchange optical pumping of noble-gas nuclei. *Rev. Mod. Phys.*, 69:629–642, Apr 1997.

[69] M. A. Bouchiat, T. R. Carver, and C. M. Varnum. Nuclear polarization in he^3 gas induced by optical pumping and dipolar exchange. *Phys. Rev. Lett.*, 5:373–375, Oct 1960.

[70] Earl Babcock, Ian Nelson, Steve Kadlecek, Bastiaan Driehuys, L. W. Anderson, F. W. Hersman, and Thad G. Walker. Hybrid spin-exchange optical pumping of ^{3}He. *Phys. Rev. Lett.*, 91:123003, Sep 2003.

[71] W. R. Leo. *Techniques for Nuclear and Particle Physics Experiments: A How to Approach*. 1987.

[72] M. Tanabashi, K. Hagiwara, K. Hikasa, K. Nakamura, Y. Sumino, F. Takahashi, J. Tanaka, K. Agashe, G. Aielli, C. Amsler, M. Antonelli, D. M. Asner, H. Baer, Sw. Banerjee, R. M. Barnett, T. Basaglia, C. W. Bauer, J. J. Beatty, and etc Belousov. Review of particle physics. *Phys. Rev. D*, 98:030001, Aug 2018.